https://doi.org/10.5194/egusphere-2026-2425
Preprint. Discussion started: 26 May 2026

The Met Office Unified Model and JULES Global Atmosphere and Land 9.0 configuration

Martin R. Willett[1], Melissa E. Brooks[1], Andrew Bushell[1], Paul Earnshaw[1], Charline Marzin[1], Samantha Smith[1], Lorenzo Tomassini[1,2], Nathan Luke Abraham[3,4], Martin Best[1], John M. Edwards[1], Kalli Furtado[1,a], Catherine Hardacre[1,b], Alan J. Hewitt[1], Ben Johnson[1], Adrian Lock[1], Jane P. Mulcahy[1], James Manners[1], Alistair Sellar[1], Peter Sheridan[1], Warren Tennant[1], Kwinten Van Weverberg[1,c], Vidya Varma[5,d], and Michael Whitall[1]

[1]Met Office, FitzRoy Road, Exeter, Devon, EX1 3PB, United Kingdom
[2]School of Mathematics, University of Leeds, Leeds, LS2 9JT, United Kingdom
[3]National Centre for Atmospheric Science, University of Cambridge, Cambridge CB2 1EW, United Kingdom
[4]Yusuf Hamied Department of Chemistry, University of Cambridge, Cambridge, CB2 1EW, United Kingdom
[5]National Institute of Water and Atmospheric Research Ltd (NIWA), Wellington, 6021, New Zealand
[a]Now at National Oceanography Center, European Way, Southampton, SO14 3ZH, United Kingdom
[b]Now at School of Physical and Chemical Sciences, University of Canterbury, New Zealand
[c]Now at Department of Geography, Ghent University, Belgium and Royal Meteorological Institute of Belgium, Ringlaan 3, 1180 Brussels, Belgium
[d]Now at The Institute of Climate and Energy Systems - Troposphere (ICE-3), Forschungszentrum Jülich, Wilhelm-Johnen-Straße, 52428 Jülich, Germany

Correspondence: Martin Willett (martin.willett@metoffice.gov.uk)

Abstract.

We describe Global Atmosphere and Land 9.0 (GAL9) and GAL9.1: the latest science configurations of the Met Office Unified Model and JULES land surface model developed for seamless use across weather and climate timescales. GAL9 builds upon GA8GL9. GAL9 includes developments to most areas of the science. Some of the key changes include: moving to a single "mid-level" scheme to represent surface driven deep convection and elevated convection that improves the diurnal cycle of convection, an enhancement to the semi-Lagrangian advection that improves local conservation, improved physical realism in the gravity wave drag scheme by accounting for the effects of humidity and latent heating, and a package of enhancements to the land surface which improve soil moisture profiles and remove the need to apply an observation based albedo scaling. The NWP and climate performance of GAL9 is evaluated against the previous configuration, GA8GL9. In NWP tests GAL9 is shown have reduced errors relative to GA8GL9. The mean climate in GAL9 is shown to be improved relative to GA8GL9 with notable improvements in the top of atmosphere outgoing shortwave radiation. NWP tests of GAL9.0 at 10 km showed a degradation relative to GA8GL9. This issue is resolved in the branch configuration GAL9.1 that includes an improved orography. GAL9/GAL9.1 is the atmosphere and land component of GC5/GC5.1. From early 2026, GC5.1 is being be used as the operational global NWP model at the Met Office and GC5 will be a key component of the UK's contribution to CMIP7.

https://doi.org/10.5194/egusphere-2026-2425
Preprint. Discussion started: 26 May 2026

1 Introduction

At the Met Office and other UM partners the Unified Model (UM) and JULES are used in defined Global Atmosphere (GA) and Global Land (GL) configurations to simulate the global atmosphere-land system. The GA/GL development process is described in Walters et al. (2011). Each subsequent GA/GL configuration is built upon the previous configuration. For example, the subject of this report, GAL9, is built upon the previous configuration GA8.0GL9.0 (Willett et al., 2026). Each GA/GL configuration is designed for seamless use across all timescales and global resolutions, and hence is assessed in terms of both its climate and NWP performance. Global coupled (GC) configurations also include Global Ocean (GO) and Global Sea-Ice (GSI) components to simulate the global atmosphere-land-ocean-sea-ice system. The naming convention has been modified from previous configurations to use a single version number for the combined atmosphere and land model - in this case GAL9. This reflects the fact that the atmosphere model is always used in combination with the land surface model and never in isolation.

For brevity in this document the suffix ".0" will be dropped when referring to the trunk configurations (GAL9 rather than GAL9.0).

GC5 couples GAL9 with the GOSI9.0 ocean (Guiavarc'h et al., 2025). GAL9 and GC5 were released in early 2023. GC5.1, which differs from GC5 by the inclusion of GAL9.1, has been used for operational global NWP at the Met Office from January 2026. GC5 will be a key component of the UK's contribution to CMIP7. The next GAL/GC configuration, GAL10/GC6, will build upon GAL9/GC5.

The primary aims of this paper are to provide a stand-alone scientific description of GAL9 (and hence a single reference) and to describe how GAL9 differs from the previous configuration, GA8GL9. To that end, Sect. 3 of this document provides a scientific description of GAL9[1], Sect. 2 describes the development process, and Sect. 4 details all changes made between GA8GL9 and GAL9. The development of these changes is documented using "trac" issue tracking software; for consistency with that documentation, we have included the trac ticket numbers with each change. A full assessment of the performance of GAL9/GC5 is made in Xavier et al. (2026), but a brief assessment of GAL9 relative to GA8GL9 is given in Sect. 5. The differences between GAL9 and the branch configuration, GAL9.1, are described in Sect. 6.

2 The development process

Every change being considered for inclusion in GAL9 was tested individually on top of GA8GL9 control simulations. At a minimum this would include 20-year N96 AMIP simulations and a set of 24 N320 NWP case studies, but additional tests were

[1]Where the configuration remains unchanged from GA8GL9 and its predecessors, Sect. 3 contains material which is unaltered from the documentation papers for those releases (i.e Willett et al., 2026; Walters et al., 2019, 2017, 2014, 2011)

https://doi.org/10.5194/egusphere-2026-2425
Preprint. Discussion started: 26 May 2026

performed if it was deemed to be necessary. For example, all changes that had a non-negligible effect in the NWP case studies were also tested using 3-month summer and winter N320 Data Assimilation (DA) trials. The results from the testing of each change were recorded in its “trac” ticket. Changes that were considered acceptable in terms of their scientific performance, technical quality and documentation were passed to "package" testing.

The first stage of package testing combined all the changes from broad science areas (i.e. gravity waves and orographic effects, boundary layer, convection, aerosols, clouds and radiation, land surface, corrections) together and test again using N96 AMIP simulations, N320 NWP case studies and DA trials. In the next stage of package testing the science area packages were incrementally added together and retested. Throughout this process any changes in the model’s scientific performance were identified and recorded. This development process ensures that any changes in model behaviour are traceable to individual science changes or combinations of changes. This helps in identifying the physical mechanism for any new biases or undesirable model behaviour introduced during the development process and consequently hence helps to identify potential mitigation measures. Possible mitigation measures include the introduction of an additional science change, tuning of model parameters (Sect. 4.12), or exclusion of a change from the configuration if the error it introduces cannot be adequately addressed.

Additional tests such as N96 and N216 coupled climate simulations, N320 coupled NWP case studies, N640 NWP case studies, N216 and N640 AMIP simulations and N96 AMIP+4K simulations were performed at various stages during the development process to evaluate coupled performance, resolution sensitivity, computational stability at higher resolutions and climate feedbacks.

Several additional science changes were introduced during package testing to address issues identified during the development process. Numerous sensitivity tests to the values of model parameters were performed on top of the trunk configuration at various stages throughout the development process using AMIP simulations, NWP case studies and DA trials. The parameters were chosen to address biases in the trunk development configuration and selected by considering the effect of individual science changes, a physical understand of the processes leading to the biases, an understanding of what parameters do within a physics scheme, and results from previous parameter sensitivity tests (sensitivity tests at earlier configurations and in "perturbed parameter ensembles" of GA8GL9).

The top of the atmosphere fluxes were tuned during the package development process to facilitate coupled climate tests to avoid long term drifts in the ocean and sea-ice. During the later stages of the development several "release candidates" were defined and evaluated. It was during these stages that other parameter tunings were introduced. Some additional fine tuning of the top of atmosphere fluxes was undertaken at the final stages of the development process. The tuning is discussed further in Sect. 4.12.

3 Global Atmosphere and Global Land 9.0

3.1 Dynamical formulation and discretisation

The UM’s ENDGame dynamical core uses a semi-implicit semi-Lagrangian formulation to solve the non-hydrostatic, fully-compressible deep-atmosphere equations of motion (Wood et al., 2014). The primary atmospheric prognostics are the three-

https://doi.org/10.5194/egusphere-2026-2425
Preprint. Discussion started: 26 May 2026

dimensional wind components, virtual dry potential temperature, Exner pressure, and dry density, whilst moist prognostics such as the mass mixing ratio of water vapour and prognostic cloud fields as well as other atmospheric loadings are advected as free tracers. These prognostic fields are discretised horizontally onto a regular longitude/latitude grid with Arakawa C-grid staggering (Arakawa and Lamb, 1977), whilst the vertical discretisation utilises a Charney-Phillips staggering (Charney and Phillips, 1953) using terrain-following hybrid height coordinates. The discretised equations are solved using a nested iterative approach centred about solving a linear Helmholtz equation. By convention, global configurations are defined on $2 \times N$ longitudes and $1.5 \times N$ latitudes of scalar grid-points, with the meridional wind variable first stored at the north and south poles and scalar and zonal wind variables first stored half a grid length away from the poles. This choice makes the grid-spacing approximately isotropic in the mid-latitudes and means that the integer N, which represents the maximum number of zonal 2 grid-point waves that can be represented by the model, uniquely defines its horizontal resolution; a model with $N = 96$ is said to be N96 resolution. Limited-area configurations use a rotated longitude/latitude grid with the pole rotated so that the grid's equator runs through the centre of the model domain. In the vertical, most climate configurations use an 85-level set labelled $\mathrm{L85}(50_\mathrm{t}, 35_\mathrm{s})_{85}$, which has 50 levels below 18 km (and hence at least sometimes in the troposphere), 35 levels above this (and hence solely in or above the stratosphere) and a fixed model lid 85 km above sea level. Finally, numerical weather prediction (NWP) configurations use a 70-level set, $\mathrm{L70}(50_\mathrm{t}, 20_\mathrm{s})_{80}$ which has an almost identical 50 levels below 18 km, a model lid at 80 km, but has a reduced stratospheric resolution compared to $\mathrm{L85}(50_\mathrm{t}, 35_\mathrm{s})_{85}$. Although we use a range of vertical resolutions in the stratosphere, a consistent tropospheric vertical resolution is currently used for a given GA configuration. A more detailed description of these level sets is included in the supplementary material to Walters et al. (2019). For stagnation points, where semi-Lagrangian advection can give poor local conservation, a local correction is applied as discussed in Sect. 4.10.1. At the end of the time step, the dry density is scaled such that the global dry mass of atmosphere is conserved without altering its potential energy as described in Walters et al. (Sect. 3.1 of 2017). The optimised conservative filter (OCF) scheme of Zerroukat and Allen (2015) is applied to the mass-weighted virtual dry potential temperature to ensure its conservation. For systems where the exact conservation is considered to be important (e.g. long climate integrations), the OCF scheme is also applied to the moist prognostics.

3.2 Structure of the atmospheric model time step

With ENDGame, the UM uses a nested iterative structure for each atmospheric time step within which processes are split into an outer loop and an inner loop. The semi-Lagrangian departure point equations are solved within the outer loop using the latest estimates for the wind variables. Appropriate fields are then interpolated to the updated departure points. Within the inner loop, the Coriolis, orographic and non-linear terms are solved along with a linear Helmholtz problem to obtain the pressure increment. The Helmholtz problem is solved using a multigrid method. Latest estimates for all variables are then obtained from the pressure increment via a back-substitution process; see Wood et al. (2014) for details. The physical parametrisations are split into slow processes (radiation, large-scale precipitation and gravity wave drag) and fast processes (atmospheric boundary layer turbulence, convection and surface coupling). The slow processes are treated in parallel and are computed once per time step before the outer loop. The source terms from the slow processes are then added on to the appropriate fields before

https://doi.org/10.5194/egusphere-2026-2425
Preprint. Discussion started: 26 May 2026

interpolation. The fast processes are treated sequentially and are computed in the outer loop using the latest predicted estimate for the required variables at the next, $n+1$ time step. A summary of the atmospheric time step is given in Algorithm 1. In practice two iterations are used for each of the outer and inner loops so that the Helmholtz problem is solved four times per time step. The prognostic aerosol scheme is included via a call to the UK Chemistry and Aerosol (UKCA) code after the main atmospheric time step; this call is currently performed once per hour. Finally, Table 1 contains the typical length of time step used for a range of horizontal resolutions.

Algorithm 1 Iterative structure of time step $n+1$. Here, we use two inner and two outer loops ($L=2$, $M=2$).

Given the solution at time step n, let the first estimate for a prognostic variable F at time level $n+1$ be $F^{n+1}=F^n$
Compute slow parametrised processes and time level n forcings R_F^n

for $m=1,M$ **do** {*departure (outer-loop) iteration*}
    Solve the trajectory equations to compute the next estimate of the departure points using the time level n and the latest estimate for time level $n+1$ wind fields
    Interpolate R_F^n to departure points
    Compute time level $n+1$ predictors F^*
    Compute fast parametrised processes using latest $n+1$ predictor F^*
    Evaluate time level n component of Helmholtz right hand side $\mathfrak{R}^n$

    for $l=1,L$ **do** {*non-linear (inner-loop) iteration*}
        Evaluate non-linear and Coriolis terms R_F^*
        Evaluate time level $n+1$ component of Helmholtz right hand side $\mathfrak{R}^*$
        Solve the Helmholtz problem for the pressure increment π' and hence obtain the next estimate for $\pi^{n+1}\equiv\pi^n+\pi'$
        Obtain the other prognostic variables at time level $n+1$ via back-substitution
    end for

end for

3.3 Solar and terrestrial radiation

Shortwave (SW) radiation from the Sun is absorbed and reflected in the atmosphere and at the Earth's surface and provides energy to drive the atmospheric circulation. Longwave (LW) radiation is emitted from the planet and interacts with the atmosphere, redistributing heat, before being emitted into space. These processes are parametrised via the radiation scheme, which provides prognostic atmospheric temperature increments, prognostic surface fluxes and additional diagnostic fluxes. The SOCRATES [2] radiative transfer scheme (Edwards and Slingo, 1996; Manners et al., 2025) is used for GAL9. Solar ra-

[2] https://github.com/MetOffice/socrates

https://doi.org/10.5194/egusphere-2026-2425
Preprint. Discussion started: 26 May 2026

Table 1. Typical time step for a range of horizontal resolutions.

Grid	Nominal horizontal resolution	Typical time step
N96	135 km	20.0 min
N216	60 km	15.0 min
N320	40 km	12.0 min
N512	25 km	10.0 min
N640	20 km	7.5 min
N768	17 km	7.5 min
N1280	10 km	4.0 min

diation is treated in 6 SW bands and thermal radiation in 9 LW bands, as outlined in Table 2. Gaseous absorption uses the correlated-k method with newly derived coefficients for all gases (except where indicated below) based on the HITRAN 2012 spectroscopic database (Rothman et al., 2013). Scaling of absorption coefficients uses a look-up table of 59 pressures with 5 temperatures per pressure level based around a mid-latitude summer profile. The method of equivalent extinction (Edwards, 1996; Amundsen et al., 2017) is used for minor gases in each band. The water vapour continuum is represented using laboratory results from the CAVIAR project (Continuum Absorption at Visible and Infrared wavelengths and its Atmospheric Relevance) between 1 and 5 µm (Ptashnik et al., 2011, 2012) and version 2.5 of the Mlawer–Tobin_Clough–Kneizys–Davies (MT_CKD-2.5) model (Mlawer et al., 2012) at other wavelengths.

Table 2. Spectral bands for the treatment of incoming solar (SW) radiation (left) and thermal (LW) radiation (right).

SW Band	Wavelength (nm)
1	200 - 320
2	320 - 505
3	505 - 690
4	690 - 1190
5	1190 - 2380
6	2380 - 10000
-	-
-	-
-	-

LW Band	Wavenumber (cm^{-1})	Wavelength (μm)
1	1 - 400	25 - 10000
2	400 - 550	18.18 - 25
3	550 - 590 and 750 - 800	12.5 - 13.33 and 16.95 - 18.18
4	590 - 750	13.33 - 16.95
5	800 - 990 and 1120 - 1200	8.33 - 8.93 and 10.10 - 12.5
6	990 - 1120	8.93 - 10.10
7	1200 - 1330	7.52 - 8.33
8	1330 - 1500	6.67 - 7.52
9	1500 - 2995	3.34 - 6.67

Forty-one (41) k terms are used for the major gases in the SW bands. Absorption by water vapour (H_2O), carbon dioxide (CO_2), ozone (O_3), oxygen (O_2), nitrous oxide (N_2O) and methane (CH_4) is included. Ozone cross-sections for the ultra-violet and visible come from Serdyuchenko et al. (2014) and Gorshelev et al. (2014), along with Brion-Daumont-Malicet (Daumont et al., 1992; Malicet et al., 1995) for the far-UV. In the first SW band, a single k-term is calculated for each 20 nm sub-interval

https://doi.org/10.5194/egusphere-2026-2425
Preprint. Discussion started: 26 May 2026

from 200 to 320 nm, and in band 2, a single k-term is calculated for each of the sub-intervals 320-400 nm and 400-505 nm. This allows the incoming solar flux to be supplied on these finer wavelength bands for experiments concerning solar spectral variability. The solar spectrum uses data from NRLSSI (Lean et al., 2005) as recommended by the SPARC/SOLARIS [3] group. A mean solar spectrum for the period 2000-2011 is used when a varying spectrum is not invoked.

Eighty-one (81) k terms are used for the major gases in the LW bands. Absorption by H_2O, O_3, CO_2, CH_4, N_2O, CFC-11 (CCl_3F), CFC-12 (CCl_2F_2) and HFC134a (CH_2FCF_3) is included. For climate simulations, the atmospheric concentrations of CFC-12 and HFC134a are adjusted to represent absorption by all the remaining trace halocarbons. The treatment of CO_2 absorption for the peak of the 15 µm band (LW band 4) is as described in Zhong and Haigh (2000). An improved representation of CO_2 absorption in the "window" region (8 - 13 µm) provides a better forcing response to increases in CO_2 (Pincus et al., 2015). The method of "hybrid" scattering is used in the LW which runs full scattering calculations for 27 of the major gas k-terms (where their nominal optical depth is less than 10 in a mid-latitude summer atmosphere). For the remaining 54 k-terms (optical depth > 10) much cheaper non-scattering calculations are run.

Of the major gases considered, only H_2O is prognostic; O_3 uses a zonally symmetric climatology, whilst other gases are prescribed using either fixed or time-varying mass mixing ratios and assumed to be well mixed.

Absorption and scattering by the following prognostic aerosol species (the representation of which is discussed in Sect. 3.10 below) are included in both the SW and LW using the UKCA-Radaer scheme: sulphate, black carbon, organic carbon and sea salt. The aerosol scattering and absorption coefficients and asymmetry parameters are precomputed for a wide range of plausible Mie parameters and stored in look-up tables for use during run-time when the atmospheric chemical composition, including mean aerosol particle radius and water content are known. As the aerosol species are internally mixed within the modal aerosol scheme (see Table 4 in Walters et al., 2019), the refractive indices of each mode are calculated online as a volume weighted mean of the component species contributing to that mode. The component refractive indices are documented in the Appendix of Bellouin et al. (2013) apart from black carbon that was updated to the middle value from Bond and Bergstrom (2006) as discussed in Willett et al. (2026). Nucleation mode particles are neglected as they are not expected to contribute significantly to the atmospheric optical properties. The parametrisation of cloud droplets is described in Edwards and Slingo (1996) using the method of "thick averaging". Padé fits are used for the variation with effective radius, which is computed from the number of cloud droplets. In configurations using prognostic aerosol, cloud droplet number concentrations (CDNCs) are not calculated within the radiation scheme itself but are calculated by the UKCA-Activate scheme (West et al., 2014), which is based on the activation scheme of Abdul-Razzak and Ghan (2000). In configurations that use climatological aerosols (typically NWP) the CDNC is usually calculated using the method described in Jones et al. (1994) to reduce computational cost. Both prognostic and climatological simulations of mineral dust use the CLASSIC scheme (Woodward, 2011). The parametrisation of ice crystals is described in Baran et al. (2016). Full treatment of scattering is used in both the SW and LW. The sub-grid cloud structure is represented using the Monte Carlo Independent Column Approximation (McICA) (Pincus et al. (2003) with enhancements and implementation described in Hill et al. (2011)), with the parametrisation of subgrid-scale water content variability described in Hill et al. (2015).

[3] http://solarisheppa.geomar.de/ccmi

https://doi.org/10.5194/egusphere-2026-2425
Preprint. Discussion started: 26 May 2026

Full radiation calculations are made every hour using the instantaneous cloud fields and a mean solar zenith angle for the following 1 h period. Corrections are made for the change in solar zenith angle on every model time step as described in Manners et al. (2009). The emissivity and the albedo of the surface are set by the land surface model. The direct SW flux at the surface is corrected for the angle and aspect of the topographic slope as described in Manners et al. (2012).

3.4 Large-scale precipitation

The formation and evolution of precipitation due to grid scale processes is the responsibility of the large-scale precipitation — or microphysics — scheme, whilst small-scale precipitating events are handled by the convection scheme. The microphysics scheme has prognostic input fields of temperature, moisture, cloud and precipitation from the end of the previous time step, which it modifies in turn. The microphysics used is a single moment scheme based on Wilson and Ballard (1999), with extensive modifications. The warm-rain scheme is based on Boutle et al. (2014b), and includes a prognostic rain formulation, which allows three-dimensional advection of the precipitation mass mixing ratio, and an explicit representation of the effect of sub-grid variability on autoconversion and accretion rates (Boutle et al., 2014a). We use the rain-rate dependent particle size distribution of Abel and Boutle (2012) and fall velocities of Abel and Shipway (2007), which combine to allow a better representation of the sedimentation and evaporation of small droplets. We also make use of multiple sub-time steps of the precipitation scheme, with one call to the scheme for every two minutes of model time step. This is required to achieve a realistic treatment of in-column evaporation. With prognostic aerosol, we use the UKCA-Activate aerosol activation scheme (West et al., 2014) to provide the cloud droplet number for autoconversion, where particles from the soluble aerosol modes are activated into cloud droplets. The soluble modes comprise sulphate, sea salt, black carbon and organic carbon but with black carbon remaining hydrophobic within the internally mixed particles. The Aitken insoluble mode comprised of black carbon and organic carbon also participates in activation to form cloud condensation nuclei. In configurations that use climatological aerosols (typically NWP), the cloud droplet number is usually calculated using the method described in Jones et al. (1994) to reduce computational cost. Ice cloud parametrisations use the generic size distribution of Field et al. (2007) and mass-diameter relations of Cotton et al. (2013).

3.5 Large-scale cloud

Cloud appears on sub-grid scales well before the humidity averaged over the size of a model grid box reaches saturation. A cloud parametrisation scheme is therefore required to determine the fraction of the grid box which is covered by cloud and the amount and phase of condensed water contained in this cloud. The formation of cloud will convert water vapour into liquid or ice and release latent heat. The cloud cover and liquid and ice water contents are then used by the radiation scheme to calculate the radiative impact of the cloud and by the large-scale precipitation scheme to calculate whether any precipitation has formed.

The parametrisation used is the prognostic cloud fraction and prognostic condensate (PC2) scheme (Wilson et al., 2008a, b) along with the cloud erosion parametrisation described by Morcrette (2012) and critical relative humidity parametrisation described in Van Weverberg et al. (2016). PC2 uses three prognostic variables for water mixing ratio — vapour, liquid and

https://doi.org/10.5194/egusphere-2026-2425
Preprint. Discussion started: 26 May 2026

ice — and a further three prognostic variables for cloud fraction: liquid, ice and mixed-phase. The following atmospheric processes can modify the cloud fields: SW radiation, LW radiation, boundary layer processes, convection, precipitation, small-scale mixing (cloud erosion), advection and changes in atmospheric pressure. The convection scheme calculates increments to the prognostic liquid and ice water contents by detraining condensate from the convective plume, whilst the cloud fractions are updated using the non-uniform forcing method of Bushell et al. (2003). One advantage of the prognostic approach is that cloud can be transported away from where it was created. For example, anvils detrained from convection can persist and be advected downstream long after the convection itself has ceased. The radiative impact of convective cores, which hold condensate not detrained into the environment, is represented by diagnosing a convective cloud amount (CCA) and convective cloud water (CCW) where the convection is active on a particular time-step. The CCA and CCW then get combined with the PC2 cloud fraction and condensate variables before these get passed to McICA to calculate the radiative impact of the combined cloud fields. Finally, the production of supercooled liquid water in a turbulent environment is parametrised following Furtado et al. (2016).

3.6 Sub-grid orographic drag

The effect of local and mesoscale orographic features not resolved by the mean orography, from individual hills through to small mountain ranges, must be parametrised.

The smallest scales, where buoyancy effects are assumed to be unimportant, are represented by the turbulent orographic form drag parametrisation of Wood et al. (2001). The effects of the remainder of the sub-grid orography (on scales where buoyancy effects are important) are parametrised by a drag scheme which represents the effects of low-level flow blocking and the drag associated with stationary gravity waves (mountain waves). This is based on the scheme described by Lott and Miller (1997), but with some important differences, described in more detail in Vosper (2015), and with further modifications to account for moist processes as summarised in Sect. 4.3.1 and described more fully in Smith (2021).

The sub-grid orography is assumed to consist of uniformly distributed elliptical mountains within the grid box, described in terms of a height amplitude, which is proportional to the grid box standard deviation of the source orography data, anisotropy (the extent to which the sub-grid orography is ridge-like, as opposed to circular), the alignment of the major axis and the mean slope along the major axis. The scheme is based on two different frameworks for the drag mechanisms: bluff body dynamics for the flow-blocking and linear gravity waves for the mountain wave drag component.

The degree to which the flow is blocked and so passes around, rather than over the mountains is determined by the Froude number, $F = U/(NH)$ where H is the assumed sub-grid mountain height (proportional to the sub-grid standard deviation of the source orography data) and N and U are respectively measures of the buoyancy frequency and wind speed of the low-level flow. When F is less than the critical value, F_c, a fraction of the flow is assumed to pass around the sides of the orography, and a drag is applied to the flow within this blocked layer. Mountain waves are generated by the remaining proportion of the layer, which the orography pierces through. The acceleration of the flow due to wave stress divergence is exerted at levels where wave breaking is diagnosed. The kinetic energy dissipated through the flow-blocking drag, the mountain-wave drag and the non-orographic gravity wave drag (see Sect. 3.7 below) is returned to the atmosphere as a local heating term.

https://doi.org/10.5194/egusphere-2026-2425
Preprint. Discussion started: 26 May 2026

3.7 Non-orographic gravity wave drag

While orography can force zero phase speed waves, non-orographic sources — such as convection, fronts and jets — induce gravity waves with non-zero phase speed. Momentum deposited when these waves break in the upper stratosphere and mesosphere drives the zonal mean wind and temperature structures away from radiative equilibrium. Waves on scales too small for the model to sustain explicitly are represented by a spectral sub-grid parametrisation scheme of a type proposed by Warner and McIntyre (2001), which represents processes of wave generation, conservative propagation and dissipation by critical-level filtering and wave saturation acting on a vertical wavenumber spectrum of gravity wave fluxes. As described in more detail in Walters et al. (2011), momentum conservation is enforced at launch in the lower troposphere, where isotropic fluxes guarantee zero net momentum, and by imposing a condition of zero vertical wave flux at the model's upper boundary. In between, as the ascending launch spectrum is transformed by conservative propagation and eroded to match the locally evaluated saturation spectrum, the flux integrated across individual layers can reduce due to momentum deposition. The variable source scheme of Bushell et al. (2015) is used whereby the initial gravity wave vertical momentum flux is scaled in proportion to the square root of total precipitation. The mean period of the tropical quasi-biennial oscillation (QBO) is highly sensitive to the scaling parameter for launch level fluxes, which enables tuning to realistic values in present-day simulations.

3.8 Atmospheric boundary layer

Turbulent motions in the atmosphere are not resolved by global atmospheric models, but are important to parametrise in order to give realistic vertical structure in the thermodynamic and wind profiles. Although referred to as the "boundary layer" (BL) scheme, this parametrisation represents mixing over the full depth of the troposphere. The scheme is that of Lock et al. (2000) with the modifications described in Lock (2001) and Brown et al. (2008). It is a first-order turbulence closure mixing adiabatically conserved heat and moisture variables, momentum and tracers. For unstable BLs, diffusion coefficients (K profiles) are specified functions of height within the BL, related to the strength of the turbulence forcing. Two separate K profiles are used, one for surface sources of turbulence (surface heating and wind shear) and one for cloud top sources (radiative and evaporative cooling). The existence and depth of unstable layers is diagnosed initially by two moist adiabatic parcels, one released from the surface, the other from cloud-top. The top of the K profile for surface sources and the base of that for cloud-top sources are then adjusted to ensure that, from the resultant buoyancy flux, the magnitude of the buoyancy consumption of turbulence kinetic energy is limited to a specified fraction of buoyancy production, integrated across the BL. This can permit the cloud layer to decouple from the surface (Nicholls, 1984). This same energetic diagnosis is used to limit the vertical extent of the surface-driven K profile when cumulus convection is diagnosed (through comparison of cloud and sub-cloud layer moisture gradients), except that in this case no condensation is included in the diagnosed buoyancy flux because that part of the distribution is handled by the convection scheme (which is triggered at cloud base). Mixing across the top of the BL is through an explicit entrainment parametrisation that can either be resolved across a diagnosed inversion thickness or, if too thin, is coupled to the radiative fluxes and the dynamics through a sub-grid inversion diagnosis. If the thermodynamic conditions are right, cumulus penetration into a stratocumulus layer can generate additional turbulence and cloud-top entrainment in the stratocumulus

https://doi.org/10.5194/egusphere-2026-2425
Preprint. Discussion started: 26 May 2026

by enhancing evaporative cooling at cloud top. In convective BLs, the scheme includes additional non-local fluxes of heat and momentum that represent the efficient mixing by convective thermals. These generate the vertically uniform potential temperature and wind profiles seen in observations. Primarily for stable BLs and in the free troposphere, diffusion coefficients are also calculated using a local Richardson number scheme based on Smith (1990), with the final coefficients being the maximum of this and the non-local ones described above. The stability dependence in unstable BLs uses the "conventional function" of Brown (1999) that gives only weak enhancement over neutral mixing, as we expect the non-local scheme to be most appropriate in this regime. The stability dependence in stable BLs is given by the "sharp" function over sea and by the "MES-tail" function over land (which matches linearly between an enhanced mixing function at the surface and "sharp" at 200 m and above), as defined in Brown et al. (2008). This additional near-surface mixing is motivated by the effects of surface heterogeneity, such as those described in McCabe and Brown (2007). The resulting diffusion equation is solved implicitly using the monotonically damping, second-order-accurate, unconditionally stable numerical scheme of Wood et al. (2007). The kinetic energy dissipated through the turbulent shear stresses is returned to the atmosphere as a local heating term.

3.9 Convection

The convection scheme represents the sub-grid scale transport of heat, moisture and momentum associated with cumulus cloud within a grid box. The UM uses a mass flux convection scheme based on Gregory and Rowntree (1990) with extensions to include down-draughts (Gregory and Allen, 1991), convective momentum transport (CMT) and a number of other enhancements. The current scheme consists of three stages: (i) convective diagnosis to determine whether shallow convection is possible from the BL; (ii) a call to the shallow scheme for all points diagnosed shallow by the first step; and (iii) a call to the mid-level convection scheme for all grid points.

The diagnosis of shallow convection is based on an undilute parcel ascent from the near surface for grid boxes where the surface buoyancy flux is positive and forms part of the BL diagnosis (Lock et al., 2000). Shallow convection is then diagnosed if the following conditions are met: (i) the parcel attains neutral buoyancy below 2.5 km or below the freezing level, whichever is higher, and (ii) the air in model levels forming a layer of order 1500 m above this has a mean upward vertical velocity less than 0.02 $\mathrm{m\,s^{-1}}$.

The shallow convection scheme uses a closure based on Grant (2001) and has relatively large entrainment rate consistent with cloud-resolving model (CRM) simulations of shallow convection. The shallow CMT uses flux–gradient relationships derived from CRM simulations of shallow convection (Grant and Brown, 1999).

The mid-level scheme operates on any instabilities found in a column at or above the lifting condensation level or above shallow convection, and therefore can represent both surface-driven and elevated convection. It differs from the original Gregory and Rowntree (1990) scheme in a number of important ways. It uses the prognostic dependent entrainment rate as described in Willett and Whitall (2017) and Willett et al. (2026, Sect. 3.5.3.). This allows the convective entrainment rate used to vary over a realistic range of values by linking it to the amount of convective activity within the last several hours, as measured by a 3-dimensional prognostic based on surface convective precipitation, and on the saturated specific humidity at cloud base. The mixing detrainment represents turbulent mixing at the cloud edge, and its rate is set to a fixed fraction of the entrainment rate.

https://doi.org/10.5194/egusphere-2026-2425
Preprint. Discussion started: 26 May 2026

Forced detrainment represents the final detrainment of convective plumes as their buoyancy falls to zero. Mid-level convection uses the adaptive forced detrainment scheme of Derbyshire et al. (2011) whereby the forced detrainment rate adapts to the mean buoyancy of the convective parcel. This allows mid-level convection to represent a spectrum of buoyancies, as would arise from multiple plumes entraining at different entrainment rates, within a single parcel ascent. A convective available potential energy (CAPE) closure based on Fritsch and Chappell (1980) is used with a fixed CAPE timescale of 30 minutes. The CAPE used in the closure will be sensitive to humidity of the environment because it is a dilute value calculated from the entraining parcel ascent. The CAPE is also weighted by the forced detrainment rate as described in Sect. 4.8.2 which introduces sensitivity to the level of convective inhibition into the closure. A numerically more stable version of the Gregory et al. (1997) CMT scheme is used as described in Sect. Willett et al. (2026, Sect. 3.5.2.).

Condensed water in the updraught parcel is converted to precipitation when it exceeds a critical value. This critical value is simply parametrised as a fixed fraction of the local environmental saturated specific humidity ($0.35q_{sat}^{Env}$) bounded by fixed upper ($1\ \mathrm{gkg}^{-1}$) and lower limits ($0.4\ \mathrm{gkg}^{-1}$) (see Walters et al., 2014, Eq.7). The convective precipitation may either evaporate within the downdraught, evaporate in the environment below cloud base, or reach the surface. Detrained convective condensate is converted directly to large-scale cloud condensate and the large-scale cloud fraction is updated using the "injection forcing" method described in Wilson et al. (2008a).

The convection scheme is sub-stepped with two sequential calls to the shallow and mid-level schemes per model time step, with each call using half the full model time step. This was originally introduced to improve the numerical stability of the model.

To mitigate against the detrimental dynamical effects of intermittency within the convection scheme, the potential temperature and humidity increments from the convection scheme as seen by the rest of the model are damped in time with a damping timescale of 45 min as described in Willett et al. (2026, Sect. 3.5.1.)

3.10 Atmospheric aerosols

As discussed in Walters et al. (2011), the precise details of the modelling of atmospheric aerosols and chemistry is considered as a separate component of the full Earth system and remains outside the scope of this document. The aerosol species represented and their interaction with the atmospheric parametrisations is, however, part of the Global Atmosphere component and is therefore included. GAL9 provides the option to use either prognostic aerosols or climatological aerosols with the choice being dependent on the needs of the application (typically climatological aerosols are used for NWP and prognostic aerosols for most other applications).

If prognostic aerosols are used, this is done using the GLOMAP-mode (Global Model of Aerosol Processes) aerosol scheme described in Mann et al. (2010) with updates described in Mulcahy et al. (2018). The scheme simulates speciated aerosol mass and number in four soluble modes covering the sub-micron to super-micron aerosol size ranges as well as an insoluble Aitken mode (Table 3). The prognostic aerosol species represented are sulphate, black carbon, organic carbon and sea salt. For more details see Walters et al. (2019) and Mulcahy et al. (2020).

https://doi.org/10.5194/egusphere-2026-2425
Preprint. Discussion started: 26 May 2026

Aerosol mode	Species	Diameter
soluble nucleation	SO_4 OC	< 10nm
soluble Aitken	SO_4 BC OC	$10 - 100$nm
soluble accumulation	SO_4 BC OC SS	100nm $- 500$nm
soluble coarse	SO_4 BC OC SS	> 500nm
insoluble Aitken	BC OC	$10 - 100$nm

Table 3. The aerosol size distribution in GLOMAP-mode. Species represented are sulphate, black carbon, organic carbon and sea salt.

If climatological aerosols are used, this is done so using three-dimensional monthly climatologies for each aerosol species to model both the direct and indirect aerosol effects. The monthly climatology aerosols fields were derived from a long GA8GL9 N96 AMIP simulation using the prognostic GLOMAP aerosol as described in Sect. 4.9.1.

In GAL9, regardless of the choice prognostic or climatological aerosols, the mineral dust component is simulated using the CLASSIC dust scheme described in Woodward (2011). Functionality to replace CLASSIC mineral dust with GLOMAP mineral dust is under active development and will be included in future configuration.

In addition to the treatment of these tropospheric aerosols, we include simple representations of the radiative impact of stratospheric aerosols, such as those related to injections of SO2 from explosive volcanic eruptions, because the GLOMAP-mode and CLASSIC climatologies do not sufficiently capture sources of stratospheric aerosols. In NWP simulations this is prescribed using a coarse-grain stratospheric aerosol climatology based on Cusack et al. (1998), while in climate simulations we apply the CMIP6 forcing of Thomason et al. (2018) as described in Sect 3.2.1 of Sellar et al. (2020). We also include the production of stratospheric water vapour via a simple methane oxidation parametrisation (Untch and Simmons, 1999).

3.11 Surface flux exchange, land surface and hydrology

The exchange of fluxes between the surface (land, sea and sea-ice) and the atmosphere is an important mechanism for heating and moistening the atmospheric BL. In addition, the exchange of CO_2 and other greenhouse gases plays a significant role in the climate system. The hydrological state of the land surface contributes to impacts such as flooding and drought as well as providing freshwater fluxes to the ocean, which influences ocean circulation. The Global Land configuration uses a community land surface model, JULES (Best et al., 2011; Clark et al., 2011), to model all of these processes in atmosphere/land only and in coupled applications.

In atmosphere/land only applications, the sea surface temperature (SST) is prescribed via an ancillary file. The sea-ice is simply modelled within JULES as a single layer of ice with fixed thickness and areal heat capacity, with the top boundary condition given by the heat flux into the sea-ice and a bottom boundary set to the freezing temperature of sea water. The surface temperature is determined from the surface energy balance using the gradient between the surface and ice temperatures, with a fixed thermal conductivity. Although the details of coupling between the atmosphere, ocean and sea-ice models when running in coupled simulations lie outside the scope of this paper, it is useful to note, however, where the boundaries lie between

https://doi.org/10.5194/egusphere-2026-2425
Preprint. Discussion started: 26 May 2026

JULES, and the ocean and sea-ice components when GAL9 is run in coupled mode as part of GC5. In GC5, the SST is set to be equal to the temperature of the 1 m-thick, top ocean layer, which is calculated within the ocean model, with JULES being used to calculate the surface fluxes that are subsequently passed back to the ocean. Over the sea-ice, JULES is used to calculate both the skin temperature of the top sea-ice layer and the surface fluxes, because this has been shown to be both more accurate and more numerically stable than calculating them within the sea-ice model (West et al., 2016).

A tile approach is used to represent sub-grid scale heterogeneity of the land-surface (Essery et al., 2003b), with the surface of each land grid box subdivided into five types of vegetation (broadleaf trees, needle-leaved trees, temperate C3 grass, tropical C4 grass and shrubs) and four non-vegetated surface types (urban areas, inland water, bare soil and land ice). The ground beneath vegetation is coupled to the vegetation canopy by LW radiation and turbulent sensible heat exchanges. JULES also uses a canopy radiation scheme to represent the penetration of light within the vegetation canopy and its subsequent impact on photosynthesis (Mercado et al., 2007). The canopy also interacts with falling snow. Snow buries the canopy for most vegetation types, but the interception of snow by both needle-leaved and broad-leaved trees is represented with separate snow stores on the canopy and on the ground. This impacts the surface albedo, the snow sublimation and the snow melt (Essery et al., 2003a). The vegetation canopy code has been adapted for use with the urban surface type by defining an "urban canopy" with the thermal properties of concrete (Best, 2005), and evaluates well for the surface heat and moisture fluxes (Grimmond et al., 2011; Lipson et al., 2023).

Following Best et al. (2011), this canopy approach has also been adopted for the representation of inland water[4]. By defining an "inland water canopy" and setting the thermal characteristics to those of a suitable mixed layer depth of water ($\approx 5\,\mathrm{m}$), a better diurnal and seasonal cycle for the surface temperature is achieved than for the original "permanently saturated soil" approach (Rooney and Jones, 2010). The depth of the water in the canopy is held fixed, but global water conservation is pragmatically ensured by a small global adjustment to the water content of the deepest soil level (with appropriate checks to avoid negative values or supersaturation) in response to water fluxes into and out of the inland water canopies. The surface below the inland water canopy is essentially decoupled from the canopy, and hence it plays no role in the model's evolution.

Following Best et al. (2011) and as described in more detail in Wiltshire et al. (2020), land ice is represented by using the soil scheme with the soil parameters set to appropriate values for ice, i.e., the thermal characteristics are set to those of ice, whilst the other soil parameters are set to zero. This means that it is not possible to have both land ice and other surface types in the same grid box, as they share the same soil profile; hence, if land ice is present in the model, then it must cover 100% of the grid box. Furthermore, to reduce the likelihood of small scale sharp horizontal gradients which could lead to numerical problems, only large areas of land ice are permitted in the model, e.g. in most climate simulations, only Antarctica and Greenland are included. Land ice is typically initiated at the start of integrations with a large amount of overlying snow to ensure that not all of the snow can be removed through sublimation or melt during the simulation. In addition, as the lateral transfer of snow by glacial movement is not represented in the model, it is possible to accumulate very large amounts of snow. However, this does not adversely impact on the surface energy balance. The surface temperature is not allowed to go above the melting

[4]Noting that the largest lakes - e.g. the Caspian Sea, the Great Lakes, Lake Victoria etc. - are treated as sea points in all applications and hence are not represented in this manner.

https://doi.org/10.5194/egusphere-2026-2425
Preprint. Discussion started: 26 May 2026

temperature, but instead the associated energy is used to melt the snow. Infiltration of this snow melt, along with any liquid precipitation, is not permitted into the land ice, but is directed to surface runoff.

Surface fluxes are calculated separately on each tile using surface similarity theory. In stable conditions we use the stability functions of Beljaars and Holtslag (1991), whilst in unstable conditions we take the functions from Dyer and Hicks (1970). The effects on surface exchange of both BL gustiness (Godfrey and Beljaars, 1991) and deep convective gustiness (Redelsperger et al., 2000) are included. Temperatures at 1.5 m and winds at 10 m are interpolated between the model's grid levels using the same similarity functions, but a parametrisation of transitional decoupling in very light winds is included in the calculation of the 1.5 m temperature.

The roughness length for the bare soil is specified via an ancillary file that is based on Prigent et al. (2012) and the roughness lengths for all other land type are explicitly specified. Over the sea surface the COARE (Coupled Ocean–Atmosphere Response Experiment) 4.0 (Edson, 2009) momentum roughness length parametrisation is used. At very high wind speeds over the sea the drag coefficient is gradually reduced from a maximum value of 3×10^{-3} at 33 ms^{-1} to a limiting value of 2×10^{-3} at 55 ms^{-1} in agreement with observed estimates (e.g. Donelan et al., 2004; Donelan, 2018; Curcic and Haus, 2020). The form drag for marginal ice uses the explicit representation from Lupkes et al. (2012) which is validated in Renfrew et al. (2019).

The snow-free albedo for each land surface type uses the radiative transfer model of Sellers (1985) with each surface type using prescribed visible and near-infrared, and direct and scattering coefficients. The grid-box mean albedo of the land surface is further modified in the presence of snow. The albedo of the ocean surface is a function of the wavelength, the solar zenith angle, the 10 m wind speed and the chlorophyll content according to the Jin et al. (2011) parametrisation. The emitted LW radiation is calculated using a prescribed emissivity for each surface type.

Soil processes are represented using a 4-layer scheme for the heat and water fluxes with hydraulic relationships taken from Brooks and Corey (1964). These four soil layers have thicknesses from the top down of 0.1, 0.25, 0.65 and 2.0 m. The impact of moisture on the thermal characteristics of the soil is represented using a simplification of Johansen (1975), as described in Dharssi et al. (2009). The energetics of water movement within the soil is accounted for, as is the latent heat exchange resulting from the phase change of soil water from liquid to solid states. Sub-grid scale heterogeneity of soil moisture is represented using the Large-Scale Hydrology approach (Gedney and Cox, 2003), which is based on the topography-based rainfall-runoff model TOPMODEL (Beven and Kirkby, 1979). This enables the representation of an interactive water table within the soil that can be used to represent wetland areas, as well as increasing surface runoff through heterogeneity in soil moisture driven by topography.

A river routing scheme is used to route the total runoff (from all land surface types including land ice) from inland grid points both out to the sea and to inland basins (where it can flow back into the soil moisture). If the soil at inland basin points becomes saturated and hence unable to hold more water, the resultant runoff is pragmatically redirected evenly across all sea outflow points. The resulting increase in the river outflow is always very small and does not affect the ocean salinity structure in any significant way, but importantly this process ensures global water conservation which is an important criterion for global climate models. In coupled model simulations the resulting freshwater outflow is passed to the ocean, where it is an important component of the thermohaline circulation, whilst in atmosphere/land-only simulations this ocean outflow is purely

https://doi.org/10.5194/egusphere-2026-2425
Preprint. Discussion started: 26 May 2026

diagnostic. River routing calculations are performed using the TRIP (Total Runoff Integrating Pathways) model (Oki and Sud, 1998), which uses a simple advection method (Oki, 1997) to route total runoff along prescribed river channels on a $1^\circ \times 1^\circ$ grid using a 3 h time step. Land surface runoff accumulated over this time step is mapped onto the river routing grid prior to the TRIP calculations, after which soil moisture increments and total outflow at river mouths are mapped back to the atmospheric grid (Falloon and Betts, 2006). This river routing model is not currently being used in NWP implementations of the Global Atmosphere/Land and hence any runoff is purely diagnostic and "lost" from the model's water budget.

3.12 Stochastic physics

A key component of many Ensemble Prediction Systems (EPSs) is the use of stochastic physics schemes to represent model error emerging from unrepresented or coarsely resolved processes such as numerical diffusion or fluctuations in the impact of physical parametrisations on the large-scale fields. The addition of unresolved variability around the deterministic solution adds spread between ensemble members and has been shown to improve ensemble predictions in the medium range (Palmer et al., 2009; Tennant et al., 2011) as well as on seasonal (Weisheimer et al., 2011) and decadal time scales (Doblas-Reyes et al., 2009). The increase in the model's internal variability also helps to improve the model's climatology, through a noise-drift induced process. In particular, there is strong evidence of the positive impact of stochastic physics schemes on specific processes such as mid-latitude blocking (Berner et al., 2012), the Madden–Julian Oscillation (MJO, Madden and Julian, 1971; Weisheimer et al., 2014) and North Atlantic weather regimes (Dawson and Palmer, 2015).

In GAL9, we use a standardised package of stochastic physics schemes (Sanchez et al., 2016) based on an improved version of the Stochastic Kinetic Energy Backscatter scheme version 2 (SKEB2, Tennant et al., 2011) and the Stochastic Perturbation of Tendencies scheme (SPT) with additional constraints designed to conserve energy and water. SKEB2 adds forcing to the large-scale flow to represent the backscatter of small-scale kinetic energy lost via numerical diffusion, whilst SPT stochastically scales the output of physical parametrisations to represent variability about their mean predictions.

Despite the positive impact of model error stochastic physics schemes on EPS and climate model performance by making probability forecasts more statistically reliable and reducing the error of the ensemble mean, their formulations fundamentally add noise which degrades forecast skill when run in deterministic mode (Sanchez et al., 2016). For these reasons, these schemes are not used in deterministic forecast systems, which are designed to forecast the best possible single prediction of the atmosphere's future state.

3.13 Global atmospheric energy correction

Long climate simulations of the Unified Model include an energy correction scheme, designed to ensure that numerical errors, inconsistent geometric assumptions and missing processes do not lead to any spurious drift in the atmosphere's total energy. The scheme accumulates the net flux of energy through the upper and lower boundaries of the atmosphere over a period of $1\,\mathrm{day}$ and calculates the difference between this and the change in the atmosphere's internal energy. Any drift is compensated by the addition of a globally uniform temperature increment, which is applied every time step for the following day. In GAL9, the magnitude of these corrections is typically $\lesssim +0.3\,\mathrm{W\,m^{-2}}$.

https://doi.org/10.5194/egusphere-2026-2425
Preprint. Discussion started: 26 May 2026

3.14 Ancillary files and forcing data

In the UM, the characteristics of the lower boundary, the values of climatological fields and the distribution of natural and anthropogenic emissions are specified using ancillary files. Use of correct ancillary file inputs can play as important a role in the performance of a system as the correct choice of many options in the parametrisations described above. For this reason, we consider the source data and processing required to create ancillaries as part of the definition of the Global Atmosphere/Land configurations. Table 4 contains the main ancillaries used as well as references to the source data from which they are created.

Table 4. Source datasets used to create standard ancillary files used in GAL9.

Ancillary field	Source data	Notes
Land mask/fraction	System dependent	
Mean/sub-grid orography	GMTED; Danielson and Gesch (2011)	Fields filtered before use
	RAMP2; Liu et al. (2015)	Antarctica only. Fields filtered before use.
Land usage	CCI; Poulter et al. (2014)	Mapped to 9 tile types
Soil properties	HWSD; Nachtergaele et al. (2008)	Three datasets blended via optimal interpolation
	STATSGO; Miller and White (1998)	
	ISRIC-WISE; Batjes (2009)	
Leaf area index	MODIS collection 5	4 km data (Samanta et al., 2012) mapped to 5 plant types
Plant canopy height	IGBP; Loveland et al. (2000)	Derived from land usage and mapped to 5 plant types
Bare soil albedo	MODIS; Houldcroft et al. (2008)	
TOPMODEL topographic index	Marthews et al. (2015)	
SST/sea ice	System/experiment dependent	
Sea surface chlorophyll content	GlobColour; Ford et al. (2012)	
Ozone	System/experiment dependent	
GLOMAP-mode emissions/fields:		Only required for prognostic aerosol simulations.
Anthropogenic emissions	CEDS-CMIP6; Hoesly et al. (2018)	Includes SO_2, black carbon and organic carbon
Biomass Burning	GFED-CMIP6; van Marle et al. (2017)	
Volcanic SO_2 emissions	Dentener et al. (2006)	
Aerosol precursor oxidants	UKESM1.1 CMIP6 simulation Mulcahy et al. (2023)	
Ocean DMS concentrations	Lana et al. (2011)	
GLOMAP-mode aerosol climatologies	GA8GL9 AMIP simulation with prognostic aerosols Willett et al. (2026)	Used when prognostic fields not available
TRIP river paths	1° data from Oki and Sud (1998)	Adjusted at coastlines to ensure correct outflow

https://doi.org/10.5194/egusphere-2026-2425
Preprint. Discussion started: 26 May 2026

4 Developments since GA8GL9

The subject of this paper, GAL9, will be the next science configuration of the Global Atmosphere and Global Land models and it builds upon GA8GL9 (Willett et al., 2026). This section gives a description of all the changes added between GA8GL9 and GAL9.

4.1 Surface flux exchange, land surface and hydrology

4.1.1 Surface tile albedo improvements, unification of soil parameters and transpiration/soil moisture dependence improvements (GMED ticket #527)

The main motivation for changes to the land surface component in GAL9 has been to consolidate the science between the global and regional model configurations. Hence, three aspects of the land surface model have been addressed in the GAL9 configuration; surface albedo, soil hydraulics and the relationship between transpiration and soil moisture stress.

In the land surface scheme, the albedo is specified separately for direct and diffuse radiation and is also split between the visible and near-infrared regions of the spectrum. Generally, the direct albedo is higher than the diffuse albedo when the sun is low in the sky, but lower when it is closer to the zenith, while many natural surfaces are more reflective in the near infrared region. The albedo of vegetation canopies is calculated using the equations provided by Sellers (1985) with leaf reflection and scattering coefficients mainly taken from Dorman and Sellers (1989). In GL6 Walters et al. (2017), a scheme was introduced to scale the leaf reflection and transmission coefficients so as to improve the agreement with the climatologies of visible and near-infrared albedos provided by GlobAlbedo (Lewis et al., 2012): this slightly improved the simulation of near-surface air temperatures. However, it is not possible to apply this scaling in simulations where the surface properties may evolve as will be the case in many climate change experiments, so it has been removed and the underlying albedo scheme has been revised.

The equations given in Sellers (1985) for the scattering of direct radiation apply only in the case of isotropic scattering by leaves, although the standard optical properties represent rather anisotropic scattering: it was recognized that this discrepancy contributed to our previous inability to make use of the direct components of the albedo. The scheme was therefore extended to apply to anisotropic direct scattering. Moreover, in CLM4 (Lawrence et al., 2011), it was found that the optical parameters of leaves given by Dorman and Sellers (1989) imply too much reflection in the near-infrared, and they were replaced by values taken from Asner et al. (1998). Similarly, we replace the original values with values derived from more recent spectral databases of leaf optical properties. Specifically, we derive the scattering and reflection coefficients for broad-leaved tress from the data for Downy Oak in LOPEX93 (Hosgood et al., 1993), those for C3 grass from the spectra for Timothy grass, and those for C4 grass from the spectra for Johnson Grass, both from the same compilation. The values for shrubs are derived from the spectra for woody plants given in Asner et al. (1998). The coefficients for needle-leaved trees are taken from the spectra for black spruce given in Lukeš et al. (2013) with an adjustment for multiple scattering within shoots (Smolander and Stenberg, 2005). There is considerable variation between spectra, and we have in part chosen spectra for representative plants to minimize differences between values calculated and retrieved albedos. Following these changes and the extension of the canopy snow scheme to broad-leaved trees, we retuned the parameters affecting the masking of vegetation by snow.

https://doi.org/10.5194/egusphere-2026-2425
Preprint. Discussion started: 26 May 2026

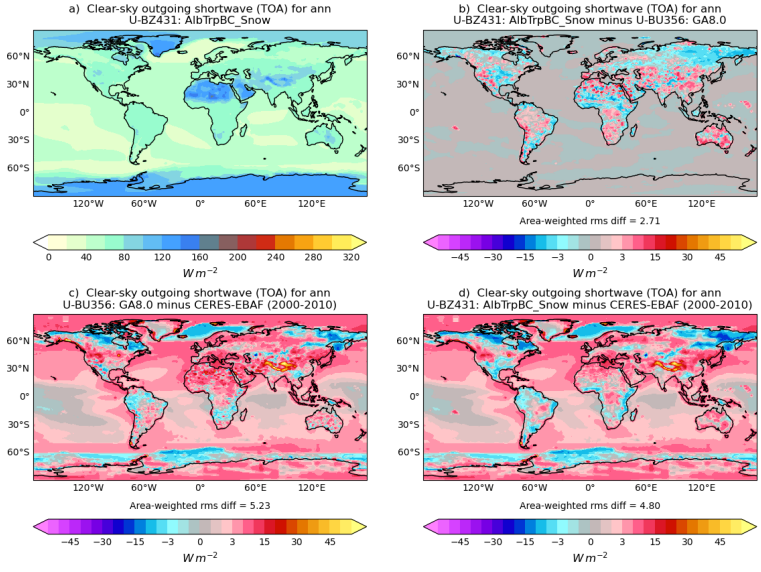

Figure 1. Annual mean top-of-atmosphere clear-sky reflected SW radiation (Wm^2) in a 20-year N96 atmosphere/land only climate simulations compared to Clouds and Earth's Radiant Energy System (CERES) Energy Balanced and Filled (EBAF)dataset version 4.1 (NASA/LARC/SD/ASDC, 2019) showing (a) The package of surface changes, (b) the difference between the surface package and GA8GL9, (c) bias in GA8GL9 relative to CERES-EBAF and (d) bias in the surface package relative to CERES-EBAF.

Previously, the soil albedo at a point was specified as a single broad-band value without any separation between the visible and near-infrared spectral regions, or between direct and diffuse radiation. In reality, soils are more reflective at infrared wavelengths, so in GAL9 we disaggregate the broadband value between these spectral regions, assuming that incident radiation is equally split between the two regions and that the value in the near-infrared value should be twice that in the visible. We introduce a dependence of the direct albedo on the solar zenith angle by assuming a Lommel-Seliger bidirectional radiance distribution function (BRDF), as discussed by Hapke (1981): the BRDF is thus a function of the radiative similarity parameter, which is inferred from the diffuse albedo in the ancillary file.

Collectively, the changes to the albedo improve the simulation of the clear-sky reflected SW radiation relative to CERES-EBAF without any climatological scaling of the albedo, as shown in Fig. 1.

JULES has two soil hydraulic options, namely the Brookes and Corey (BC) scheme (Brooks and Corey, 1964) and the Van Genuchten (VG) scheme (van Genuchten, 1980). For code efficiency reasons, only a simplified version of the VG scheme was implemented, which enabled the two schemes to use the same soil parameter ancillary information. However, results from global and climate simulations have demonstrated that this implementation can result in lofted soil moisture in the upper soil layers due to the rapid decrease in hydraulic conductivity with decreasing soil moisture. Hence, this can result in drier soil layers below wetter ones with some soil types resulting in an unrealistic soil moisture profile. Improving the VG implementation to remove these issues is a longer term objective, but was beyond the GAL9 configuration development

https://doi.org/10.5194/egusphere-2026-2425
Preprint. Discussion started: 26 May 2026

timescale. The decision was therefore made to adopt the BC hydraulics scheme instead. A comparison between these two hydraulics schemes implemented in JULES does indeed show that the soil moisture in the top soil layer with the BC scheme is reduced compared to VG because the water has been able to drain to the lower layers.

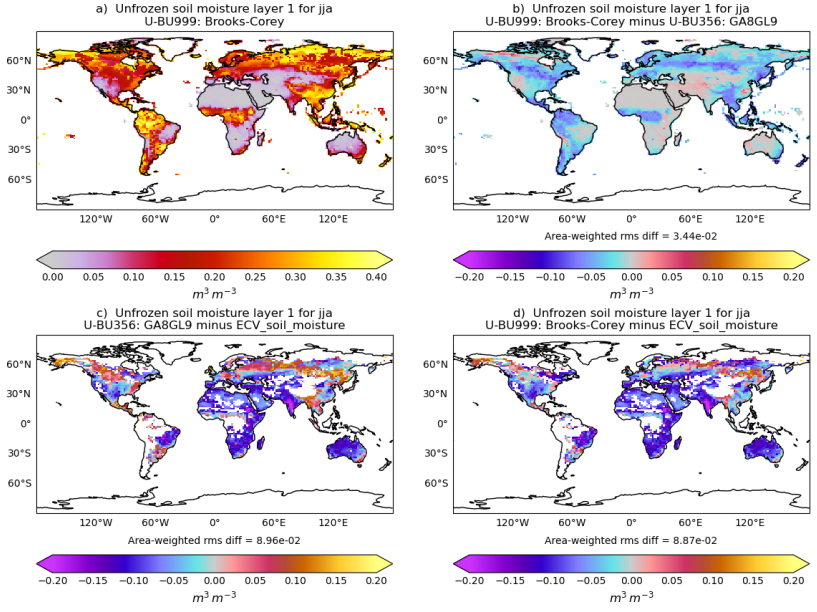

Figure 2. June-August mean unfrozen soil moisture for for the upmost soil layer ($\mathrm{m^3 m^{-3}}$) in a 20-year N96 atmosphere/land only climate simulations compared to ECV soil moisture (Dorigo et al., 2017; Gruber et al., 2019) showing (a) The GA8GL9+BC, (b) the difference between GA8GL9+BC and GA8GL9, (c) bias in GA8GL9 relative to ECV and (d) bias in the GA8GL9+BC relative to ECV.

The impact on transpiration from the limitation of soil moisture is represented by a simple function in JULES that scales between zero and one. For soil moisture above a reference value, the function is set to one and transpiration is not impacted by the soil moisture, hence is at the potential rate. For soil moisture below the wilting point the function is set to zero to prevent any transpiration. For the range of soil moisture between the wilting point and the reference soil moisture, the function scales linearly between zero and one and multiplies the potential transpiration value (Best et al., 2011). This function is determined for each soil layer and then implemented through a normalised density of the roots within that layer.

In previous configurations of the model, the reference soil moisture was set to the critical point. However, stand-alone evaluation studies of the JULES land surface model have shown that this results in transpiration decreases too rapidly as the soil moisture dries beyond the critical point (Verhoef and Egea, 2014). In GAL9, the reference point is set to 60 % of the difference between the wilting point and the critical point. Transpiration, therefore, is maintained at the potential rate until the soil moisture drops below $\beta = \theta_{wilt} + 0.6\,(\theta_{crit} - \theta_{wilt})$, where β is the soil moisture stress function and θ is the soil moisture.

https://doi.org/10.5194/egusphere-2026-2425
Preprint. Discussion started: 26 May 2026

4.1.2 Fix unrealistic surface temperatures (GMED ticket #604)

A new diagnostic for the maximum time step surface temperature over an hour highlighted unrealistic extreme temperatures in the model. Investigations showed that this was a time step phenomenon that occurred in environments with high solar fluxes and dense cloud cover. In these situations, the longer radiation time steps enabled the surface to cool until the lowest part of the boundary layer became stable. If the cloud then cleared on the next radiation time step, there would then be a large amount of SW radiation reaching the surface.

The issue in the model resulted from the surface exchange coefficients being calculated explicitly using the temperature gradients from the previous time step. In this case, when the previous time step had a stable boundary layer profile, heat could not be transported effectively away from the surface by turbulence, so the only other mechanisms to transport the heat away from the surface were through LW exchange and the soil heat flux, resulting in unrealistically high surface temperature.

Updating the surface temperature within the surface exchange iteration removed the inconsistency between the previous time step conditions and the instantaneous surface radiation fluxes leading to more realistic, smoothly varying surface temperatures.

4.2 Sub-grid orographic drag

4.2.1 Account for moist processes in the GWD scheme (GMED ticket #451)

Atmospheric gravity waves require a stably stratified atmosphere. The level of stability, as quantified by the Brunt-Vaisala or buoyancy frequency, N, affects the surface stress, wave propagation, wave breaking and the flow blocking depth within the GWD scheme (e.g. Vosper, 2015), and hence it is clearly very important.

Prior to GAL9, the effects of water vapour and latent heat release on atmospheric stability were ignored in the GWD scheme. In GAL9, the calculation of the buoyancy frequency, N, has been modified to account for the virtual effects of water vapour, grid box saturation on resolved scales, and latent heat release during low-level saturated sub-grid orographic ascent (Table 5). The last of these is most important and it significantly reduces the effective stability seen by the orographic drag scheme. Blocked layer depths are significantly reduced via smaller Froude numbers, greatly reducing long-standing negative near-surface wind biases over mountains in coarse resolution simulations. Wave drag magnitudes are also modified, and the orographic drag scheme switches off more frequently as it is now able to identify moist instability. In isolation this change results in increased wind speeds, but this is offset by the tuning discussed in Sect. 4.12.

GA8GL9	GAL9
$N_d^2 = \frac{g}{\theta}\frac{d\theta}{dz}$	$N_{unsat}^2 = \frac{g}{\theta_v}\frac{d\theta_v}{dz}$
	$N_{sat}^2 = \frac{g}{T}\left(\frac{dT}{dz} + \Gamma_s\right)\left(1 + \frac{L_v q}{R_d T}\right) - \frac{g}{1+q_T}\frac{dq_T}{dz}$

Table 5. Buoyancy frequency, N, as used in the GWD scheme in its dry form only in GA8 and the unsaturated and saturated forms used in GAL9. θ, θ_v and T are potential temperature, virtual potential temperature and temperature respectively. q is water vapour mixing ratio and q_T is the total water mixing ratio. Γ_s is the saturated adiabatic lapse rate. R_d is the gas constant for dry air.

https://doi.org/10.5194/egusphere-2026-2425
Preprint. Discussion started: 26 May 2026

More detail of the modifications to account for moist processes in the GWD scheme and testing of the scheme is given in Smith (2021).

4.2.2 Targeted smoothing of orography (GMED ticket #599)

High-resolution ensemble forecasts have been previously troubled by instabilities around regions of steep orography where the model sometimes develops a positive feedback between vertical velocity and surface fluxes resulting in failures akin to grid-point storms. These issues were found to be strongly geographically located to a handful of grid-points where the orography slopes exceeded a certain amount, most notably in the southwestern slopes of the Himalayas. The ensemble forecasts were especially impacted because of perturbations to the model state, which are required to generate spread in the ensemble, tend to explore more of the phase-space than the deterministic forecasts. To mitigate this problem in GAL9, we apply a blending scheme to the orography processing that reduces the amplitude of these problematic steep slopes.

The targeted smoothing scheme uses two orography fields. The first is a field with the desired level of fine-scale detail and roughness to give the best forecasts. The second is a smoother version of the orography that you are confident will not lead to forecast instabilities. It then blends these two fields, replacing the fine-scale orography with the smooth orography at points where the slope of the fine-scale orography exceeds the maximum slope of the smooth orography. To avoid step changes in the blended field we use a Butterworth filter to smooth out the blending mask such that there is a gradual transition between the two orography fields over a length-scale of approximately 120 km. This step is iterated (up to a maximum of 30 iterations) until there are no slopes in the blended orography that exceed the original deemed safe maximum taken from the smooth orography.

Because it targets steep slopes, the targeted smoothing of orography has no effect on the orography used at N96 and N216, and has only a tiny effect at N320. Even at N640 and N1280, only a small number of points are modified by this process.

Testing after the freeze of GAL9 revealed that targeted smoothing was over smoothing at N1280. This necessitated that branch configuration GAL9.1 which is discussed further in Sect. 6.

4.3 Non-orographic gravity wave drag

4.3.1 Source of non-orographic gravity waves that depends on total precipitation (GMED ticket #298)

With an appropriately tuned invariant source amplitude of non-orographic gravity waves, GA8 can generate model QBOs with realistic mean periods and amplitudes: intercycle variations, however, are typically under-represented but this may be improved by introducing greater spatial and temporal variability into the source. A further incentive to introduce meteorologically interactive sources at GAL9 is to enable a feedback pathway for parametrised gravity waves, which are known to contribute significantly to driving trends in the stratospheric Brewer-Dobson circulation, in response to climate change. Ultimately, an evolution to multiple source representations (e.g. from convection, frontal or shear zones) is envisaged. However, successful implementation in a global model requires identification of a sufficiently complete source set and a solution to the challenge of partitioning without duplication in more complex situations where several sources might coexist. As a pragmatic development approach, GAL9 replaces the invariant source with a simple empirical relationship between precipitation and gravity wave ver-

https://doi.org/10.5194/egusphere-2026-2425
Preprint. Discussion started: 26 May 2026

tical momentum flux that was derived from an analysis of a high-resolution, convection-permitting simulation of the tropical Indian Ocean as described in Bushell et al. (2015). Other characteristics of the launch spectrum, such as its shape, isotropy or launch altitude, remain unaltered. Hence, the launch flux at height z_l and azimuth direction $\hat{\mathbf{k_0}}(\phi_j)$

$$\mathbf{F_{ptot}}(z_l, \phi_j) \;=\; \mathrm{C_{pf}} \left[Max\left(1,\, \frac{\mathrm{P}(\lambda,\phi,\mathrm{t})}{\mathrm{P_{base}}}\right)\right]^{\frac{1}{2}} \hat{\boldsymbol{k_0}}(\phi_j) \tag{1}$$

where $\mathrm{P_{base}}$ ($1.1574 \times 10^{-6}\,\mathrm{kg\,m^{-2}\,s^{-1}}$) is a threshold value equivalent to $0.1\,\mathrm{mm\,day^{-1}}$, $\mathrm{P}(\lambda,\phi,\mathrm{t})$, in $\mathrm{kg\,m^{-2}\,s^{-1}}$, is the total precipitation at longitude λ, latitude ϕ and time t and parameter $\mathrm{C_{pf}}$ ($7.20507 \times 10^{-4}\,\mathrm{m^{-2}\,s^{-2}}$) scales the amplitude of gravity waves generated by the total precipitation sources.

Comparison of the invariant and variable source performance in the global model is made easier by tuning baseline amplitude factor $\mathrm{C_{pf}}$ such that the mean launch flux over several years between latitudes $75°N - 75°S$ from the variable and invariant sources match. For scaling parameter $\mathrm{C_{l0}}$ ($3.4191 \times 10^{-9}\,\mathrm{s^{-2}}$) and wavenumber spectrum peak $m_* = (2\pi/4300)\,\mathrm{m^{-1}}$ the invariant source flux is $\mathrm{C_{l0}}\, m_*^{-2}$. Hence:

$$\frac{\mathrm{P}(\lambda,\phi,\mathrm{t})}{\mathrm{P_{base}}} \;=\; \left(\frac{\mathrm{C_{l0}}}{\mathrm{C_{pf}}}\right)^2 m_*^{-4} \tag{2}$$

Local strengths from the precipitation source will match those from the invariant for a precipitation rate $\approx 0.49\,\mathrm{mm\,day^{-1}}$ ($0.02\,\mathrm{mm\,h^{-1}}$). The new variable source exhibits far greater spatial and temporal variability (Fig. 3) than the invariant source (the only variation comes from its dependence on air density at the launch level). In tropical summer regions, where convection generates most of the total precipitation, the outcome resembles a scale independent convective source flux but there are also strong contributions from the extra-tropical winter precipitation zones. In contrast, at polar latitudes and in the subtropical subsidence regions, GAL9 actually launches less subgrid gravity wave flux than GA8. Comparisons under nudged conditions reported in Bushell et al. (2015) showed that these differences are eroded on ascent through the model atmosphere because larger fluxes are more likely to reach the saturation threshold for dissipation at lower altitudes where their momentum is deposited to accelerate the mean wind flow. Although the possibility of feedback in free-running global models leads to a more complicated response, the tendency toward enhanced launch fluxes in GAL9 relative to GA8 close to the equator and suppressed towards the subtropics can broadly be seen to support the maintenance of realistic QBO periods for lower levels of non-orographic gravity wave fluxes away from the equator. This in turn acts to amplify a reduction of drag on jets in the extratropical upper stratosphere in response to other science changes in GAL9.

4.4 Solar and terrestrial radiation

4.4.1 Improve cloud droplet optical properties including Optimal MCICA sampling to reduce noise (GMED ticket #518)

The radiation configuration has had a minor update from GA8. Principal changes are to the representation of the water vapour continuum while minor updates have also been made to the cloud optical properties including an adjustment to the sub-grid cloud sampling to reduce noise.

https://doi.org/10.5194/egusphere-2026-2425
Preprint. Discussion started: 26 May 2026

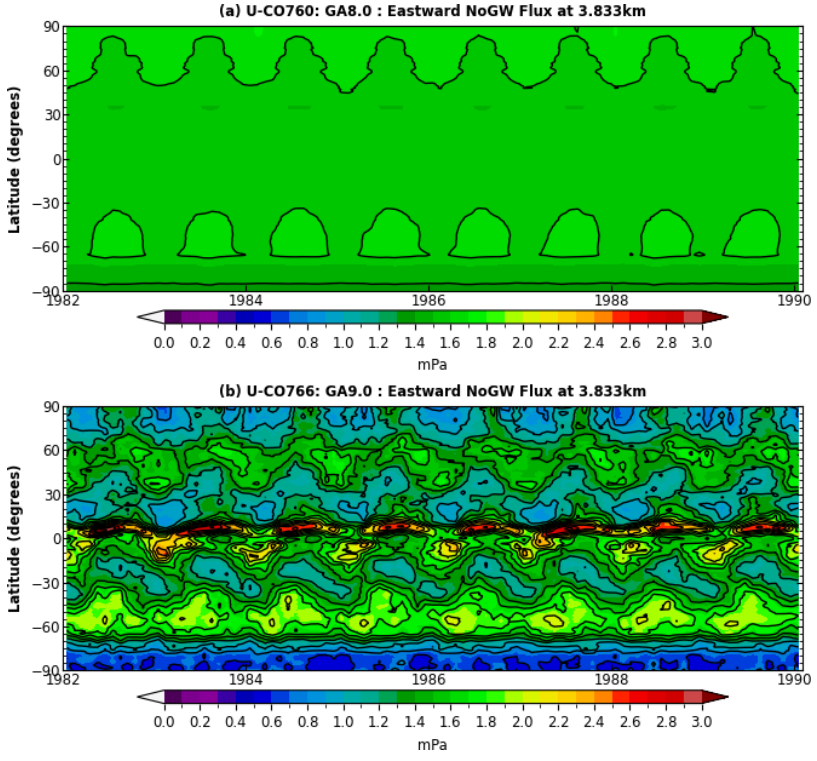

Figure 3. Time-latitude Hovmoller plot of the zonal-mean parametrised non-orographic gravity wave flux at the launch level for the eastward azimuthal direction for 8 years of N216 AMIP simulations using (a) GA8 and (b) GAL9.

An update to the CAVIAR (Continuum Absorption at Visible and Infrared wavelengths and its Atmospheric Relevance) water vapour continuum has been provided by Jon Elsey and Keith P. Shine (private communication), motivated by several advancements in understanding since the original version used with GA7 and GA8. The original CAVIAR continuum used laboratory measurements between 1 and 5 μm (Ptashnik et al., 2011) supplemented by version 2.5 of the Mlawer-Tobin_Clough-Kneizys-Davies (MT_CKD2.5) model (Mlawer et al., 2012) at other wavelengths. The MT_CKD version has now been updated to 3.2 (Mlawer et al., 2019) with particular increases in the far-infrared continuum. Additional updates are based on near-infrared in-band measurements from Ptashnik et al. (2019) and Birk et al. (2020), window measurements in the 4, 2.1 and 1.6 μm windows from Cavity Ring-Down Spectroscopy (CRDS) e.g. Mondelain et al. (2014); Ventrillard et al. (2015); Richard et al. (2017) and an increased understanding of CAVIAR lab measurements with respect to inconsistencies in the temperature dependence (Elsey et al., 2020). The net effect is to reduce water vapour absorption in the near-infrared window regions.

The cloud droplet optical properties used with GA8 were unchanged since the GA3 configuration where SW bands 2 and 3 both represented the wavelength range 0.32 - 0.69 μm. These have now been recalculated for GAL9 to represent the new band limits for SW bands 2 and 3 (now split into 0.32 - 0.505, 0.505 - 0.69 μm) weighted using the solar spectrum.

https://doi.org/10.5194/egusphere-2026-2425
Preprint. Discussion started: 26 May 2026

The sub-grid cloud sampling that is done as part of the Monte Carlo Independent Column Approximation (MCICA) has been enhanced to over-sample the k-terms that are most sensitive to cloud with a further 10 monochromatic calculations in the SW and 6 in the LW. This reduces the random sampling noise in the radiative fluxes and heating rates.

The impact in NWP tests of this change is very small apart from the reduced spatial noise in instantaneous radiative fluxes. In climate tests the mean outgoing SW is increased by approximately 0.5 Wm^{-2}, but this is readily compensate for within the wider tuning exercise (Sect. 4.12).

4.5 Large-scale precipitation

4.5.1 Seeder Feeder sub-grid orographic precipitation enhancement (GMED ticket #319)

The "seeder-feeder" mechanism, whereby precipitation falling from an upper level "seeder" cloud is enhanced by accretion as it falls through a lower level "feeder" cloud, is a significant process in the orographic enhancement of precipitation (Bergeron, 1965). Prior to GAL9, this process will be under represented because it does not account for the variability in the orography at scales that are not explicitly resolved. In GAL9, the representation of this process is improved by including the seeder-feeder sub-grid orographic precipitation enhancement parametrisation of Smith et al. (2016) with the further enhancements described in Smith et al. (2019). This change is designed to represent rain enhancement due to laminar flow over sub-grid mountains. It estimates the increase in grid-box mean cloud liquid-water mixing ratio, accounting for regions where the actual surface is both higher and lower than the model surface. This sub-grid orographic water estimate is used to enhance the growth of rain (snow) via accretion (riming) within the large-scale precipitation scheme (Sect. 3.4). This change increases the large-scale precipitation over orography, but the wider impacts are small.

More details on the original design of the scheme, and results of idealised tests, are given in Smith et al. (2016). The enhancements to account for the effect on the amount of sub-grid orographic water of flow blocking in small Froude number situations, and verification of the scheme within the Unified Model, are given in Smith et al. (2019).

4.5.2 Linking ice-nucleation temperature to prognostic-dust aerosols (GMED ticket #481)

Nucleation of ice crystals from atmospheric aerosols is sensitive to the physical and chemical characteristics of ice-nucleating aerosols as well as to atmospheric conditions. The most prevalent ice-nucleating species in simulations is mineral dust, which in GAL9 is provided by the prognostic dust scheme described in Woodward (2011). In previous GA versions, an aerosol-independent threshold temperature for ice nucleations was assumed in the convection scheme, below which the convection parametrisation switched to detraining condensed water mass as ice (more precisely, a linear function was used to gradually change the phase of detrained condensate between two fixed temperature values). In the large-scale precipitation (microphysics) scheme, when below a threshold temperature, an empirical formula, based on Fletcher (1962) is used to calculate a heterogeneous freezing rate and convert a small quantity of cloud liquid to ice. In GAL9, a simple and pragmatic scheme is added to link the ice nucleation in convection and microphysics to prognostic dust concentration. The threshold temperature for ice nucleation smoothly decreases as dust-number concentration increases from a typical heterogeneous nucleation temperature of

https://doi.org/10.5194/egusphere-2026-2425
Preprint. Discussion started: 26 May 2026

-10 °C at higher dust concentrations to the homogeneous freezing temperature at very low concentrations. Note that the GAL9 dust scheme prognoses dust mass in either two or six size bins depending on the requirements of the application. These are converted to a total diagnostic dust number assuming spherical particles with radii representative of each bin. In the convection scheme, this leads to convective clouds in dusty regions, such as over subtropical land masses, detraining ice at relatively warm temperatures; in contrast in pristine environments, such as over the oceans remote from major dust sources, convection has to penetrate to colder temperatures before becoming a source of ice. In the large-scale precipitation scheme, heterogeneous freezing occurs when temperatures are below the same dust-dependent threshold. Despite the additional complexity of the scheme, when the sensitivity of ice-nucleation temperature to dust aerosols is tuned to have a physically plausible value, the effect on the scheme on cloud phase is relatively minor.

4.6 Large-scale cloud

4.6.1 Bimodal cloud initiation for PC2 (GMED ticket #493)

The PC2 cloud scheme's (Wilson et al., 2008a) initiation term can generate some cloud during clear-sky conditions, or introduce partial cloudiness during completely overcast conditions, when the subgrid saturation-departure distribution is conducive to such changes. Prior to GAL9, this initiation term followed the Smith (1990) diagnostic cloud scheme, assuming a symmetric, unimodal, triangular subgrid saturation-departure distribution. However, this approach typically produced insufficient cloud cover compared to observations, particularly in environments characterized by sharp atmospheric inversions and boundary layer entrainment processes.

In GAL9, the Smith formulation is replaced with a bimodal diagnostic cloud scheme (Van Weverberg et al., 2021a, b). The scientific foundation rests on recognising that atmospheric moisture variability within model grid boxes often exhibits non-Gaussian characteristics, particularly in regions influenced by entrainment processes near atmospheric inversions. The bimodal scheme allows the subgrid saturation-departure probability-density function to be both skewed and bimodal. This enables representation of two distinct variability modes, typically associated with different air mass characteristics above and below entrainment zones. The scheme operates by identifying entrainment zones near sharp atmospheric inversions, where coexisting distinct air masses create bimodal moisture distributions. Within these zones, cloud fraction and liquid water content calculations account for the dual-mode structure while conserving grid-box mean saturation departure. For equivalent relative humidity conditions, this approach typically generates larger cloud fractions and enhanced liquid water content compared to the original formulation. The entrainment zone diagnosis is not performed above 3 km to prevent excessive mid-level cloud formation. Further to the description in Van Weverberg et al. (2021b), an additional requirement is introduced into GAL9 that the entrainment zones need to have subcritical Richardson numbers; this change improves consistency with future planned physics. Note that the PC2 initiation term creates liquid cloud only, but takes into account vapour competition in mixed-phase clouds following Field et al. (2014), using the prognostic PC2 ice cloud fraction and water content, rather than a diagnostic ice cloud fraction as in Van Weverberg et al. (2021b).

https://doi.org/10.5194/egusphere-2026-2425
Preprint. Discussion started: 26 May 2026

Comprehensive evaluation of N96 AMIP climate simulations and N320 case study simulations, demonstrated generally increased and improved low-level cloud coverage and liquid water content, predominantly over the tropics and oceanic regions, but also over mid-latitude continental areas during JJA. Radiative impacts included generally stronger (and more biased) SW cloud forcing over oceanic regions, but improved LW cloud forcing characteristics. The modifications showed minimal impact on surface temperature and precipitation fields, indicating successful addressing of identified deficiencies while maintaining overall model physical consistency.

4.6.2 Implicit cloud erosion (GMED ticket #615)

The cloud erosion scheme represents the effects of the mixing of sub-saturated clear air and saturated cloudy air around the cloud edge and is described in Morcrette (2012). This process acts to reduce the liquid condensate and cloud fraction in a grid box (cloud erosion is only applied to liquid cloud and not ice cloud). Equation 3 describes the erosion of liquid condensate in its continuous form.

$$\left(\frac{\partial \overline{qcl}}{\partial t}\right)_{eros} = A\left(C_l\right) K\left(q_{sat} - q_v\right) \tag{3}$$

$A\left(C_l\right)$ is the area of the cloud edge as described in Morcrette (2012) and K is the fixed erosion rate. Prior to GAL9, this was discretised in a time explicit form as:

$$\Delta qcl_{eros} = \Delta t A\left(C_l^n\right) K\left(q_{sat} - q_v\right) \tag{4}$$

where Δqcl_{eros} is the liquid cloud condensate increment due to erosion. Unfortunately, this could suffer from numerical overshoot resulting in the scheme attempting to remove more condensate than was available (although additional checks prevent this). Furthermore, the erosion was applied in parallel to the homogenous forcing from convective detrainment with the increments from both processes being summed together. The combination of these factors resulted in the cloud erosion being overly sensitive to the model time step.

In GAL9, Eq. (3) is rewritten as:

$$\left(\frac{\partial \overline{qcl}}{\partial t}\right)_{eros} = \overbrace{qcl}^{fast} \frac{\overbrace{A\left(C_l\right) K\left(q_{sat} - q_v\right)}^{slow}}{qcl} \tag{5}$$

The right hand side has been split into a term that will evolve rapidly with erosion and a term that will evolve more slowly because erosion will reduce both the numerator and denominator. In the discretisation the fast term will be treated implicitly and the slow term explicitly in time as follows:

$$\Delta qcl_{eros} = \Delta t\, qcl^{n+1} f^n \tag{6}$$

https://doi.org/10.5194/egusphere-2026-2425
Preprint. Discussion started: 26 May 2026

where $f^n = \frac{A(C_l^n)K(q_{sat}-q_v)}{qcl^n}$. The liquid water at time level $n+1$ includes the contributions from both erosion and homogenous forcing from convection, i.e. $qcl^{n+1} = qcl^n + \Delta qcl_{eros} + \Delta qcl_{conv}$, and hence after some rearrangement the increment due to cloud erosion can be written as:

$$\Delta qcl_{eros} = \Delta t f^n qcl^n \frac{1 + \frac{\Delta qcl_{conv}}{qcl^n}}{1 - f^n \Delta t} \tag{7}$$

It can be seen that this is equivalent to the explicit form in Eq. (4) but with an addition scaling term. This form guarantees a positive solution for qcl and has been shown in single column model testing to be far less sensitive to the model time step.

In isolation this change generally increases cloud in stratocumulus and shallow convective dominated regions, whilst reducing it elsewhere. However, a particular advantage is that it is now practical to use the cloud erosion rate (which is not well constrained by theory or observations) as a tuning parameter and this was done as part of the tuning discussed in Sect. 4.12.

4.7 Boundary layer

4.7.1 Use Ri-based diffusion across PBL top except with strong inversions (GMED ticket #433)

Until now, the diffusion coefficient derived from the local Richardson number (Ri) has been set to zero across the top of all boundary layers, so that its potentially unrealistic behaviour there does not overrule the fluxes across the inversion generated by the non-local scheme (this is especially important in cloud-capped boundary layers since the static stability for Ri has to be interpolated and how to calculate the moist stability is not well defined, see Sect. 4.7.3). Here we relax this behaviour to only set to zero where a sharp inversion is diagnosed (one where the non-local scheme parametrises the entrainment fluxes explicitly). This means the Ri-based diffusion is now active at weak inversions (including those resolved across multiple grid levels and at cumulus cloud base), and so able potentially to give some representation of mixing driven by local wind shear. This change results in a reduction in low cloud although the magnitude of the change is much smaller than some of the other changes that affect low cloud (e.g. the bimodal cloud initiation in Sect. 4.6.1 and implicit cloud erosion in Sect. 4.6.2). The wider effects of this change are small.

4.7.2 Revised TKE and variance diagnostics (GMED ticket #513)

The diagnosed higher order turbulence moments (TKE and variances of vertical velocity, temperature and humidity) include terms proportional to the scalar fluxes. Previously these were represented using down-gradient diffusion but now we use the parametrised fluxes directly. As well as being more accurate, this avoids an issue where the non-local BL scheme parametrises entrainment fluxes across sharp inversions explicitly and sets the diffusion coefficients there to zero, which has led to zero TKE and variances being diagnosed. The impact of this change is generally small with just some minor changes in low cloud being the most significant effect.

https://doi.org/10.5194/egusphere-2026-2425
Preprint. Discussion started: 26 May 2026

4.7.3 Revised calculation of buoyancy gradient in Ri (GMED ticket #559)

In the BL scheme, the Richardson number (Ri), which measures the ratio of buoyancy and shear forces, is used to calculate the local diffusion coefficient (Sect. 3.8).

With the Charney–Philips vertical grid staggering, Ri is required on the same grid levels as scalars (referred to as θ-levels), where the vertical gradient of horizontal momentum naturally falls. Previously, the gradients of liquid-ice static energy temperature and total water content were interpolated to θ-levels and that θ-level's cloud fraction used to obtain the buoyancy gradient required for the numerator of Ri. For clouds below a strong inversion, such as stratocumulus, the combination of interpolated gradients and saturated buoyancy calculation has been found to lead to spurious apparent instability. Here the buoyancy gradient is now calculated locally (on ρ-levels) and interpolated to θ-levels. This then requires an estimate of the vertical fraction of the grid containing saturated air on ρ-levels, which is done by interpolating the supersaturation from the adjacent θ-levels. For the stratocumulus example above, this means the contribution from the ρ-level with strong gradients is typically largely unsaturated, leading to strong stability, which then remains stable when averaged with the saturated ρ-level with weak gradients below.

In isolation, this change increases the amount of low-cloud and outgoing SW in stratocumulus regions, and the net downward radiation at the top of the atmosphere is reduced by about 1.0 Wm^{-2}.

4.8 Convection

4.8.1 Align mid-level convection and deep convection (GMED ticket #507)

In previous configurations mid-level convection and deep convection use different science settings for entrainment, initiation level and initial parcel buoyancy perturbation. In GAL9 we make these science settings in mid-level convection more consistent with those for deep convection. The following changes are made:

- Switching on the prognostic based entrainment rate (ProgEnt) in mid-level convection. This was added to deep convection in GA8 and is outlined in (Willett et al., 2026, Sect. 3.5.3.) and described in more detail in Willett and Whitall (2017). ProgEnt allows the convective entrainment rate used to vary over a realistic range of values by linking it to the amount of convective activity within the last several hours, as measured by a 3-dimensional prognostic based on surface convective precipitation, and on the saturated specific humidity at cloud base. This is justified on the premise that locations that have experienced high levels of recent convective activity will be populated with relatively large convective clouds that have low entrainment rates: conversely, locations that have experienced low levels of recent activity will be populated with relatively small convective clouds (if any) that will have high entrainment rates.

- Prior to GAL9, shallow and deep convection could only be initiated from the top of the turbulently mixed layer (`ntml`). In contrast, mid-level convection was only allowed to initiate from 2 levels above the turbulent mixed layer or higher (`ntml+2`) to avoid mid-level convection being coupled directly to surface driven boundary-layer mixing. In GAL9 this restriction is relaxed so that mid-level convection can initiate from the top of the turbulent mixed layer (`ntml`) or higher.

https://doi.org/10.5194/egusphere-2026-2425
Preprint. Discussion started: 26 May 2026

– Prior to GAL9, mid-level convection used an fixed initial parcel buoyancy perturbation that only perturbed potential temperature. In contrast, the initial parcel buoyancy perturbation in deep convection is related to the environmental buoyancy gradient at cloud base and applied by enforcing saturation (in a manner analogous to that used in shallow convection); consequently, the buoyancy perturbation is mainly achieved by perturbing the parcel's humidity. In GAL9, the fixed initial parcel perturbation is retained but it achieved by perturbing the humidity (subject to some restrictions discussed in Sect 4.8.4).

The big remaining difference between mid-level and deep convection would be the diagnosis/triggering. This ticket will not be addressing this difference.

In isolation, the impact of this change is small. The most notable change is a small reduction in SW cloud forcing (0.2 Wm^{-2} in the annual mean) due to mid-level convection being able to vent more moisture from the BL and hence reduce the amount of boundary layer cloud. This change, however, should be seen as a prerequisite to switching off the separate deep convection as discussed below in Sect. 4.8.3.

4.8.2 Forced detrainment weighted CAPE calculation (GMED ticket #508)

The convection scheme uses a CAPE closure. The CAPE used in the closure is a dilute CAPE, i.e. it is reduced by entrainment. The convection scheme attempts to represent an ensemble of plumes through the adaptive forced detrainment (Derbyshire et al., 2011). This accounts for the fact that plumes have a spectrum of buoyancies and hence terminate at different levels. The closure, however, sees the dilute CAPE at the top of the parcel ascent, i.e. it sees the CAPE of the very deepest plume. It does not account the fact that some plumes terminate lower down. This problem is exacerbated by the fact that the adaptive detrainment can increase the parcel buoyancy at the expense of reduced mass flux (prior to the closure). In this scenario the CAPE used in the closure (which depends only on the parcel buoyancy) can increase when it encounters a convective inhibition (CIN), but the pre-closure mass flux, and hence dCAPE/dt, is reduced. The net effect of this is that when the standard CAPE closure is applied, the final mass flux can be larger with CIN than without CIN. This is an undesirable consequence on the combination of adaptive detrainment and the standard CAPE closure.

The standard calculation of CAPE between the cloud base, z_b, and height, z, is:

$$\mathrm{CAPE}(z) = \int_{z_b}^{z} \frac{\theta_v^P - \theta_v^E}{\theta_v^E} g \mathrm{d}h \tag{8}$$

where θ_v^P and θ_v^E are the virtual potential temperatures of the dilute parcel and its environment respectively. In GA8 the CAPE used in the closure is calculated using Eq. 8 with z equal to the height of the cloud top, z_t, to give $\mathrm{CAPE}(z_t)$.

In GAL9 we replace the $\mathrm{CAPE}(z_t)$ as used in the closure by a measure of CAPE that is weighted in the vertical by the mass flux that is undergoing forced detrainment. We will refer to this quantity as FCAPE. This is calculated as follows:

https://doi.org/10.5194/egusphere-2026-2425
Preprint. Discussion started: 26 May 2026

$$\mathrm{FCAPE} = \frac{\int_{z_b}^{z_t} M\delta \mathrm{CAPE}(z)\,\mathrm{d}z}{\int_{z_b}^{z_t} M\delta\,\mathrm{d}z} \tag{9}$$

where $M\delta$ is the mass flux detrained by forced detrainment at height z. FCAPE will always be smaller than CAPE. FCAPE then replaces CAPE in the cloud base mass flux closure equation, i.e.:

$$M(z_b) = M_0(z_b)\,\frac{\mathrm{FCAPE}}{\tau \left.\frac{\partial \mathrm{CAPE}}{\partial t}\right|_0} \tag{10}$$

where the subscript 0 indicates quantities calculated using the arbitrary initial mass flux prior to the closure being applied, τ is the CAPE timescale and $\frac{\partial \mathrm{CAPE}}{\partial t}$ is the rate of destruction CAPE due to the convective updraught between z_b and z_t. Note that FCAPE, like CAPE, is independent of the cloud base mass flux.

The impact of this change is in general small with the most notable difference being a very small cooling (<0.05 K) in the tropical tropospheric temperatures. It should, however, address a problem very occasionally seen in the model whereby deep convection penetrates a low-level inversion and generates excessive precipitation. In such an instance, FCAPE will be far smaller than the standard CAPE and hence the application of the closure will result in far less precipitation.

4.8.3 Switch off deep convection (GMED ticket #557)

Prior to GAL9, there were three distinct types of convection used: shallow and deep convection, which were driven from the surface, and mid-level convection, which could only initiate above the boundary-layer top. As described above in Sect. 4.8.1, mid-level convection is modified in GAL9 to reduce the differences between it and deep convection, and this included the ability to initiate from the top of the turbulently mixed layer (which is defined to be equal to the LCL for points diagnosed as convecting) in the same manner as for shallow and deep convection. These changes make the need for a separate deep convection scheme essentially redundant because it can be replaced by the revised mid-level scheme. In GAL9, therefore, the deep convection scheme is switched off.

The convection diagnoses step is still performed as in previous configurations. As before, if shallow convection is diagnosed then shallow convection is initiated from the LCL. However, although deep convection can still be diagnosed in GAL9, the deep convection scheme is not initiated. Instead mid-level convection is tested for at all points including those diagnosed as deep convection and at all levels at or above the LCL. Almost all points that are diagnosed as deep convection can also support mid-level convection from the LCL because the two schemes are very similar albeit not identical (the initial perturbation being the most significant difference). Therefore, despite the name, mid-level convection is able the represent deep, surface driven convection in a similar manner to the previous deep convection scheme.

The second part of this change is that the CAPE timescale, which in the previous two configurations (GA7GL7 and GA8GL9) was a function of the large-scale vertical velocity as described in Walters et al. (2019), is now fixed at 30 minutes. This change is

https://doi.org/10.5194/egusphere-2026-2425
Preprint. Discussion started: 26 May 2026

motivated by several factors. The relationship between the large-scale vertical velocity and CAPE timescale, which is the basis for the w-based CAPE timescale, was derived using high resolution model data and using an undilute calculation of CAPE. This was justifiable approximation in the context of deep and mid-level convection in GA7 that both used low entrainment rates and hence dilute CAPE values that do not greatly differ from undilute CAPE. However, prognostic entrainment, which was introduced for deep convection at GA8 and is now used for mid-level convection in GAL9, can access much higher entrainment rates and increase the difference between undilute and dilute CAPE. Furthermore, the forced detrainment weighted CAPE (described above in Sect. 4.8.2) will further increase this difference. Consequently, undilute CAPE, which was used in the derivation of the w-based CAPE timescale, and dilute FCAPE, which is used in GAL9, can take very different values for the same thermodynamic profile, and hence the w-based CAPE timescales are no longer valid. In GAL9, therefore, we take the pragmatic approach to use a simple fixed CAPE timescale in the closure. However, it should be noted that even with the fixed CAPE timescale, the CAPE closure in GAL9 does not just depend on CAPE but it will be sensitive to relative humidity (because of the entrainment) and CIN (through the forced detrainment weighted CAPE). Furthermore, it will be indirectly sensitive to the large-scale dynamics due to the effect of the large-scale dynamics on RH, CAPE and CIN.

A notable benefit of switching off deep convection is the consistency over the diurnal cycle over land. Previously, deep convection would typically operate over land during the day and mid-level convection would operate overnight. Differences in their diagnoses and especially their initial perturbations would often result discontinuity during late afternoon when neither scheme would operate. This issue is fixed in GAL9 because only mid-level convection is operating (shallow convection is still operating but is very rarely diagnosed over land). The net effect is that the phase of the diurnal cycle is improved in GAL9 relative to GA8GL9 with the phase error of the diurnal harmonic being reduced by typically 1.5 hrs (Table 6). It should be noted that the prognostic based entrainment in mid-level convection is a necessary condition for this improvement; i.e. if deep convection is switched off without prognostic entrainment being switched on in mid-level convection, the error in the phase of the diurnal harmonic is similar to that in GA8GL9.

	MAM	JJA	SON	DJF
GA8	4.3	4.7	4.3	5.0
GA8+align mid	4.9 (+0.6)	4.8 (+0.1)	4.8 (+0.5)	5.3 (+0.3)
GA8+align mid+no deep	2.5 (-1.8)	3.0 (-1.7)	2.8 (-1.5)	3.2 (-1.8)
GAL9-ProgEnt	4.4 (+0.1)	4.2 (-0.5)	4.4 (+0.1)	4.8 (-0.2)
GAL9	2.8 (-1.5)	3.1 (-1.6)	2.9 (-1.4)	3.4 (-1.6)

Table 6. Median absolute phase error in hours in the seasonal-mean diurnal-harmonic for land points between 40S and 40N for N96 GA8GL9, GA8GL9+align mid (Sect. 4.8.1), GA8GL9+aligned mid+no deep, GAL9-ProgEnt, and GAL9 configurations relative to GPM IMERG V06B (Huffman et al., 2020a, b). The seasonal mean diurnal cycles from the model configurations are aggregated using 20 years of 3-hourly instantaneous precipitation rates. The seasonal mean diurnal cycle for GPM IMERG was aggregated from 10 years of 3-hourly instantaneous precipitation rates and regridded to the model grid using area-averaged weighting. The values in brackets are differences from the GA8GL9 values.

https://doi.org/10.5194/egusphere-2026-2425
Preprint. Discussion started: 26 May 2026

4.8.4 Improved treatment of mid-level initial parcel perturbation (GMED ticket #613)

In GAL9, the initial parcel buoyancy perturbation in mid-level convection is set to the following:

$$\theta_v'^P = 0.5\frac{\Delta p}{5000}\mathrm{K} \tag{11}$$

where Δp is the pressure thickness of the initiating level in Pa. If convection is initiated from a typical oceanic lifting condensation level, then the pressure thickness scaling term is ~ 0.2 which gives a typical initial buoyancy perturation of $\sim 0.1\,\mathrm{K}$. The unscaled buoyancy perturbation, set to 0.5 K here, is a tuneable parameter and was set to this value as part of the tuning (Sect. 4.12).

In most circumstances the buoyancy perturbation is generated by solely perturbing the parcel humidity. However, several limits are applied to the humidity perturbation to prevent it becoming too large. In the initial development the initial humidity perturbation was limited so that the following conditions were met.

- less than $q^E_{sat} - q^E$ to prevent the parcel becoming supersaturated (unless the environment was supersaturated).
- less than $0.2\,q^E_{sat}$ to prevent the parcel perturbation exceeding 20 % relative humidity
- less than q^E to prevent the perturbation being larger than the environmental humidity

After these limits are applied the remaining buoyancy perturbation is then applied by perturbing the potential temperature.

Tests using these conditions would very occasionally fail due to small negative humidities being generated. In this change these limits are tightened with the final condition being replaced by:

- less than $0.8\,q^E$ to prevent the perturbation being larger than 80 % of the environmental humidity.

The impact of these changes on climate or NWP simulations is exceedingly small, but it does prevent the numerical failures which were caused by very small negative humidities. An additional check to ensure that the humidity perturbation does not become negative was also added.

4.9 Aerosols

4.9.1 GLOMAP-mode climatological aerosols (GMED ticket #498)

Prognostic aerosols cannot be used in all applications because of the high computational cost, but climatological aerosols do provide a computationally cheaper alternative where the simpler representation is acceptable. Prior to GAL9, applications that used aerosol climatologies (typically NWP) were derived from the single moment (mass only) CLASSIC aerosol scheme (Bellouin et al., 2011) as opposed to the two moment (mass and number concentration) GLOMAP-mode (Mann et al., 2010; Mulcahy et al., 2018) which is used with prognostic aerosols. For some time, it has been desirable to improve the consistency between prognostic and climatological representations of aerosols by moving to a GLOMAP-mode based climatology.

https://doi.org/10.5194/egusphere-2026-2425
Preprint. Discussion started: 26 May 2026

	Soluble modes				Insoluble modes		
Components	Nucleation	Aitken	Accumulation	Coarse	Aitken	Accumulation	Coarse
Number	No	Yes	Yes	Yes	Yes	No	No
Sulphate	No	Yes	Yes	Yes	-	-	-
Black Carbon	-	Yes	Yes	Yes	Yes	-	-
Organic Carbon	No	Yes	Yes	Yes	Yes	-	-
Sea Salt	-	-	Yes	Yes	-	-	-
Dust	-	-	-	-	-	No	No

Table 7. GLOMAP modes and components used in GAL9 with climatological aerosols. Number is the number of particles in each mode per molecule of air. Sulphate, black carbon, organic carbon, sea salt and dust are stored as mass mixing ratios.

Aerosols affect the model evolution through their direct effect on radiation and their indirect effect on CDNC, which are used by the radiation and large-scale precipitation schemes respectively (Sect. 3.3 and 3.4). To develop a computationally efficient mechanism for representing the effects of aerosols using a GLOMAP-mode based climatology, three questions were considered: (1) what is the minimum set of fields that need to be returned from UKCA to the parent model, (2) could we replace the calculation of the aerosol fields with a climatological average, and (3) what are the minimum required calculations to be able to pass those fields.

In consideration of the first question, the minimum set of fields to be returned from UKCA is the CDNC, which gets passed to the large-scale precipitation and radiation schemes, and a number of fields which describe the aerosols (mean particle dry diameters of each mode, mean wet diameter of each soluble mode, particle density of each mode, partial volume of water of each soluble mode, and partial volume of each aerosol component), which get passed to RADAER where the SW and LW absorption, scattering and asymmetry are calculated before being passed to the radiation scheme.

The second question has led to a hybrid solution for GAL9. Climatology aerosol fields are used for all soluble modes to generate the CDNC field. For four of the six modes in Table 7, we also obtain the required fields to pass to RADAER. For dust, however, we retain the single moment Classic prognostic dust scheme (this is also used with prognostic aerosols).

The seventeen aerosol climatology fields (4 number modes plus 13 mass mixing ratios as per Table 7), were produced from a twenty year AMIP climatological run at a low model resolution (N96). At each grid box, a monthly mean was obtained and a twenty year mean for each month was calculated in post processing. Monthly averages represents the middle of the month and a simple interpolation is used for the specific start date. To reduce the cost of reading the aerosol climatologies, NWP applications typically do not update the aerosols from the climatologies during the course of the forecast.

In order to minimise computational cost of using climatological aerosols, the “GLOMAP_Clim” interface was created. GLOMAP_Clim is essentially a set of pipework designed to bypass the majority of UKCA, and instead call a small subset of science modules within the UKCA repository in order to efficiently return only the minimum required fields.

https://doi.org/10.5194/egusphere-2026-2425
Preprint. Discussion started: 26 May 2026

There are several available methods for calculating CDNC within UKCA. When the GLOMAP-mode aerosol climatologies are used with GAL9, the computationally inexpensive method described by Jones et al. (1994) is usually used in preference to the UKCA-Activate scheme (West et al., 2014), which is used with prognostic aerosols, because UKCA-Activate is too computationally expensive for NWP applications. The method of Jones et al. (1994) results in systematically higher CDNC, and hence lower cloud droplet effective radius and increased outgoing SW flux, than the Abdul-Razzak and Ghan (2000) method in UKCA-Activate. The global mean outgoing SW flux is approximately 3 Wm^{-2} higher with GLOMAP-mode climatologies and the Jones et al. (1994) activation scheme than with prognostic GLOMAP-mode and UKCA-Activate, with most of the difference due to the choice of aerosol activation scheme. In climate simulations this would result in the outgoing SW being slightly too large and a gradual drift towards a cooler state, but this is considered acceptable given the large computational cost saving and the intended use in NWP applications where the state of the system is constrained by the DA.

4.9.2 Improve SO_2 dry deposition in GLOMAP-mode aerosol scheme (GMED ticket #500)

This ticket implements a set of improvements to the parametrisation of the dry deposition of SO_2, a key trace gas precursor to sulfate aerosol. These changes were first implemented in UKESM1.1 and documented fully in Mulcahy et al. (2023) and Hardacre et al. (2021). The dry deposition velocity of a trace gas species such as SO_2 is calculated in the model as the inverse sum of a set of resistances representing the aerodynamic resistance (r_a), the quasi-laminar sublayer resistance (r_b) and the surface resistance (r_c) following Wesely (1989). The developments here refer specifically to the surface resistance term for SO_2 which is dependent on the underlying surface properties and atmospheric conditions (eg. temperature, humidity). Previously the r_c value for SO_2 took no account of the surface moisture conditions of the surface, despite the high solubility of SO_2. A scheme is now implemented which makes r_c for SO_2, over vegetated surfaces, a function of surface wetness (determined from the simulated precipitation rates) or near surface relative humidity if the surface is classed as dry. In addition, the surface resistance values for C3 and C4 crop surface types are reduced to represent irrigated crops, reduced from 209.8 scm^{-1} (C3) and 196.1 scm^{-1} (C4) to 30.0 scm^{-1} for both surface types. Finally, the r_c value for SO_2 over water surfaces is also reduced from 10 scm^{-1} to 1 scm^{-1} consistent with settings in UKESM1.1. The scheme is described and evaluated in detail in Hardacre et al. (2021). The changes lead to an increase in the dry deposition of SO_2, particularly close to anthropogenic sources over land, reducing global SO_2 concentrations and subsequently sulfate aerosol. The changes reduce biases in surface concentrations of SO_2 at observation sites over North America and Europe although pre-existing negative biases in sulfate aerosol at European and Northeastern US sites are slightly degraded. The changes and subsequent weaker effective radiative forcing from sulfate aerosol significantly improved the simulation of historical surface temperature in UKESM1.1, removing the large cold bias in UKESM1.0 (Mulcahy et al., 2023).

4.9.3 Update chemical oxidants in offline oxidant aerosol scheme (GMED ticket #503)

In GAL9, the offline oxidants used to drive the GLOMAP-mode aerosol scheme were updated. This change accounts for the latest science developments in the UK Earth System Model's full chemistry scheme - the UK Chemistry and Aerosol (UKCA) model's StratTrop scheme (Archibald et al., 2020) – and will make GAL9 more consistent with UKESM1.1 simulations

https://doi.org/10.5194/egusphere-2026-2425
Preprint. Discussion started: 26 May 2026

conducted for CMIP6. The five oxidant species accounted for (O_3, NO_3, OH, H_2O_2 and HO_2) are the same as previous versions. The new oxidants were generated from one realization of the UKESM1.1 CMIP6 historical simulation (Mulcahy et al., 2023). The atmospheric concentrations of the updated offline oxidants were generally around 25% higher than the previous version and increases the amount of ozone (O_3) and OH available for the oxidation of SO_2 to sulphate aerosol. The main impact of this change was therefore increased sulphate concentrations, increasing the global burden in total atmospheric sulphate from 9.83 to 10.47 Tgy^{-1}. Surface sulphate concentrations increased by up to 20% between approximately 0-30 ° S, and over source regions including the northeastern USA, India and China, offsetting to some degree the degradation in model bias over Europe and northeastern USA reported in Sect. 4.9.2. Subsequent higher CDNCs enhance the cooling from clouds and lead to a decrease in the net downward radiation at the top of atmosphere by 0.3 Wm^{-2}.

4.9.4 Improvements to carbonaceous aerosol absorption (GMED ticket #515)

In GAL9 two new tuning options are provided for Black Carbon (BC) absorption properties. These reduce absorption efficiency, or so-called Mass Absorption Coefficient (MAC) to correct for a high bias resulting from the simplified representation of aerosol mixing. In GLOMAP-mode and the associated RADAER scheme that computes optical properties, aerosols are represented as homogeneous internally mixed spheres and the refractive index is calculated as the volume-weight average of the components present. This approximation is computationally efficient but, as highlighted in various studies (e.g. Zhang et al., 2019; Taylor et al., 2020), can lead to an overestimation of MAC relative to more realistic approaches where BC is modelled either as a core or as separate inclusions within a mixed particle. Evaluations based on GA7.1 AMIP simulations (same BC settings as GA8) showed the global annual mean value of MAC to be around 17 $\mathrm{m}^2\mathrm{g}^{-1}$ for 514 nm, which is on the high side compared to observational constraints (Bond et al., 2013). Whilst BC MAC is highly variable depending on particle size and composition a recent analysis of aircraft observations in Taylor et al. (2020) suggested values 20 – 30% lower than those in GA7.1, at around 14 $\mathrm{m}^2\mathrm{g}^{-1}$ (their Figure 3e) for aged carbonaceous aerosol mixtures containing BC from biomass burning and evaluated various alternatives to the homogeneous mixed approach.

One potential improvement over the approach in GA8 is to switch to a more complex refractive index mixing rule, such as the Maxwell-Garnet approximation (Markel, 2016). This arguably offers a more realistic optical model for aerosol mixtures containing BC and typically results in a lower MAC than volume-weighted averaging. The increased complexity of the mixing equation however adds substantial computational cost to RADAER and the radiation scheme as a whole. Another means of correcting for the high bias in MAC is to increase the assumed mass density of BC, which decreases the volume of BC and therefore its contribution to the refractive index of the mixture. BC mass density in GA8 and earlier configurations has a value of 1500 kgm^{-3}, representing an acceptable middle point in a wide range of published estimates (e.g. Bond and Bergstrom, 2006; Bond et al., 2013) and this remains the default (untuned) value in GAL9. However, increasing density to a higher value such as 1800 or 1900 kgm^{-3} remains consistent with the range recommended in Bond and Bergstrom (2006) and is compatible with the assumed BC refractive index of 1.85 + 0.71i that was adopted from that study in GA8.

The BC tuning options available in GAL9 are therefore two-fold, but the first option is the recommended default:

https://doi.org/10.5194/egusphere-2026-2425
Preprint. Discussion started: 26 May 2026

1. BC mass density is increased from 1500 to 1900 kgm^{-3}. Recommended option, reducing BC absorption by around 21%. No added computational cost.

2. Refractive index is calculated via the Maxwell-Garnet approximation and BC mass density is increased from 1500 to 1800 kgm^{-3}. Recommended only for development and dedicated aerosol-radiation studies, due to substantial increase in RADAER runtime. Reduces BC absorption by around 27%.

4.9.5 Use ASAD Newton Raphson column-call chemical solver for offline-oxidants configuration (GMED ticket #551)

The offline-oxidants chemical scheme, used to drive the GLOMAP-mode aerosol scheme, is described in detail in Section 2.5 and Table 3 of Mulcahy et al. (2020) and has not changed from GA8 (Willett et al., 2026). However, the chemical solver used has been updated to use the same chemical solver used in the UK Earth System Model, UKESM (Archibald et al., 2020; Sellar et al., 2019), which is an implicit backward Euler solver that uses Newton-Raphson iteration (Esentürk et al., 2018). This has benefits as it reduces technical debt and means that solver improvements developed for UKESM also benefit GA configurations and vice versa. As with UKESM, the chemical time step is 1 hour, and it is called over columns to preserve bit-comparability when changing the decomposition. A fix to the chemical tendencies of sulphuric acid from this solver is also included (Ranjithkumar et al., 2021). As this is a technical change there is no scientific impact.

4.9.6 Emit all SO_2 at the surface (GMED ticket #584)

GA8 and previous GA configurations injected SO_2 from half of industrial and all of energy sector emissions at a height of 500 m, to represent thermally lofted emissions from cooling towers and industrial chimneys. All other SO_2 was emitted at the surface. This approach for SO_2 was different from that for corresponding primary aerosol emissions from these sectors, which are emitted at the surface then mixed by the boundary layer scheme. To make emissions of SO_2 and primary aerosol consistent, and to make GAL9 consistent with the CMIP6 simulations of UKESM1 (Sellar et al., 2020), GAL9 emits all SO_2 and primary aerosol at the surface. This change increases the dry deposition of SO_2, reducing the total atmospheric burden of SO_2 and sulphate aerosol. This results in small reductions in clear-sky and all-sky outgoing SW radiation in AMIP simulations (approx 0.2 Wm^{-2} and 0.3 Wm^{-2}, respectively). Mulcahy et al. (2020) analyse the impact of an equivalent change in UKESM1 and find that it has minimal impact on the comparison of surface sulphate aerosol against observations (their section 5.2.1).

4.10 Dynamical formulation and discretisation

4.10.1 Fountain buster (GMED ticket #492)

It has been found that the UM semi-Lagrangian (SL) advection scheme can lead to single grid-column updraughts becoming unrealistically intense and persistent (an "eternal fountain"), because a stagnation point forms at the base of the updraught. The fountain buster works by identifying grid points where the winds converge into a stagnation point and applies a simple linear upwind advection increment to add in the effects of convergent inflow missed by the SL advection. This change reduces the frequency of unphysical, local extremes of precipitation that were occasionally noted in earlier configurations. Associated with

https://doi.org/10.5194/egusphere-2026-2425
Preprint. Discussion started: 26 May 2026

the reduction in extreme localised precipitation rates, is a reduction in GAL9 in the frequency of very high vertical velocities in the troposphere ($> 1\mathrm{ms}^{-2}$) when compared to GA8GL9 as can be seen in Fig. 4 (the reduction in moderately high vertical velocities in the stratosphere is due the convection changes). The local conservation of water is improved and hence the global conservation in climate simulations as measured by the difference between global mean precipitation and evaporation is also substantially improved. In DA trials there was substantial improvement across a range of measures especially in the summer. Further details of the scheme are given in Lock et al. (2024).

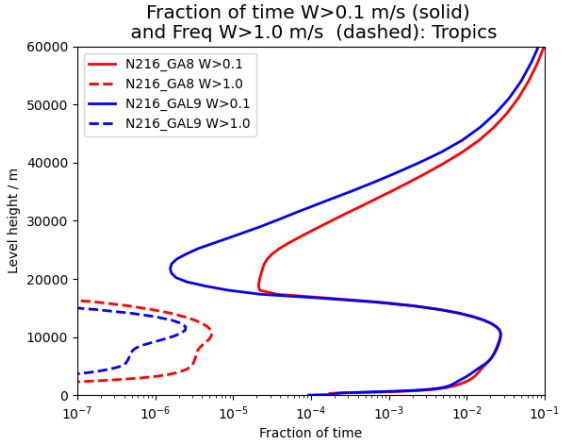

Figure 4. Vertical profile showing the fraction of the time where the vertical velocity exceeds $0.1\,\mathrm{ms}^{-1}$ in solid and $1.0\,\mathrm{ms}^{-1}$ in dashed from 27 year N216 atmosphere/land only climate simulations using GA8GL9 and GAL9 for 20° S to 20° N.

4.11 Corrections

4.11.1 Bug fix to allow non-zero decay of nitrogen through the canopy (GMED ticket #596)

The photosynthetic capacity of each canopy layer varies vertically as leaf nitrogen decreases from the top to the bottom of the canopy as described in Clark et al. (2011). This variation is a function of the nitrogen profile coefficient (k_n in Clark et al., 2011). Prior to GAL9, the value of this coefficient set in the parameter namelist was not correctly passed to JULES and a default value of zero was used instead. This resulted in no decay of leaf nitrogen through the canopy and hence no vertical variation of photosynthetic capacity. This change fixes this bug and the correct value of the nitrogen profile coefficient is passed to JULES.

In climate simulations this correction reduces gross primary productivity (GPP) and on average there is small shift of $\sim 0.4\mathrm{Wm}^{-2}$ from latent heat flux to sensible heat flux over land points.

https://doi.org/10.5194/egusphere-2026-2425
Preprint. Discussion started: 26 May 2026

4.11.2 Moisture conservation fixes for GAL9 (GMED ticket #601)

In preparation for a switch of moist variable in the global atmosphere model from specific humidity to mass mixing ratio, the following set of changes were tested and included in GAL9.

- A reset of negative humidity to zero within the BL scheme that breaks water conservation is removed.
- The convection scheme includes an option to correct the very small errors in water and energy conservation due to the scheme's assumption of hydrostatic balance and shallow atmospheric geometry. This was pragmatically switched off in GA8GL9 (Sect. 3.5.8. in Willett et al., 2026) but is switched back on the GAL9.
- The convection scheme uses specific quantities whereas its water and energy correction is expressed in terms of mixing ratios to be consistent with the dynamics (Sect. 3.1) and global energy correction (Sect. 3.13). This requires the conversion of specific quantities and tendencies to mixing ratios and tendencies to mixing ratios. This change improves these conversions so that they are consistent with the conversions used elsewhere in the model.

This set of changes does improve the conservation of water (as measured by the difference between global mean precipitation and evaporation in long AMIP simulations) and improve the global energy conservation (as measured by the magnitude of the global energy correction as discussed in Sect. 3.13). There are also some small changes to cloud and temperatures but these are addressed as part of the tuning as discussed in Sect. 4.12.

4.11.3 Set temporary fixes to .true. for GAL9 (GMED ticket #568)

In the UM "temporary logicals" are used to protect fixes that significantly alter science configurations. The protection is provided so that a defined GA/GL/GC configuration is scientifically consistent across a limited number of UM releases. From a technical perspective we wish to set as many temporary logicals to true at each GA configuration because this will aid the retirement of the logicals and simplify the code. From a scientific perspective we wish to set them to true because that will fix bugs in the code and enhance the scientific integrity of the model. For GAL9, all available temporary logicals available at the time of the freeze (i.e. those that existed in UM vn12.1) were set to true. The list of fixes applied including a brief description is given in Table 8.

Most of these corrections have a negligible effect on the model evolution or on the model's climate and some have zero effect in some applications. The overall impact is generally small. The stratocumulus regions, however, are brightened by these corrections which results in the global and annual outgoing SW flux increasing by about $0.3\,\mathrm{Wm}^{-2}$. Such changes are not problematic and are accounted for within the tuning process.

4.12 Tuning

GAL9 (and GC5) is intended for use in both NWP and climate applications, and hence it could only be considered to be acceptable if it performs at least as well as its predecessor, GA8GL9, in these applications. Tuning is an essential part of the

https://doi.org/10.5194/egusphere-2026-2425
Preprint. Discussion started: 26 May 2026

Scheme	Variable	Parameter Description
JULES	l_accurate_rho	When set to True improves the accuracy of air density in surface fluxes.
Microphysics	i_fix_mphys_drop_settle	When set to 2 fixes the droplet settling in the microphysics code.
	l_fix_gr_autoc	When set to true fixes a bug in the graupel autoconversion. Has no impact in GAL9 because graupel is not used.
	l_fix_mcr_frac_ice	When set to true fixes inconsistent microphysics increments to ice cloud fraction and mass.
	l_fix_tidy_rainfracs	When set to true, this fixes a bug in the update to rain fractions.
Large-scale cloud	l_pc2_checks_sdfix	When set to true, ensure that total-cloud cover in subsaturated conditions is removed.
UKCA	l_fix_ukca_activate_pdf	When set to true, fixes the pdf of updraught vertical velocities at very high resolutions.
	l_fix_ukca_activate_vert_rep	When set to true, fixes a bug in the CDNC vertical replication in cloud columns.
	l_fix_ukca_cloud_frac	When set to True fixes offset in indexing of cloud fraction array
	l_fix_ukca_h2so4_ystore	When true, correctly store the UKCA H2SO4 tracer in ASAD for updating in GLOMAP-mode and correct the products of the SO2+OH reaction in the StratTrop and Strat mechanisms.
	l_fix_ukca_offox_h2o_fac	When set to True, convert water vapour to vmr in UKCA Offline-Oxidants chemistry.
	l_fix_drydep_so2_water	When set to True, uses correct surface resistance of water when calculating the dry deposition of SO2.

Table 8. Temporary logicals set to true as part of #568

model development process. It is needed to ensure that biases are minimised and that the overall scientific performance reaches an acceptable level across a wide range of measures and experiment types. The tuning described here will cover the tuning necessary after all the changes were combined, but not describe any parameter tuning that was undertaken by developers and included as part of any individual change. As a general principle, the values used for the tuning parameters are either unconstrained by observation or theoretical limits, or where constraints exist are tuned within those constraints.

The wind speeds in GAL9 prior to tuning are consistently higher than those in GA8GL9 (Fig 5). This is primarily because we now account the effects of humidity in the gravity wave drag scheme (Sect. 4.2.1). At some locations and levels this beneficially reduces a pre-existing slow bias, but at other levels (often nearer to the surface) this increases a pre-existing fast bias. For example, the 10 m wind speeds are on average slightly too high in the northern hemisphere and tropics in GA8GL9 and this bias is exacerbated in the untuned GAL9. Furthermore, all else being equal, the increased wind speeds will almost always result in the root mean square vector errors of the winds increasing. The wind speeds are reduced slightly in the final

https://doi.org/10.5194/egusphere-2026-2425
Preprint. Discussion started: 26 May 2026

tuned version of GAL9 but they are still faster than in GA8GL9. This is achieved by increasing the parameters n_sigma and gsharp. n_sigma is the scaling for the subgrid mountain height (which itself is the standard deviation of the difference between the mean orography and high resolution source dataset) and as such affects both the low-level flow blocking and the drag associated with gravity waves. gsharp is a scaling factor within the gravity wave scheme and primarily affects the drag at higher levels.

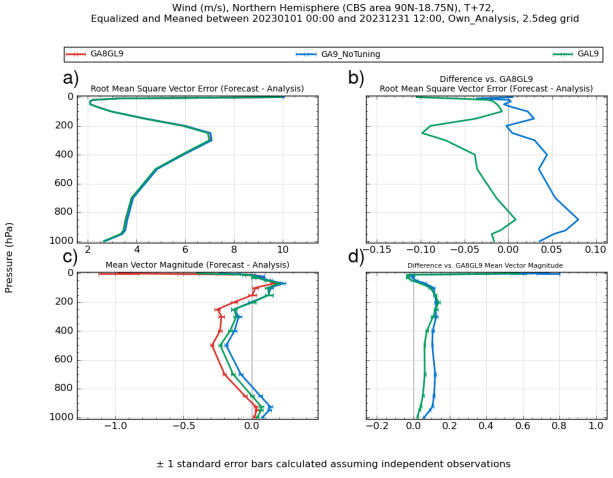

Figure 5. Verification with respect to operational analyses of northern hemisphere T+72 wind forecasts from N320 GA8GL9, GAL9 without tunings and standard GAL9 showing a) RMSE, b) difference in RMSE relative to GA8GL9, c) mean error, and d) difference in mean error relative to GA8GL9 for 59 cases between January and December 2023.

Prior to tuning GAL9, the outgoing SW radiation is much higher than observed estimates (Table 9) which results in the net downward radiation at the TOA being too low. Long coupled simulations with such a radiative balance would tend to get substantially colder. To address this issue, the cloud was tuned in GAL9 to give global mean TOA radiative fluxes in N216 AMIP simulations close to observed values.

As was mentioned in Sect. 2, the net TOA radiation was tuned to within observed estimate during the development process to facilitate testing of long coupled climate integrations. This was primarily done using the two_d_fsd_factor parameter which converts a one-dimensional fractional standard deviation of cloud condensate to a two-dimensional value and, hence, effectively controls the amount of cloud inhomogeneity and the overall radiative impact of the cloud. Its value tends to have a stronger effect on low cloud and therefore a stronger effect on the outgoing SW than on outgoing LW. The final value of two_d_fsd_factor was increased which decreased the cloud homogeneity and thereby increased the net downward radiation TOA by about 1 Wm^{-2}.

thipixs_mid controls the size of the initial parcel buoyancy perturbation for mid-level convection. Larger values of thipixs_mid results in the convection scheme transporting more water from the BL, where convection is often initiated, into the free troposphere (noting that the initial perturbation is usually only applied in terms of humidity and not temperature). Within the tuning process the value of thipixs_mid was increased from 0.2 K to 0.5 K which reduces the amount of BL cloud and

https://doi.org/10.5194/egusphere-2026-2425
Preprint. Discussion started: 26 May 2026

Field	untuned	standard	Observed Estimate
Outgoing LW radiation (Wm^{-2})	239.9	240.6	240.1
Outgoing SW radiation (Wm^{-2})	102.5	98.9	99.1
Net downward radiation at TOA (Wm^{-2})	-2.0	+0.9	+0.7
Precipitation (mmday^{-1})	3.09	3.07	2.81

Table 9. Global- and annual-mean fluxes from 20-year N216 AMIP simulations using GAL9 without the tunings in Table 10 and standard GAL9 with the tunings, and observed estimates. The observed estimates of radiative fluxes are from CERES-EBAF edition 4.0 (Loeb et al., 2018) and the precipitation from GPCP version 3.2 (Huffman et al., 2023).

increases the amount of high cloud. The net effect is an increase of net downward radiation of about 0.8 Wm^{-2}. Furthermore, prior to tuning the free troposphere tends to be cooler than GA8GL9 (Fig. 6). Increasing thipixs_mid acts to warm the troposphere and reduce the cold bias.

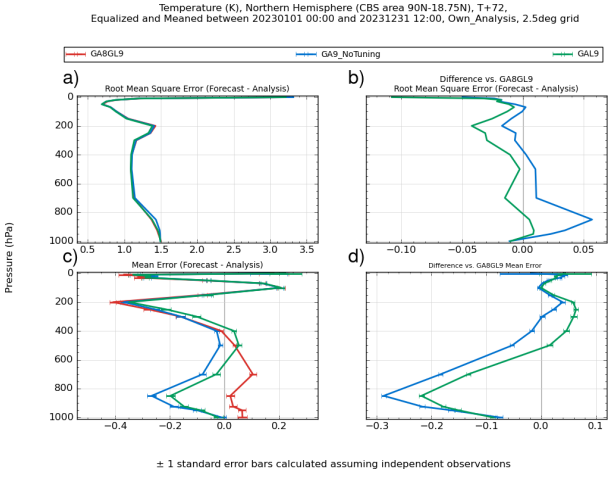

Figure 6. Verification with respect to operational analyses of northern hemisphere T+72 temperature forecasts from N320 GA8GL9, GAL9 without tunings and standard GAL9 showing a) RMSE, b) difference in RMSE relative to GA8GL9, c) mean error, and d) difference in mean error relative to GA8GL9 for 59 cases between January and December 2023.

At the very final stages of development the net downward radiation at TOA was increased by about 0.3 Wm^{-2} by altering the parameters in the Liu cloud droplet spectral dispersion (Liu et al., 2008). This increased the cloud droplet effective radius which improves the agreement with the observation based estimates.

The combined impact of the tuning is strongly beneficial in climate (Fig. 7) and in NWP simulations (Fig. 8). The scientific performance of untuned version of GAL9 would be substantially worse than GA8GL9 and it would not have been considered acceptable for operational climate and NWP use. The tuned parameters and their GA8GL9 and GAL9 values are listed in Table 10.

https://doi.org/10.5194/egusphere-2026-2425
Preprint. Discussion started: 26 May 2026

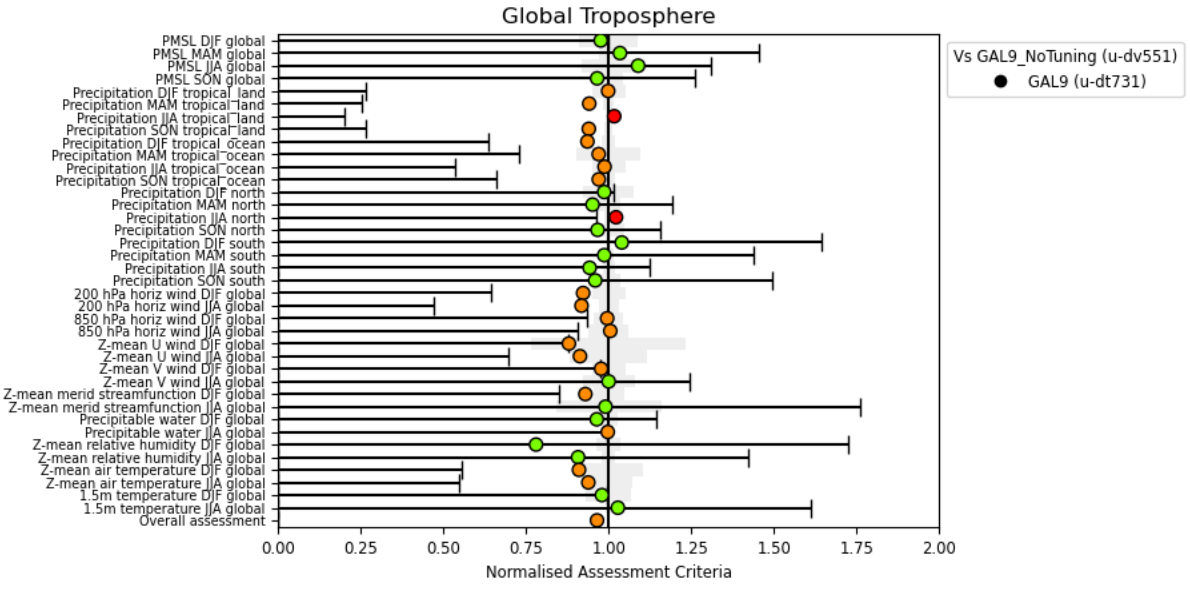

Figure 7. Normalised assessment plot (ratio of mean field RMSEs) for a number of atmospheric fields from a GAL9 atmosphere/land-only climate simulation at N216 horizontal resolution compared to an equivalent simulation using a version of GAL9 without tuning. Statistics shown are for seasons DJF, MAM, JJA and September–November (SON) and for regions global, tropical land (land points between 30° N and 30° S), tropical ocean (sea points between 30° N and 30° S), north (30°– 90° N) and south (30°– 90° S). The observation datasets used are HadSLP2 pressure at mean sea level (Allan and Ansell, 2006), GPCP precipitation (Adler et al., 2003), SSMI precipitable water (Wentz and Spencer, 1998) and CRUTEM3 1.5 m temperature (Brohan et al., 2006), whilst the remaining climatologies are from ERA-interim reanalyses (Berrisford et al., 2009). The whisker bars are observational uncertainty, which is calculated by comparing these with alternative datasets; these are ERA-40 pressure at mean sea level and precipitable water (Uppala et al., 2005), CMAP precipitation (Xie and Arkin, 1997), Legates and Willmott (1990) 1.5 m temperature and MERRA reanalyses for everything else (Bosilovich, 2008). Green circles denote fields for which the RMSE lies within observational uncertainty, whilst light orange or red circles denote fields that do not, and for which the RMSE is improved or degraded respectively.

In GAL9, the resolution sensitivity between N216 and N96 in all the individual TOA radiative components is less than in previous configurations. There is, however, a reduction in the cancellation effects between the individual components that results in a change in the net downward radiation at the TOA between N216 and N96. The default GAL9 settings are optimised for N216 (Table 9), but with the default parameter settings the net downward radiation at TOA in N96 GAL9 for present day climate simulations is higher than is desirable (+2.5 $\mathrm{Wm^{-2}}$). This is not normally an issue in AMIP simulations, but in coupled simulations the ocean would warm excessively. To obtain a realistic net downward radiation at the TOA in N96 GAL9 simulations for present day conditions, it is recommended that the cape_timescale is increased from 1800s to 3600s and two_d_fsd_factor is decreased from 1.65 to 1.56. This gives a net downward radiation at the TOA in N96 GAL9 of +1.0 $\mathrm{Wm^{-2}}$ which is acceptably close to observed estimates.

https://doi.org/10.5194/egusphere-2026-2425
Preprint. Discussion started: 26 May 2026

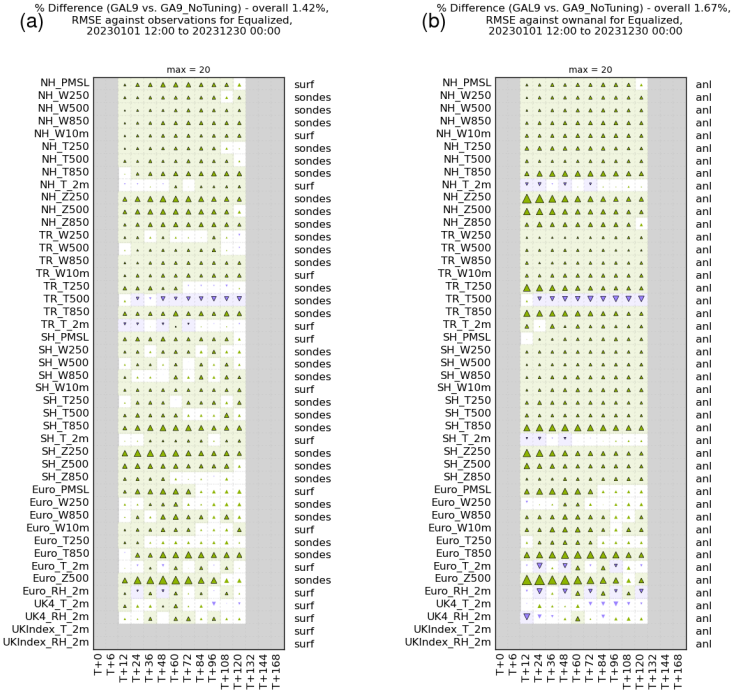

Figure 8. Global evaluation suite scorecards for GAL9 tuned vs GAL9 untuned for 59 cases between January and December 2023 with respect to (a) observations and (b) operational Met Office analyses. Shaded boxes are statistically significant. Green upward pointing triangles indicate the RMSEs in GAL9 tuned are reduced relative to GAL9 untuned, and downward pointing purple triangles indicate where the RMSEs are increased. The area of the triangles are proportion to the change in RMSE with a change of 5 % filling the box.

5 Evaluation

A detailed assessment of GC5 against GC4 is given in Xavier et al. (2026). However, a reduced assessment was made against GA8GL9 and this is presented here.

5.1 Climate Assessment

The climate performance of GAL9 was compared to GA8GL9 using 27 year long atmosphere/land only climate simulations at both N96L85 and N216L85 resolutions. Unsurprisingly given the additional resolution, N216 performs better than N96 in most metrics for both configurations. However, the differences in climate mean fields between the resolutions is usually smaller than the differences between the model configurations, and usually far smaller than the differences between model and observations or reanalyses. We focus here, therefore, on the N216L85 simulations and note that the differences between GA8GL9 and GAL9 at N96L85 will be similar unless explicitly discussed in the text.

https://doi.org/10.5194/egusphere-2026-2425
Preprint. Discussion started: 26 May 2026

Ticket	Scheme	Variable	Parameter Description	GA8GL9 Value	GAL9 Value
#549	Convection	`thpixs_mid`	Initial parcel perturbation for mid-level convection prior to pressure thickness scaling	0.2 K	0.5 K
#583	Orographic drag	`n_sigma`	Scaling factor for the subgrid standard deviation of orography to give heights of sub-grid mountain peaks	2.5	2.6
		`gsharp`	Factor controlling the amount of orographic GW drag	0.5	0.7
#573	Large-scale cloud and radiation	`mp_dz_scal`	Scaling factor for the mixed phase cloud turbulent mixing length (β_1 in Furtado et al. (2016))	1.0	2.0
		`two_d_fsd_factor`	Factor to convert a one dimensional fractional standard deviation to a 2 dimensional value.	1.5	1.65
		`aparam`	Scaling factor that controls the effective radius ratio (a_β in Liu et al. (2008))	0.07	0.077
		`bparam`	Exponential factor that controls the effective radius ratio (b_β in Liu et al. (2008))	-0.14	-0.1365

Table 10. Initial proposed and final values of parameters to tuned to improve cloud, radiation and circulation

Global and annual mean fluxes from the N216L85 model simulations as well as observational estimates are given in Table 11. Both configurations have been tuned to give acceptable values of global and annual mean Top of Atmosphere (TOA) radiative fluxes, and, unsurprisingly, GA8GL9 and GAL9 are both close to observed values.

Field	GA8GL9	GAL9	Observed Estimate
Outgoing LW radiation ($\mathrm{Wm^{-2}}$)	240.3	240.5	240.1
Outgoing SW radiation ($\mathrm{Wm^{-2}}$)	100.0	99.1	99.1
Net downward radiation at TOA ($\mathrm{Wm^{-2}}$)	+0.1	+0.8	+0.7
Precipitation ($\mathrm{mm\,day^{-1}}$)	3.05	3.07	2.81

Table 11. Global- and annual-mean fluxes from 27 year N216 GA8GL9 and GAL9 AMIP simulations and observed estimates. The observed estimates of radiative fluxes are from CERES-EBAF edition 4.0 (Loeb et al., 2018) and the precipitation from GPCP version 3.2 (Huffman et al., 2023)

Figure 9 shows a top-level summary of the impact of GAL9 relative to GA8GL9 on the model's climatology as measured by the ratio of spatial RMSE of various meaned fields with respect to a range of observational estimates and reanalyses. The majority of the fields presented here are either improved, little changed or within observational uncertainty. Many of the wind

https://doi.org/10.5194/egusphere-2026-2425
Preprint. Discussion started: 26 May 2026

fields shown in Fig. 9, and others that are not shown, are improved. The only field that is consistently degraded, albeit by a small amount, is the precipitation over tropical land; in contrast, the precipitation over tropical oceans is improved.

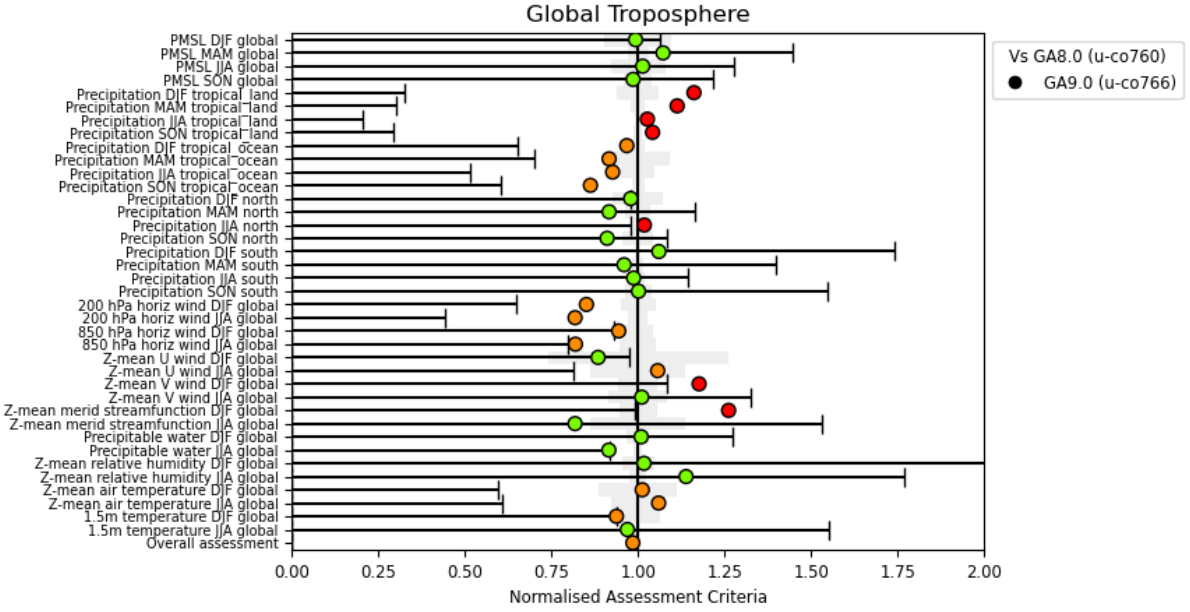

Figure 9. Normalised assessment plot (ratio of mean field RMSEs) for a number of atmospheric fields from a GAL9 atmosphere/land-only climate simulation at N216 horizontal resolution compared to an equivalent simulation using GA8GL9. Statistics shown are for seasons DJF, MAM, JJA and September–November (SON) and for regions global, tropical land (land points between 30° N and 30° S), tropical ocean (sea points between 30° N and 30° S), north (30°– 90° N) and south (30°– 90° S). The observation datasets used are HadSLP2 pressure at mean sea level (Allan and Ansell, 2006), GPCP precipitation (Adler et al., 2003), SSMI precipitable water (Wentz and Spencer, 1998) and CRUTEM3 1.5 m temperature (Brohan et al., 2006), whilst the remaining climatologies are from ERA-interim reanalyses (Berrisford et al., 2009). The whisker bars are observational uncertainty, which is calculated by comparing these with alternative datasets; these are ERA-40 pressure at mean sea level and precipitable water (Uppala et al., 2005), CMAP precipitation (Xie and Arkin, 1997), Legates and Willmott (1990) 1.5 m temperature and MERRA reanalyses for everything else (Bosilovich, 2008). Green circles denote fields for which the RMSE lies within observational uncertainty, whilst light orange or red circles denote fields that do not, and for which the RMSE is improved or degraded respectively.

Figure 10 compares the annual mean precipitation from GAL9 and GA8GL9 with GPCP. The largest change in the pre-
1125 cipitation in GAL9 is the large increase over the maritime continent, which removes a dry bias that the previous GA/GL configurations have had in this region. Perhaps dynamically associated with this, is a reduced wet bias in the tropical Pacific ocean stretching from the Philippines to the date line. The wet-dry dipole bias in the tropical Atlantic is reduced. There is an increase in precipitation over many tropical land areas. This reduces dry biases over India, the Sahel and north-eastern Brazil, but increases a pre-existing wet bias in central Africa. In the extra-tropics the differences in precipitation are more modest and
1130 less systematic.

https://doi.org/10.5194/egusphere-2026-2425
Preprint. Discussion started: 26 May 2026

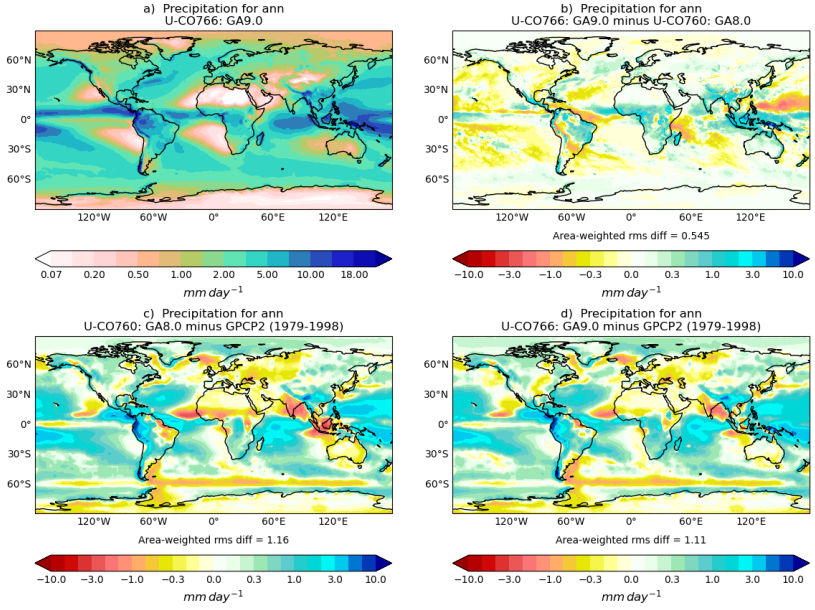

Figure 10. Annual mean precipitation (mmday^{-1}) in the 27 year N216 atmosphere/land only climate simulations compared to GPCP showing (a) GAL9, (b) the difference between GAL9 and GA8GL9, (c) bias in GA8GL9 relative to GPCP and (d) bias in GAL9 relative to GPCP.

The annual mean (shown in Fig. 11) and individual seasons (not shown) outgoing LW radiation (OLR) errors are slightly reduced in GAL9 relative GA8GL9 when compared to CERES-EBAF. The OLR increases in the western tropical Atlantic and south Pacific convergence zone, and decreases in the maritime continent, Arabian sea, India, Sahel and north-eastern Brazil are all beneficial. The increases in the ITCZ in the Pacific and tropical Indian ocean are mostly detrimental.

The annual mean outgoing SW errors are broadly neutral in GAL9 relative to GA8GL9 when compared to CERES-EBAF (Fig. 12) but there some sizeable regional changes. In subtropical stratocumulus and shallow convective regions, there is an increase in outgoing SW which is beneficial in the region to the east of South America where there is a pre-existing low bias, but detrimental in the regions off west Africa and west Australia. The outgoing SW beneficially decreases in the western tropical Atlantic and south Pacific convergence zone, and beneficially increases in the maritime continent. There is also a detrimental reduction in outgoing SW along the ITCZ in the Pacific ocean. Across the Southern Ocean at around 60°S there is beneficial reduction in outgoing SW.

One of the notable circulation improvements is a northward shift in the African Easterly Jet (AEJ) which improves agreement with reanalyses (e.g. Fig. 13). Associated with this is an increase in the strength and number of African Easterly Waves (AEWs), which now provide very good agreement with ERA-Interim at N216, and an increase in rainfall across the Sahel and the wider region (Fig. 14). The increase rainfall results in increases in latent heat flux and screen level humidity, and reductions in sensible heat flux and screen level temperature.

https://doi.org/10.5194/egusphere-2026-2425
Preprint. Discussion started: 26 May 2026

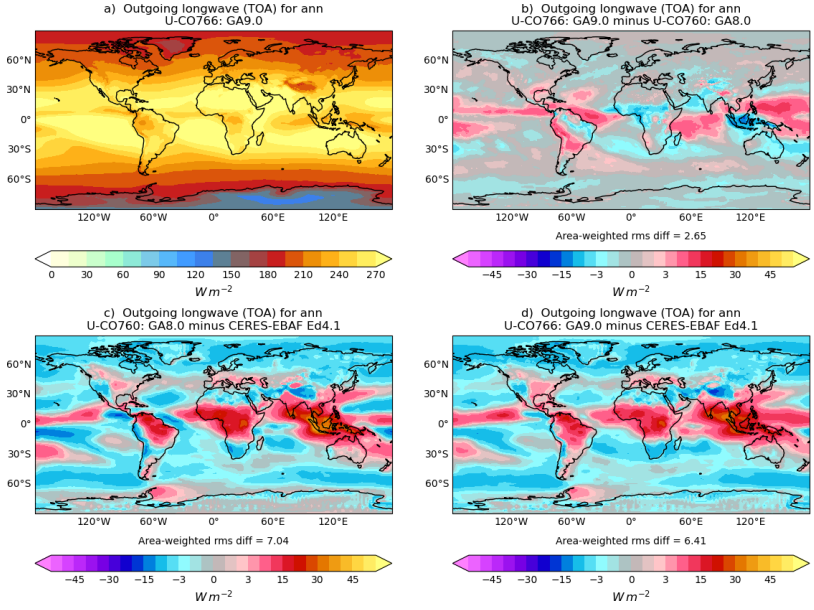

Figure 11. Annual mean top-of-atmosphere outgoing LW radiation (Wm^2) in the 27 year N216 atmosphere/land only climate simulations compared to Clouds and Earth's Radiant Energy System (CERES) Energy Balanced and Filled (EBAF) dataset version 4.1 (NASA/LARC/SD/ASDC, 2019). Layout is the same as in Fig. 10.

As discussed in Sect. 4.8.3, the diurnal cycle is improved with phase errors in the diurnal harmonic typically reduced by 1.5 hrs over tropical land. Other modes of variability that were assessed in these climate simulations, such as the MJO and QBO, were largely unchanged.

5.2 NWP Assessment

The NWP performance of GAL9 was compared to GA8GL9 using 3-month long atmosphere/land only Data Assimilation (DA) trials at a resolution of N320L70 for both summer 2019 and winter 2018/19. The same DA setup was used for both model configurations. The DA setup uses 4-dimensional variational (4DVar) DA (Rawlins et al., 2007) and a variational bias correction (Cameron and Bell, 2018) for the majority of the observations. Each model configuration will have its own analyses, which they will be initialised from and verified against, because of the coupling to the DA system. Top-level summaries of the impact of GAL9 relative to GAL8GL9 for the summer and winter trials and shown in Fig. 15 and Fig. 16 respectively. The fractional change in RMSE when verified against observations, own analyses and operational ECMWF analyses are shown. For the summer period when averaged over all the fields and forecast times shown, the RMSE is reduced by 0.7 %, 1.0 % and 1.3 % against observations, own analyses and ECMWF analyses respectively. Much of this benefit in summer comes from a combination of the improvements to the convection scheme (Sect. 4.8) and fountain buster (Sect. 4.10.1).

In the winter trial the results are more mixed in terms of changes in RMSEs. However, it is worth noting that the winds are typically faster in GAL9 than those in GA8GL9, and this acceleration is largest in the northern hemisphere in winter (e.g.

https://doi.org/10.5194/egusphere-2026-2425
Preprint. Discussion started: 26 May 2026

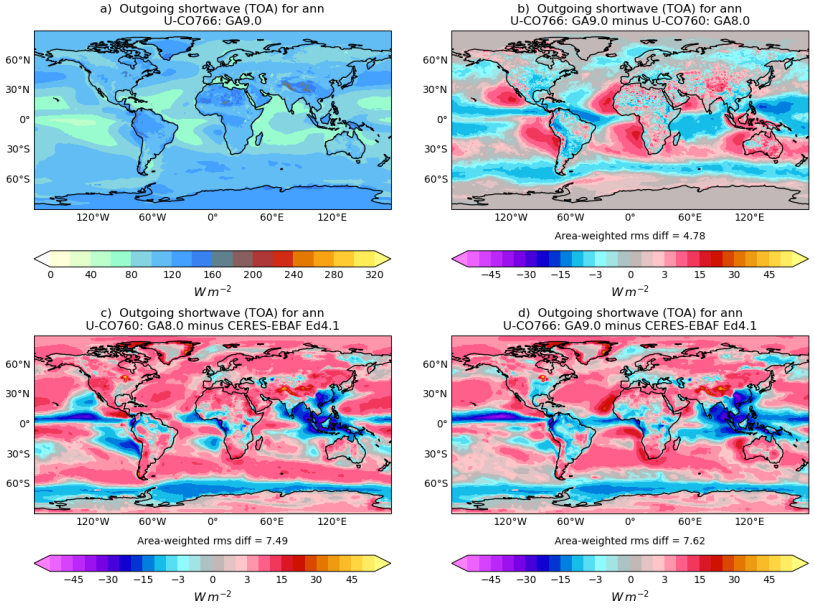

Figure 12. Annual mean top-of-atmosphere outgoing SW radiation (Wm^{-2}) in the 27 year N216 atmosphere/land only climate simulations compared to Clouds and Earth's Radiant Energy System (CERES) Energy Balanced and Filled (EBAF) dataset version 4.1 (NASA/LARC/SD/ASDC, 2019). Layout is the same as in Fig. 10.

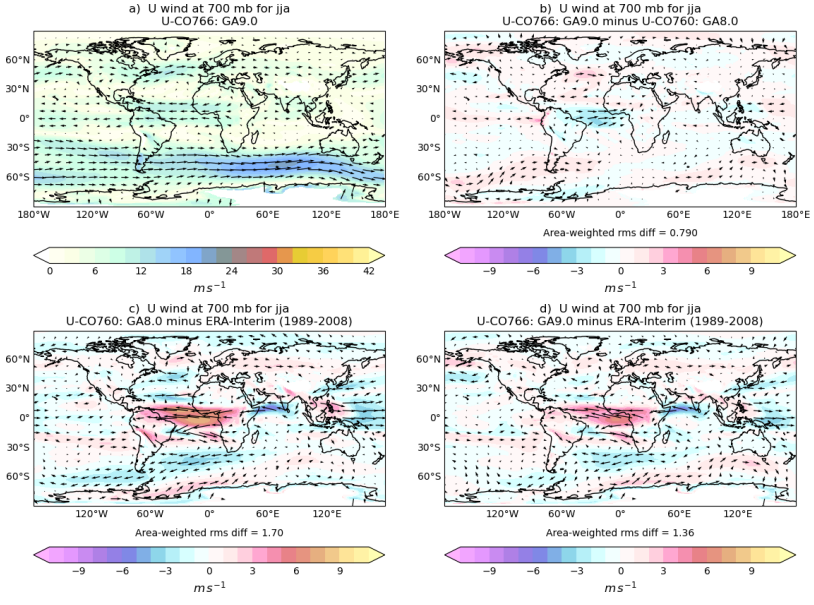

Figure 13. JJA mean 700 hPa winds in the 27 year N216 atmosphere/land only climate simulations compared to ERA-Interim. Layout is the same as in Fig. 10.

https://doi.org/10.5194/egusphere-2026-2425
Preprint. Discussion started: 26 May 2026

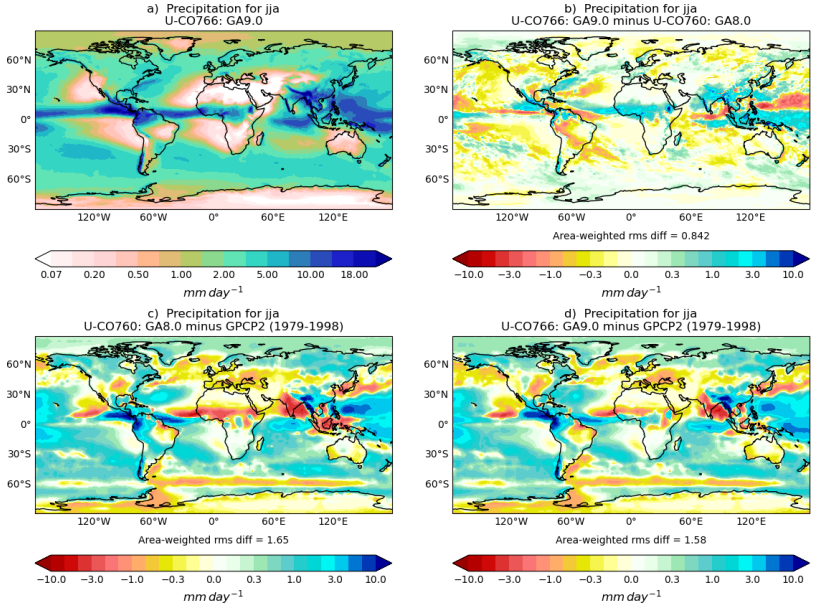

Figure 14. JJA mean precipitation (mmday^{-1}) in the 27 year N216 atmosphere/land only climate simulations compared to GPCP. Layout is the same as in Fig. 10.

Fig. 17). The increased wind speeds reduce a small pre-existing slow bias and we do not see the increased RMSEs usually seen with this. The northern hemisphere temperatures at 850 hPa stand out as consistently worse against all truth types and at most forecast ranges. The primary reason for this is the introduction of a small cold bias (up to $\sim 0.25\mathrm{K}$) at this level as can be seen in Fig. 6.

6 Additional developments included in GAL9.1

The NWP assessment of GAL9 was positive relative to GA8GL9 at N320, but in N1280 winter trials it showed some degradation. A detailed investigation revealed that that cause of the degradation was an incorrect implementation of Targeted Smoothing of Orography (Sect. 4.2.2) which resulted in the orography being excessively smoothed. This error had not been identified earlier in the development of GAL9 because the targeted smoothing does very little at resolutions below N640 and the model development mostly used resolutions lower than this. The additional changes included in GAL9.1 are the fix to the targeted smoothing of orography and an increase in scaling factor for the subgrid mountain height, n_sigma, from 2.6 to 2.8. The forecast performance of GAL9.1 is improved relative to GAL9 at higher resolutions with most of the improvement being seen in the northern hemisphere in winter. The winds are slowed relative to GAL9 but are still faster than GA8GL9. Furthermore, the northern hemisphere 850 hPa winter cold bias is substantially reduced.

The forecast performance of GAL9.1's coupled configuration, GC5.1, is similar to that of GC4 (coupled version of GA8GL9) in winter and slightly better than GC4 in summer. Consequently, GC5.1 was considered to deliver an acceptable level of fore-

https://doi.org/10.5194/egusphere-2026-2425
Preprint. Discussion started: 26 May 2026

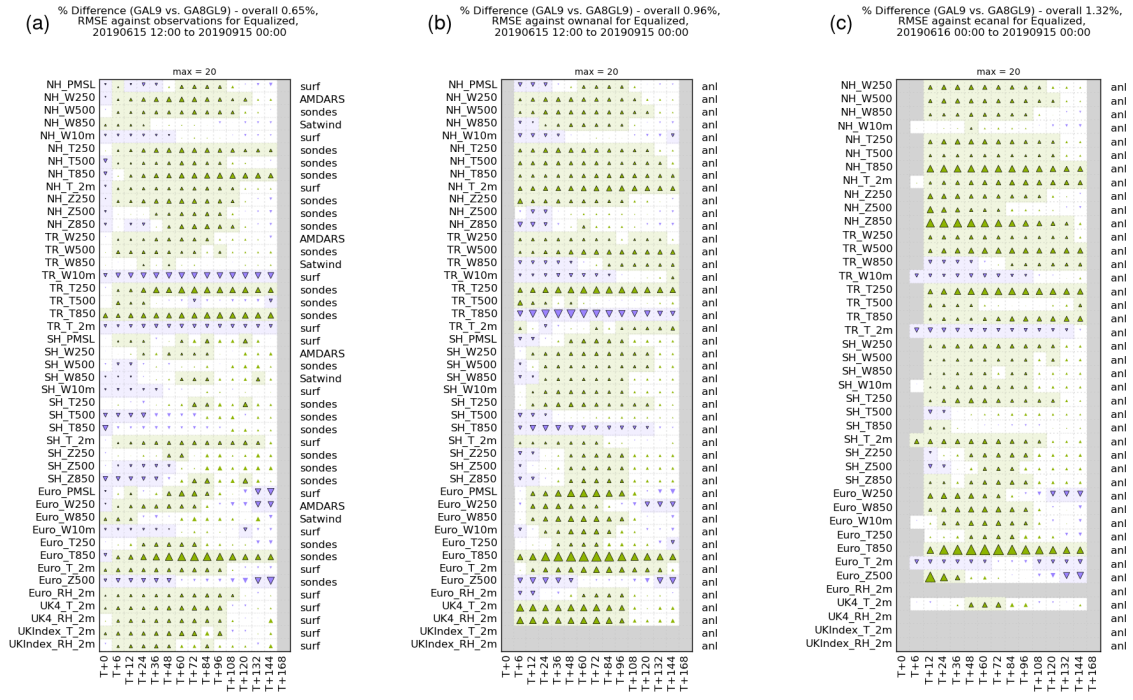

Figure 15. Global evaluation suite scorecards for GAL9 vs GA8GL9 for a three month N320 DA trial from 15 June to 15 September 2019 with respect to (a) observations, (b) own analysis and (c) EC analyses. Shaded boxes are statistically significant. Green upward pointing triangles indicate the RMSEs in GAL9 are reduced relative to GA8GL9, and downward pointing purple triangles indicate where the RMSEs are increased. The area of the triangles are proportion to the change in RMSE with a change of 5 % filling the box.

cast performance for operational implementation at the Met Office for global NWP. Furthermore, the N640 GC5.1 ensemble forecasts no longer had any instability related to orography. It was therefore possible to increase the ensemble forecast time-step from 5 minutes to 7.5 minutes, which matches the deterministic value for that resolution, amounting to a significant saving in runtime resource costs for the global NWP ensemble.

7 Conclusions

GAL9 is the latest seamless global and land science configuration of the Met Office Unified Model and JULES land surface model and it was released in 2023. GAL9 builds upon the previous configuration, GA8GL9, and there are changes to most areas of the science. The targeted smoothing of orography greatly improves the computational stability of the model without degrading scientific performance. The physical realism of the GWD scheme is improved by accounting for the effects of humidity and latent heating, and the source of non-orographic gravity waves is now linked to the local precipitation rather than a single constant value, and hence is far more spatially and temporally variable. A package of convection changes has been added which includes moving to a single "mid-level" scheme to represent both surface driven deep convection and elevated mid-level

https://doi.org/10.5194/egusphere-2026-2425
Preprint. Discussion started: 26 May 2026

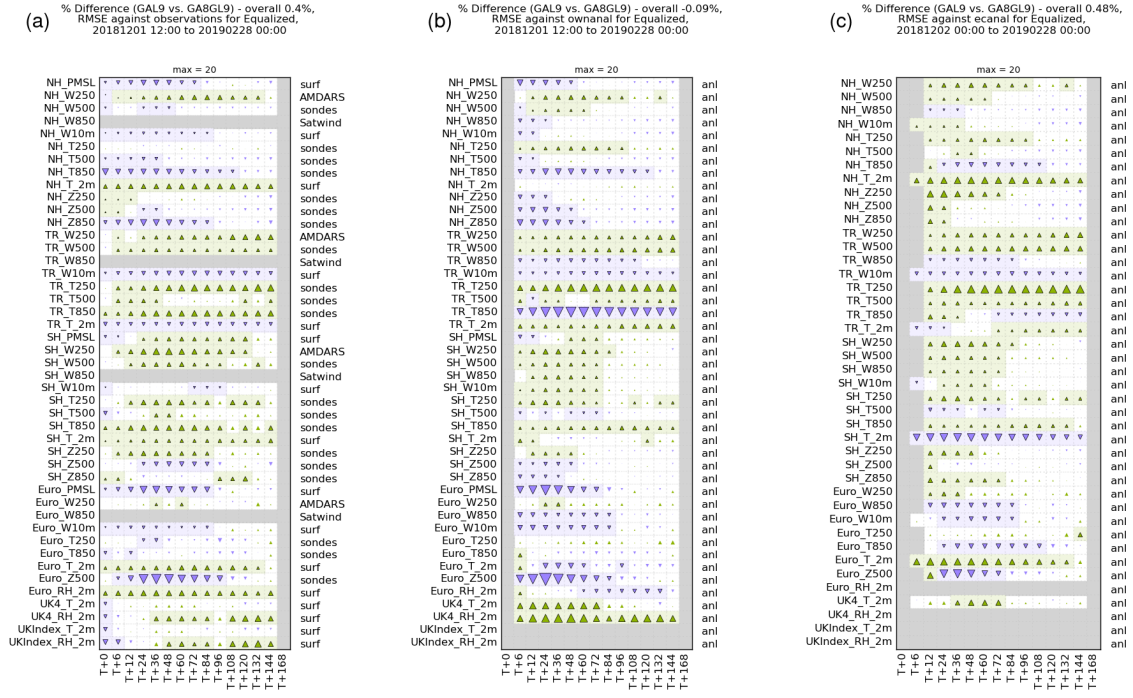

Figure 16. As for Fig. 15 but for a three month N320 DA trial from December 2018 to February 2019.

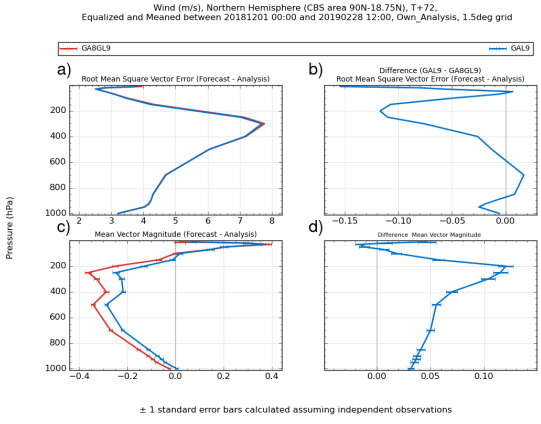

Figure 17. Verification with respect to own analyses of northern hemisphere T+72 wind forecasts from N320 GA8GL9 and GAL9 showing a) RMSE, b) difference in RMSE relative to GA8GL9, c) mean error, and d) difference in mean error relative to GA8GL9 for the winter DA trial.

convection. The greater consistency results in substantial improvements to the diurnal cycle of convection. NWP applications now use GLOMAP climatologies which removes a previous inconsistency between NWP and climate applications. A package

https://doi.org/10.5194/egusphere-2026-2425
Preprint. Discussion started: 26 May 2026

of changes to the land surface has been added including the adoption of the Brookes and Corey soil hydraulics, which removes unrealistic soil moisture profile, and improvements to the representation of surface albedo, which removes the need to apply an observation based albedo scaling. The "Fountain Buster" correction to the semi-Lagrangian advection improves the local conservation of conserved variables and the global water conservation.

The NWP performance of GAL9 at N320 improves upon that of GA8GL9 especially in the summer months. The branch configuration, GAL9.1, fixes an error in targeted smoothing of orography and thereby improves the NWP performance at higher resolutions. GAL9 also improves upon GA8GL9 in terms of its climate performance with noticeable improvements in the large-scale circulation.

In summary, GAL9 and the branch configuration GAL9.1 improve upon the previous configuration GA8GL9 in terms of scientific realism, scientific performance and numerical stability. GAL9 (GAL9.1) is the atmosphere and land component of GC5 (GC5.1). GC5 will form the basis of some of the UK's CMIP7 submissions, and GC5.1 has been the operational global NWP model at the Met Office since January 2026.

Code and data availability. The data and code used in the generation of the figures and tables has, where practical, been archived to zenodo in https://doi.org/10.5281/zenodo.19484323 (Willett, 2026a) and https://doi.org/10.5281/zenodo.19666610 (Willett, 2026b) respectively. Due to intellectual property copyright restrictions, we cannot provide the source code for the UM or JULES, but a copy was made available to the reviewers of this work. The UM is available for use under licence. A number of research organisations and national meteorological services use the UM in collaboration with the Met Office to undertake atmospheric process research, produce forecasts, develop the UM code and build and evaluate Earth system models. To apply for a licence for the UM, go to https://www.metoffice.gov.uk/research/approach/modelling-systems/unified-model (last access: 13 April 2026), and for permission to use JULES, go to https://jules.jchmr.org (last access: 13 April 2026)

Author contributions. MRW led the development of GAL9, collated and edited this paper, was the main developer of tickets #507, #508, #557, #568, #549, #573 and made a significant contributions to #615. MEB made significant contributions to the development and assessment of GAL9. AB made significant contributions to the development and assessment of GAL9, was the main developer for #298, and made significant contributions to #601. CM was the science programme manager for GAL9. PE made significant contributions to the development and assessment of GAL9, and was responsible for the technical development and maintenance of the model and ancillary workflows used in the development and assessment process. SS made significant contributions to the development and assessment of GAL9, was the main developer for #319, #451 and #583, and made significant contributions to #599. LT made significant contributions to the development and assessment of GAL9, and made significant contributions to #557. NLA was the main developer for #551. MB was the main developer for #604 and #527. JME made sigificant contributions to #527. KF made significant contributions to #481. CH made significant contributions to #500 and #503. AH was the main developer for #498. BJ was the main developer for #515. AL was the main developer for #433, #513, #559 and #596, and made significant contributions to #492 and #601. JPM made significant contributions to #500 and #503. JM was the main developer for #518. AS was the main developer for #584. PS made significant contributions to #599. WT made significant contributions to the development and assessment of GAL9 and GAL9.1, and made significant contributions to #599. KVW was the main developer for #493.VV was the main developer for #481. MW made significant contributions to #492 and #615.

https://doi.org/10.5194/egusphere-2026-2425
Preprint. Discussion started: 26 May 2026

Competing interests. The authors declare that they have no conflict of interest

Acknowledgements. The authors would like to thank Anthony Jones for reviewing some sections of this paper. The development and assessment of the Global Atmosphere/Global Land configurations are possible only through the hard work of a large number of people, both within and outside the Met Office, that exceeds the list of authors.

Martin Willett, Melissa Brooks, Andrew, Bushell, Paul Earnshaw, Samantha Smith and Lorenzo Tomassini, Ben Johnson and Jane Mulcahy were supported by the Met Office Hadley Centre Climate Programme funded by the Department of Science, Innovation and Technology (DSIT).

https://doi.org/10.5194/egusphere-2026-2425
Preprint. Discussion started: 26 May 2026

References

Abdul-Razzak, H. and Ghan, S. J.: A parameterization of aerosol activation: 2. Multiple aerosol types, J. Geophys. Res., 105, 6837–6844, https://doi.org/10.1029/1999JD901161, 2000.

Abel, S. J. and Boutle, I. A.: An improved representation of the raindrop size distribution for single-moment microphysics schemes, Q. J. R. Meteorol. Soc., 138, 2151–2162, https://doi.org/10.1002/qj.1949, 2012.

Abel, S. J. and Shipway, B. J.: A comparison of cloud-resolving model simulations of trade wind cumulus with aircraft observations taken during RICO, Q. J. R. Meteorol. Soc., 133, 781–794, https://doi.org/10.1002/qj.55, 2007.

Adler, R. F., Huffman, G. J., Chang, A., Ferraro, R., Xie, P.-P., Janowiak, J., Rudolf, B., Schneider, U., Curtis, S., Bolvin, D., Gruber, A., Susskind, J., Arkin, P., and Nelkin, E.: The version-2 Global Precipitation Climatology Project (GPCP) monthly precipitation analysis (1979-present), J. Hydrometeor., 4, 1147–1167, https://doi.org/10.1175/1525-7541(2003)004<1147:TVGPCP>2.0.CO;2, 2003.

Allan, R. and Ansell, T.: A new globally complete monthly historical gridded mean sea level pressure dataset (HadSLP2): 1850–2004, J. Climate, 19, 5816–5842, https://doi.org/10.1175/JCLI3937.1, 2006.

Amundsen, D. S., Tremblin, P., Manners, J., Baraffe, I., and Mayne, N. J.: Treatment of overlapping gaseous absorption with the correlated-k method in hot Jupiter and brown dwarf atmosphere models, Astron. Astrophys., 598, A97, https://doi.org/10.1051/0004-6361/201629322, 2017.

Arakawa, A. and Lamb, V. R.: Computational design of the basic dynamic processes of the UCLA general circulation model, Methods Comput. Phys., 17, 173–265, 1977.

Archibald, A. T., O'Connor, F. M., Abraham, N. L., Archer-Nicholls, S., Chipperfield, M. P., Dalvi, M., Folberth, G. A., Dennison, F., Dhomse, S. S., Griffiths, P. T., Hardacre, C., Hewitt, A. J., Hill, R. S., Johnson, C. E., Keeble, J., Köhler, M. O., Morgenstern, O., Mulcahy, J. P., Ordóñez, C., Pope, R. J., Rumbold, S. T., Russo, M. R., Savage, N. H., Sellar, A., Stringer, M., Turnock, S. T., Wild, O., , and Zeng, G.: Description and evaluation of the UKCA stratosphere–troposphere chemistry scheme (StratTrop vn 1.0) implemented in UKESM1, Geosci. Model Dev., 13, 1223–1266, https://doi.org/10.5194/gmd-13-1223-2020, 2020.

Asner, G. P., Wessman, C. A., Schimel, D. S., and Archer, S.: Variability in Leaf and Litter Optical Properties: Implications for BRDF Model Inversions Using AVHRR, MODIS, and MISR, Rem. Sens. Environ., 63, 243–257, https://doi.org/10.1016/S0034-4257(97)00138-7, 1998.

Baran, A. J., Hill, P., Walters, D., Hardman, S. C., Furtado, K., Field, P. R., and Manners, J.: The impact of two coupled cirrus microphysics-radiation parameterizations on the temperature and specific humidity biases in the tropical tropopause layer in a climate model, J. Climate, 29, 5299–5316, https://doi.org/10.1175/JCLI-D-15-0821.1, 2016.

Batjes, N. H.: Harmonized soil profile data for applications at global and continental scales: updates to the WISE database, Soil Use Manage., 25, 124–127, https://doi.org/10.1111/j.1475-2743.2009.00202.x, 2009.

Beljaars, A. C. M. and Holtslag, A. A. M.: Flux parametrization over land surfaces for atmospheric models, J. Appl. Meteorol., 30, 327–341, https://doi.org/10.1175/1520-0450(1991)030<0327:FPOLSF>2.0.CO;2, 1991.

Bellouin, N., Rae, J., Jones, A., Johnson, C., Haywood, J., , and Boucher, O.: Aerosol forcing in the Climate Model Intercomparison Project (CMIP5) simulations by HadGEM2-ES and the role of ammonium nitrate, J. Geophys. Res., 116, D20 206, https://doi.org/10.1029/2011JD016074, 2011.

https://doi.org/10.5194/egusphere-2026-2425
Preprint. Discussion started: 26 May 2026

Bellouin, N., Mann, G. W., Woodhouse, M. T., Johnson, C., Carslaw, K. S., and Dalvi, M.: Impact of the modal aerosol scheme GLOMAP-mode on aerosol forcing in the Hadley Centre Global Environmental Model, Atmos. Chem. Phys., 13, 3027–3044, https://doi.org/10.5194/acp-13-3027-2013, 2013.

Bergeron, T.: On the low-level redistribution of atmospheric water caused by orography, in: Supplementary Proceedings of the International Conference on Cloud Physics, 1965.

Berner, J., Jung, T., and Palmer, T. N.: Systematic error model error: the impact of increased horizontal resolution versus improved stochastic and deterministic parameterizations, J. Climate, 66, 603–626, https://doi.org/10.1175/JCLI-D-11-00297.1, 2012.

Berrisford, P., Dee, D., Fielding, K., Fuentes, M., Kållberg, P., Kobayashi, S., and Uppala, S.: The ERA-Interim archive, Tech. Rep. 1, ERA report series, ECMWF, Reading, UK, 2009.

Best, M. J.: Representing urban areas within operational numerical weather prediction models, Bound.-Lay. Meteorol., 114, 91–109, https://doi.org/10.1007/s10546-004-4834-5, 2005.

Best, M. J., Pryor, M., Clark, D. B., Rooney, G. G., Essery, R. L. H., Ménard, C. B., Edwards, J. M., Hendry, M. A., Gedney, N., Mercado, L. M., Sitch, S., Blyth, E., Boucher, O., Cox, P. M., Grimmond, C. S. B., and Harding, R. J.: The Joint UK Land Environment Simulator (JULES), model description — Part 1: Energy and water fluxes, Geosci. Model Dev., 4, 677–699, https://doi.org/10.5194/gmd-4-677-2011, 2011.

Beven, K. J. and Kirkby, M. J.: A physically based, variable contributing area model of basin hydrology, Hydrological Science Bulletin, 24, 43–69, https://doi.org/10.1080/02626667909491834, 1979.

Birk, M., Wagner, G., Loos, J., and Shine, K.: 3 μm Water vapor self- and foreign-continuum: New method for determination and new insights into the self-continuum, Journal of Quantitative Spectroscopy and Radiative Transfer, 253, 107 134, https://doi.org/https://doi.org/10.1016/j.jqsrt.2020.107134, 2020.

Bond, T. C. and Bergstrom, R. W.: Light Absorption by Carbonaceous Particles: An Investigative Review, Aerosol Science and Technology, 40, 27–67, https://doi.org/10.1080/02786820500421521, 2006.

Bond, T. C., Doherty, S. J., Fahey, D. W., Forster, P. M., Berntsen, T., DeAngelo, B. J., Flanner, M. G., Ghan, S., Kärcher, B., Koch, D., Kinne, S., Kondo, Y., Quinn, P. K., Sarofim, M. C., Schultz, M. G., Schulz, M., Venkataraman, C., Zhang, H., Zhang, S., Bellouin, N., Guttikunda, S. K., Hopke, P. K., Jacobson, M. Z., Kaiser, J. W., Klimont, Z., Lohmann, U., Schwarz, J. P., Shindell, D., Storelvmo, T., Warren, S. G., and Zender, C. S.: Bounding the role of black carbon in the climate system: A scientific assessment, Journal of Geophysical Research: Atmospheres, 118, 5380–5552, https://doi.org/https://doi.org/10.1002/jgrd.50171, 2013.

Bosilovich, M. G.: NASA′s modern era retrospective-analysis for research and applications: Integrating Earth observations, Earthzine, https://earthzine.org/nasas-modern-era-retrospective-analysis/, last access: 12$^{\text{th}}$ March 2019, 2008.

Boutle, I. A., Abel, S. J., Hill, P. G., and Morcrette, C. J.: Spatial variability of liquid cloud and rain: observations and microphysical effects, Q. J. R. Meteorol. Soc., 140, 583–594, https://doi.org/10.1002/qj.2140, 2014a.

Boutle, I. A., Eyre, J. E. J., and Lock, A. P.: Seamless stratocumulus simulation across the turbulent gray zone, Mon. Weather Rev., 142, 1655–1668, https://doi.org/10.1175/MWR-D-13-00229.1, 2014b.

Brohan, P., Kennedy, J. J., Harris, I., Tett, S. F. B., and Jones, P. D.: Uncertainty estimates in regional and global observed temperature changes: a new dataset from 1850, J. Geophys. Res., 111, D12 106, https://doi.org/10.1029/2005JD006548, 2006.

Brooks, R. H. and Corey, A. T.: Hydraulic properties of porous media, Hydrological Papers 3, Colorado State Univ., Fort Collins, CO, USA, 1964.

https://doi.org/10.5194/egusphere-2026-2425
Preprint. Discussion started: 26 May 2026

Brown, A. R.: The sensitivity of large-eddy simulations of shallow cumulus convection to resolution and sub-grid model, Q. J. R. Meteorol. Soc., 125, 469–482, https://doi.org/10.1002/qj.49712555405, 1999.

Brown, A. R., Beare, R. J., Edwards, J. M., Lock, A. P., Keogh, S. J., Milton, S. F., and Walters, D. N.: Upgrades to the boundary-layer scheme in the Met Office numerical weather prediction model, Bound.-Lay. Meteorol., 128, 117–132, https://doi.org/10.1007/s10546-008-9275-0, 2008.

Bushell, A. C., Wilson, D. R., and Gregory, D.: A description of cloud production by non-uniformly distributed processes, Q. J. R. Meteorol. Soc., 129, 1435–1455, https://doi.org/10.1256/qj.01.110, 2003.

Bushell, A. C., Butchart, N., Derbyshire, S. H., Jackson, D. R., Shutts, G. J., Vosper, S. B., and Webster, S.: Parameterized gravity wave momentum fluxes from sources related to convection and large-scale precipitation processes in a global atmosphere model, J. Atmos. Sci., 72, 4349–4371, https://doi.org/10.1175/JAS-D-15-0022.1, 2015.

Cameron, J. and Bell, W.: The testing and implementation of variational bias correction (VarBC) in the Met Office global

Charney, J. G. and Phillips, N. A.: Numerical integration of the quasi-geostrophic equations for barotropic and simple baroclinic flows, J. Meteor., 10, 71–99, https://doi.org/10.1175/1520-0469(1953)010<0071:NIOTQG>2.0.CO;2, 1953.

Clark, D. B., Mercado, L. M., Sitch, S., Jones, C. D., Gedney, N., Best, M. J., Pryor, M., Rooney, G. G., Essery, R. L. H., Blyth, E., Boucher, O., Cox, P. M., and Harding, R. J.: The Joint UK Land Environment Simulator (JULES), model description — Part 2: Carbon fluxes and vegetation, Geosci. Model Dev., 4, 701–722, https://doi.org/10.5194/gmd-4-701-2011, 2011.

Cotton, R. J., Field, P. R., Ulanowski, Z., Kaye, P. H., Hirst, E., Greenaway, R. S., Crawford, I., Crosier, J., and Dorsey, J.: The effective density of small ice particles obtained from in situ aircraft observations of mid-latitude cirrus, Q. J. R. Meteorol. Soc., 139, 1923–1934, https://doi.org/10.1002/qj.2058, 2013.

Curcic, M. and Haus, B. K.: Revised Estimate of Ocean Surface Drag in Strong Winds, Geophys. Res. Lett., 47, https://doi.org/10.1029/2020GL087647, 2020.

Cusack, S., Slingo, A., Edwards, J. M., and Wild, M.: The radiative impact of a simple aerosol climatology on the Hadley Centre atmospheric GCM, Q. J. R. Meteorol. Soc., 124, 2517–2526, https://doi.org/10.1002/qj.49712455117, 1998.

Danielson, J. J. and Gesch, D. B.: Global multi-resolution terrain elevation data 2010 (GMTED2010), Tech. Rep. 1073, U.S. Geological Survey, https://doi.org/10.3133/ofr20111073, 2011.

Daumont, D., Brion, J., Charbonnier, J., and Malicet, J.: Ozone UV spectroscopy I: Absorption cross-sections at room temperature, J. Atmos. Chem., 15, 145–155, https://doi.org/10.1007/BF00053756, 1992.

Dawson, A. and Palmer, T. N.: Simulating weather regimes: impact of model resolution and stochastic parameterization, Clim. Dynam., 44, 2177–2193, https://doi.org/10.1007/s00382-014-2238-x, 2015.

Dentener, F., Kinne, S., Bond, T., Boucher, O., Cofala, J., Generoso, S., Ginoux, P., Gong, S., Hoelzemann, J. J., Ito, A., Marelli, L., Penner, J. E., Putaud, J.-P., Textor, C., Schulz, M., van der Werf, G. R., and Wilson, J.: Emissions of primary aerosol and precursor gases in the years 2000 and 1750 prescribed data-sets for AeroCom, Atmos. Chem. Phys., 6, 4321–4344, https://doi.org/10.5194/acp-6-4321-2006, 2006.

Derbyshire, S. H., Maidens, A. V., Milton, S. F., Stratton, R. A., and Willett, M. R.: Adaptive detrainment in a convection parametization, Q. J. R. Meteorol. Soc., 137, 1856–1871, https://doi.org/10.1002/qj.875, 2011.

Dharssi, I., Vidale, P. L., Verhoef, A., Macpherson, B., Jones, C., and Best, M.: New soil physical properties implemented in the Unified Model at PS18, Tech. Rep. 528, Forecasting R&D, Met Office, Exeter, UK, 2009.

https://doi.org/10.5194/egusphere-2026-2425
Preprint. Discussion started: 26 May 2026

Doblas-Reyes, F. J., Weisheimer, A., Déqué, M., Keenlyside, N., McVean, M., Murphy, J. M., Rogel, P., Smith, D., and Palmer, T. N.: Addressing model uncertainty in seasonal and annual dynamical seasonal forecasts, Q. J. R. Meteorol. Soc., 135, 1538–1559, https://doi.org/10.1002/qj.464, 2009.

Donelan, M. A.: On the Decrease of the Oceanic Drag Coefficient in High Winds, Journal of Geophysics Research: Oceans, 123, https://doi.org/10.1002/2017JC013394, 2018.

Donelan, M. A., Haus, B. K., Reul, N., Plant, W. J., Stiassne, M., Graber, H. C., Brown, O. B., and Saltman, E. S.: On the limiting aerodynamic roughness of the ocean in very strong winds, Geophys. Res. Lett., 31, https://doi.org/10.1029/2004GL019460, 2004.

Dorigo, W., Wagner, W., Albergel, C., Albrecht, F., Balsamo, G., Brocca, L., Chung, D., Ertl, M., Forkel, M., Gruber, A., Haas, E., Hamer, D. P., Hirschi, M., Ikonen, J., De Jeu, R., Kidd, R., Lahoz, W., Liu, Y., Miralles, D., and Lecomte, P.: ESA CCI Soil Moisture for improved Earth system understanding: State-of-the art and future directions, Remote Sensing of Environment, 203, 185–215, https://doi.org/10.1016/j.rse.2017.07.001, 2017.

Dorman, J. L. and Sellers, P. J.: A Global Climatology of Albedo, Roughness Length and Stomatal Resistance for Atmospheric General Circulation Models as Represented by the Simple Biosphere Model (SiB), J. Appl. Meteorol., 28, 833–855, https://doi.org/10.1175/1520-0450(1989)028<0833:AGCOAR>2.0.CO;2, 1989.

Dyer, A. J. and Hicks, B. B.: Flux-gradient relationships in the constant flux layer, Q. J. R. Meteorol. Soc., 96, 715–721, https://doi.org/10.1002/qj.49709641012, 1970.

Edson, J. B.: Review of air-sea transfer processes, in: ECMWF workshop on atmosphere-ocean interactions, Reading, UK, 10^{th}-12^{th} November, 2008, pp. 7–24, European Centre for Medium-Range Weather Forecasts, 2009.

Edwards, J. M.: Efficient calculation of infrared fluxes and cooling rates using the two-stream equations, J. Atmos. Sci., 53, 1921–1932, https://doi.org/10.1175/1520-0469(1996)053<1921:ECOIFA>2.0.CO;2, 1996.

Edwards, J. M. and Slingo, A.: Studies with a flexible new radiation code. I: Choosing a configuration for a large-scale model, Q. J. R. Meteorol. Soc., 122, 689–719, https://doi.org/10.1002/qj.49712253107, 1996.

Elsey, J., Coleman, M. D., Gardiner, T. D., Menang, K. P., and Shine, K. P.: Atmospheric observations of the water vapour continuum in the near-infrared windows between 2500 and 6600 cm^{-1}, Atmospheric Measurement Techniques, 13, 2335–2361, https://doi.org/10.5194/amt-13-2335-2020, 2020.

Esentürk, E., Abraham, N. L., Archer-Nicholls, S., Mitsakou, C., Griffiths, P., Archibald, A., , and Pyle, J.: Quasi-Newton methods for atmospheric chemistry simulations: implementation in UKCA UM vn10.8, Geosci. Model Dev., 11, 3089–3108, https://doi.org/10.5194/gmd-11-3089-2018, 2018.

Essery, R., Pomeroy, J., Parviainen, J., and Storck, P.: Sublimation of snow from coniferous forests in a climate model, J. Climate, 16, 1855–1864, https://doi.org/10.1175/1520-0442(2003)016<1855:SOSFCF>2.0.CO;2, 2003a.

Essery, R. L. H., Best, M. J., Betts, R. A., Cox, P. M., and Taylor, C. M.: Explicit representation of subgrid heterogeneity in a GCM land surface scheme, J. Hydrometeor., 4, 530–543, https://doi.org/10.1175/1525-7541(2003)004<0530:EROSHI>2.0.CO;2, 2003b.

Falloon, P. D. and Betts, R. A.: The impact of climate change on global river flow in HadGEM1 simulations, Atmos. Sci. Lett., 7, 62–68, https://doi.org/10.1002/asl.133, 2006.

Field, P. R., Heymsfield, A. J., and Bansemer, A.: Snow Size Distribution Parameterization for Midlatitude and Tropical Ice Clouds, J. Atmos. Sci., 64, 4346–4365, https://doi.org/10.1175/2007JAS2344.1, 2007.

Fletcher, N. H.: The physics of rainclouds, Cambridge University Press, 1962.

https://doi.org/10.5194/egusphere-2026-2425
Preprint. Discussion started: 26 May 2026

Ford, D. A., Edwards, K. P., Lea, D., Barciela, R. M., Martin, M. J., and Demaria, J.: Assimilating GlobColour ocean colour data into a pre-operational physical-biogeochemical model, Ocean Sci., 8, 751–771, https://doi.org/10.5194/os-8-751-2012, 2012.

Fritsch, J. M. and Chappell, C. F.: Numerical prediction of convectively driven mesoscale pressure systems. Part I: convective parameterization, J. Atmos. Sci., 37, 1722–1733, https://doi.org/10.1175/1520-0469(1980)037<1722:NPOCDM>2.0.CO;2, 1980.

Furtado, K., Field, P. R., Boutle, I. A., Morcrette, C. J., and Wilkinson, J. M.: A physically based subgrid parameterization for the production and maintenance of mixed-phase clouds in a general circulation model, J. Atmos. Sci., 73, 279–291, https://doi.org/10.1175/JAS-D-15-0021.1, 2016.

Gedney, N. and Cox, P. M.: The sensitivity of global climate model simulations to the representation of soil moisture heterogeneity, J. Hydrometeor., 4, 1265–1275, https://doi.org/10.1175/1525-7541(2003)004<1265:TSOGCM>2.0.CO;2, 2003.

Godfrey, J. S. and Beljaars, A. C. M.: On the turbulent fluxes of buoyancy, heat and moisture at the air-sea interface at low wind speeds, J. Geophys. Res., 96, 22 043–22 048, https://doi.org/10.1029/91JC02015, 1991.

Gorshelev, V., Serdyuchenko, A., Weber, M., Chehade, W., and Burrows, J. P.: High spectral resolution ozone absorption cross-sections - Part 1: Measurements, data analysis and comparison with previous measurements around 293 K, Atmos. Meas. Tech., 7, 609–624, https://doi.org/10.5194/amt-7-609-2014, 2014.

Grant, A. L. M.: Cloud-base fluxes in the cumulus-capped boundary layer, Q. J. R. Meteorol. Soc., 127, 407–421, https://doi.org/10.1002/qj.49712757209, 2001.

Grant, A. L. M. and Brown, A. R.: A similarity hypothesis for shallow-cumulus transports, Q. J. R. Meteorol. Soc., 125, 1913–1936, https://doi.org/10.1002/qj.49712555802, 1999.

Gregory, D. and Allen, S.: The effect of convective downdraughts upon NWP and climate simulations, in: Ninth conference on numerical weather prediction, Denver, Colorado, pp. 122–123, American Meteorological Society, 1991.

Gregory, D. and Rowntree, P. R.: A massflux convection scheme with representation of cloud ensemble characteristics and stability dependent closure, Mon. Weather Rev., 118, 1483–1506, https://doi.org/10.1175/1520-0493(1990)118<1483:AMFCSW>2.0.CO;2, 1990.

Gregory, D., Kershaw, R., and Inness, P. M.: Parametrization of momentum transport by convection II: Tests in single-column and general circulation models, Q. J. R. Meteorol. Soc., 123, 1153–1183, https://doi.org/10.1002/qj.49712354103, 1997.

Grimmond, C., Blackett, M., Best, M., Baik, J.-J., Belcher, S., Bohnenstengel, S., Calmet, I., Chen, F., Dandou, A., Fortuniak, K., Gouvea, M., Hamdi, R., Hendry, M., Kondo, H., Krayenhoff, S., Lee, S.-H., Loridan, T., Martilli, A., Masson, V., Miao, S., Oleson, K., Pigeon, G., Porson, A., Salamanca, F., Steeneveld, G.-J., Tombrou, M., Voogt, J., and Zhang, N.: Initial results from Phase 2 of the international urban energy balance model comparison, Int. J. Clim., 31, 244–272, https://doi.org/10.1002/joc.2227, 2011.

Gruber, A., Scanlon, T., van der Schalie, R., Wagner, W., and Dorigo, W.: Evolution of the ESA CCI Soil Moisture climate data records and their underlying merging methodology, Earth Syst. Sci. Data, 11, 717–739, https://doi.org/10.5194/essd-11-717-2019, 2019.

Guiavarc'h, C., Storkey, D., Blaker, A. T., Blockley, E., Megann, A., Hewitt, H., Bell, M. J., Calvert, D., Copsey, D., Sinha, B., Moreton, S., Mathiot, P., , and An, B.: GOSI9: UK Global Ocean and Sea Ice configurations, Geosci. Model Dev., 18, 377–403, https://doi.org/https://doi.org/10.5194/gmd-18-377-2025, 2025.

Hapke, B.: Bidirectional reflectance spectroscopy: 1. Theory, J. Geophys. Res., 86(B4), 3039–3054, https://doi.org/10.1029/JB086iB04p03039, 1981.

Hardacre, C., Mulcahy, J. P., Pope, R. J., Jones, C. G., Rumbold, S. T., Li, C., Johnson, C., and Turnock, S. T.: Evaluation of SO_2, SO_4^{2-} and an updated SO_2 dry deposition parameterization in the United Kingdom Earth System Model, Atmospheric Chemistry and Physics, 21, 18 465–18 497, https://doi.org/10.5194/acp-21-18465-2021, 2021.

https://doi.org/10.5194/egusphere-2026-2425
Preprint. Discussion started: 26 May 2026

Hill, P. G., Manners, J., and Petch, J. C.: Reducing noise associated with the Monte Carlo Independent Column Approximation for weather forecasting models, Q. J. R. Meteorol. Soc., 137, 219–228, https://doi.org/10.1002/qj.732, 2011.

Hill, P. G., Morcrette, C. J., and Boutle, I. A.: A regime-dependent parametrization of subgrid-scale cloud water content variability, Q. J. R. Meteorol. Soc., 141, 1975–1986, https://doi.org/10.1002/qj.2506, 2015.

Hoesly, R. M., Smith, S. J., Feng, L., Klimont, Z., Janssens-Maenhout, G., Pitkanen, T., Seibert, J. J., Vu, L., Andres, R. J., Bolt, R. M., Bond, T. C., Dawidowski, L., Kholod, N., Kurokawa, J.-I., Li, M., Liu, L., Lu, Z., Moura, M. C. P., O'Rourke, P. R., and Zhang, Q.: Historical (1750–2014) anthropogenic emissions of reactive gases and aerosols from the Community Emissions Data System (CEDS), Geoscientific Model Development, 11, 369–408, https://doi.org/10.5194/gmd-11-369-2018, 2018.

Hosgood, B., Jacquemound, S., Andreeoli, G., Verdebout, J., Pedrini, J., and Schmuck, G.: Leaf Optical Properties Experiment Database (LOPEX93). Data set., Available on-line from the Ecological Spectral Information System (EcoSIS), http://ecosis.org, last access February 2020, 1993.

Houldcroft, C., Grey, W., Barnsley, M., Taylor, C., Los, S., and North, P.: New vegetation albedo parameters and global fields of background albedo derived from MODIS for use in a climate model, J. Hydrometeorology, 10, 183–198, https://doi.org/10.1175/2008JHM1021.1, 2008.

Huffman, G. J., Bolvin, D. T., Braithwaite, D., Hsu, K., Joyce, R., Kidd, C., Nelkin, E. J., Sorooshian, S., Tan, J., and Xie, P.: NASA Global Precipitation Measurement (GPM) Integrated Multi-satellitE Retrievals for GPM (IMERGE): Algorithm Theoretical Basis Document (ATBD) Version 06, Tech. rep., NASA/GSFC, https://gpm.nasa.gov/sites/default/files/2020-05/IMERG_ATBD_V06.3.pdf, last access: 2 February 2026, 2020a.

Huffman, G. J., Bolvin, D. T., Braithwaite, D., Hsu, K.-L., Joyce, R. J., Kidd, C., Nelkin, E. J., Sorooshian, S., Stocker, E. F., Tan, J., Wolff, D. B., and Xie, P.: Integrated Multi-satellite Retrievals for the Global Precipitation Measurement (GPM) Mission (IMERG), pp. 343–353, Springer International Publishing, Cham, ISBN 978-3-030-24568-9, https://doi.org/10.1007/978-3-030-24568-9_19, 2020b.

Huffman, G. J., Adler, R., Behrangi, A., Bolvin, D. T., Nelkin, E. J., Gu, G., and Ehsani, M. R.: The New Version 3.2 Global Precipitation Climatology Project (GPCP) Monthly and Daily Precipitation Products, J.Clim., 36, 7635–7655, https://doi.org/10.1175/JCLI-D-23-0123.1, 2023.

Jin, Z., Qiao, Y., Wang, Y., Fang, Y., and Yi, W.: A new parameterization of spectral and broadband ocean surface albedo, Opt. Expres, 19, 26 429–26 443, https://doi.org/10.1364/OE.19.026429, 2011.

Johansen, O.: Thermal conductivity of soils, Ph.D. thesis, University of Trondheim, Norway, 1975.

Jones, A., Roberts, D. L., and Slingo, A.: A climate model study of indirect radiative forcing by anthropogenic sulphate aerosols, Nature, 370, 450–453, https://doi.org/10.1038/370450a0, 1994.

Lana, A., Bell, T. G., Simó, R., Vallina, S. M., Ballabrera-Poy, J., Kettle, A. J., Dachs, J., Bopp, L., Saltzman, E. S., Stefels, J., Johnson, J. E., and Liss, P. S.: An updated climatology of surface dimethlysulfide concentrations and emission fluxes in the global ocean, Global Biogeochem. Cycles, 25, GB1004, https://doi.org/10.1029/2010GB003850, 2011.

Lawrence, D. M., Oleson, K. W., Flanner, M. G., Thornton, P. E., Swenson, S. C., Lawrence, P. J., Zeng, X., Yang, Z.-L., Levis, S., Sakaguchi, K., Bonan, G. B., and Slater, A. G.: Parameterization improvements and functional and structural advances in version 4 of the community land model, J. Adv. Model Earth Syst., 3, M03 001, https://doi.org/10.1029/2011MS00045, 2011.

Lean, J., Rottman, G., Harder, J., and Kopp, G.: SORCE Contributions to New Understanding of Global Change and Solar Variability, in: The Solar Radiation and Climate Experiment (SORCE): Mission Description and Early Results, edited by Rottman, G., Woods, T., and George, V., pp. 27–53, Springer New York, New York, NY, https://doi.org/10.1007/0-387-37625-9_3, 2005.

https://doi.org/10.5194/egusphere-2026-2425
Preprint. Discussion started: 26 May 2026

Legates, D. R. and Willmott, C. J.: Mean seasonal and spatial variability in global surface air temperature, Theor. Appl. Climatol., 41, 11–21, https://doi.org/10.1007/BF00866198, 1990.

Lewis, P., Guanter, L., Saldana, G. L., Muller, J., Watson, G., Shane, N., Kennedy, T., Fisher, J., Domenech, C., Preusker, R., North, P., Heckel, A., Danne, O., Krämer, U., Zülke, M., Fomferra, N., Brockmann, C., and Schaaf, C.: The ESA globAlbedo project: Algorithm, in: IEEE International Geoscience and Remote Sensing Symposium (IGARSS) 2012, pp. 5745–5748, Munich, Germany, https://doi.org/10.1109/IGARSS.2012.6352306, 2012.

Lipson, M., Grimmond, S., Best, M., Abramowitz, G., Coutts, A., Tapper, N., Baik, J.-J., Beyers, M., Blunn, L., Boussetta, S., Bou-Zeid, E., De Kauwe, M., De Munck, C., Demuzere, M., Fatichi, S., Fortuniak, K., Han, B.-S., Hendry, M., Kikegawa, Y., Kondo, H., Lee, D.-I., Lee, S.-H., and Lemonsu, A.: Evaluation of 30 urban land surface models in the Urban- PLUMBER project: Phase 1 results, Q. J. R. Meteorol. Soc., 150, 126–169, https://doi.org/10.1002/qj.4589, 2023.

Liu, H., Jezek, K. C., Li, B., and Zhao, Z.: Radarsat Antarctic Mapping Project Digital Elevation Model, Version 2., Tech. rep., NASA National Snow and Ice Data Center Distributed Active Archive Center., https://doi.org/10.5067/8JKNEW6BFRVD, 2015.

Liu, Y., Daum, P. H., Guo, H., and Peng, Y.: Dispersion bias, dispersion effect, and the aerosol-cloud conundrum, Environ. Res. Lett., 3, https://doi.org/10.1088/1748-9326/3/4/045021, 2008.

Lock, A. P.: The numerical representation of entrainment in parametrizations of boundary layer turbulent mixing, Mon. Weather Rev., 129, 1148–1163, https://doi.org/10.1175/1520-0493(2001)129<1148:TNROEI>2.0.CO;2, 2001.

Lock, A. P., Brown, A. R., Bush, M. R., Martin, G. M., and Smith, R. N. B.: A new boundary layer mixing scheme. Part I: Scheme description and single-column model tests, Mon. Wea. Rev., 128, 3187–3199, https://doi.org/10.1175/1520-0493(2000)128<3187:ANBLMS>2.0.CO;2, 2000.

Lock, A. P., Whitall, M., Stirling, A. J., Williams, K. D., Lavender, S. L., Morcrette, C., Matsubayashi, K., Field, P. R., Martin, G., Willett, M. R., and Heming, J.: The performance of the CoMorph-A convection package in global simulations with the Met Office Unified Model, Q. J. R. Meteorol. Soc., 150, 3527–3543, https://doi.org/10.1002/qj.4781, 2024.

Loeb, N. G., Doelling, D. R., Wang, H., Su, W., Nguyen, C., Corbett, J. G., Liang, L., Mitrescu, C., Rose, F. G., and Kato, S.: Clouds and the Earth's Radiant Energy System (CERES) Energy Balanced and Filled (EBAF) Top-of-Atmosphere (TOA) Edition-4.0 Data Product, J.Clim., 31, 895–918, https://doi.org/10.1175/JCLI-D-17-0208.1, 2018.

Lott, F. and Miller, M. J.: A new subgrid-scale orographic drag parametrization: Its formulation and testing, Q. J. R. Meteorol. Soc., 123, 101–127, https://doi.org/10.1002/qj.49712353704, 1997.

Loveland, T. R., Reed, B. C., Brown, J. F., Ohlen, D. O., Zhu, Z., Yang, L., and Merchant, J. W.: Development of a global land cover characteristics database and IGBP DISCover from 1 km AVHRR data, Int. J. Remote Sens., 21, 1303–1330, https://doi.org/10.1080/014311600210191, 2000.

Lukeš, P., Stenberg, P., Rautiainen, M., ottus, M. M., and Vanhatalo, M. K.: Optical properties of leaves and needles for boreal tree species in Europe, Remote Sensing Letters, 4, 667–676, https://doi.org/10.1080/2150704X.2013.782112, 2013.

Lupkes, C., Gryanik, V. M., Hartmann, J., and Andreas, E. L.: A parametrization, based on sea ice morphology, of the neutralatmospheric drag coefficients for weather predictionand climate models, J. Geophys. Res. Atmos., 117, https://doi.org/10.1029/2012JD017630, 2012.

Madden, R. A. and Julian, P. R.: Detection of a 40-50 day oscillation in the zonal wind in the tropical Pacific, J. Atmos. Sci., 28, 702–708, https://doi.org/10.1175/1520-0469(1971)028<0702:DOADOI>2.0.CO;2, 1971.

Malicet, J., Daumont, D., Charbonnier, J., Parisse, C., Chakir, A., and Brion, J.: Ozone UV spectroscopy. II. Absorption cross-sections and temperature dependence, J. Atmos. Chem., 21, 263–273, https://doi.org/10.1007/BF00696758, 1995.

https://doi.org/10.5194/egusphere-2026-2425
Preprint. Discussion started: 26 May 2026

Mann, G. W., Carslaw, K. S., Spracklen, D. V., Ridley, D. A., Manktelow, P. T., Chipperfield, M. P., Pickering, S. J., and Johnson, C. E.: Description and evaluation of GLOMAP-mode: a modal global aerosol microphysics model for the UKCA composition-climate model, Geosci. Model Dev., 3, 519–551, https://doi.org/10.5194/gmd-3-519-2010, 2010.

Manners, J., Thelen, J.-C., Petch, J., Hill, P., and Edwards, J. M.: Two fast radiative transfer methods to improve the temporal sampling of clouds in numerical weather prediction and climate models, Q. J. R. Meteorol. Soc., 135, 457–468, https://doi.org/10.1002/qj.956, 2009.

Manners, J., Vosper, S. B., and Roberts, N.: Radiative transfer over resolved topographic features for high-resolution weather prediction, Q. J. R. Meteorol. Soc., 138, 720–733, https://doi.org/10.1002/qj.956, 2012.

Manners, J., Edwards, J. M., Hill, P., and Thelen, J.-C.: SOCRATES (Suite Of Community RAdiative Transfer codes based on Edwards and Slingo) Technical Guide, Met Office, UK, https://code.metoffice.gov.uk/trac/socrates, last access: 15$^{\text{th}}$ July 2025, 2025.

Markel, V. A.: Introduction to the Maxwell Garnett approximation: tutorial, Journal of the Optical Society of America. A, Optics, image science, and vision, 33, 1244–1256, https://doi.org/10.1364/josaa.33.001244, 2016.

Marthews, T. R., Dadson, S. J., Lehner, B., Abele, S., and Gedney, N.: High-resolution global topographic index values, Dataset made available under the terms of the Open Government Licence, https://catalogue.ceh.ac.uk/documents/6b0c4358-2bf3-4924-aa8f-793d468b92be, last access: 25$^{\text{th}}$ October 2017, 2015.

McCabe, A. and Brown, A. R.: The role of surface heterogeneity in modelling the stable boundary layer, Bound.-Lay. Meteorol., 122, 517–534, https://doi.org/10.1007/s10546-006-9119-8, 2007.

Mercado, L. M., Huntingford, C., Gash, J. H. C., Cox, P. M., and Jogireddy, V.: Improving the representation of radiative interception and photosynthesis for climate model applications, Tellus, B59, 553–565, https://doi.org/10.1111/j.1600-0889.2007.00256.x, 2007.

Miller, D. A. and White, R. A.: A conterminous United States multilayer soil characteristics dataset for regional climate and hydrology modeling, Earth Interact., 2, 1–26, https://doi.org/10.1175/1087-3562(1998)002<0001:ACUSMS>2.3.CO;2, 1998.

Mlawer, E. J., Payne, V. H., Moncet, J.-L., Delamere, J. S., Alvarado, M. J., and Tobin, D. C.: Development and recent evaluation of the MT_CKD model of continuum absorption, Philos. Trans. R. Soc. Lond. A, 370, 2520–2556, https://doi.org/10.1098/rsta.2011.0295, 2012.

Mlawer, E. J., Turner, D. D., Paine, S. N., Palchetti, L., Bianchini, G., Payne, V. H., Cady-Pereira, K. E., Pernak, R. L., Alvarado, M. J., Gombos, D., Delamere, J. S., Mlynczak, M. G., and Mast, J. C.: Analysis of Water Vapor Absorption in the Far-Infrared and Submillimeter Regions Using Surface Radiometric Measurements From Extremely Dry Locations, Journal of Geophysical Research: Atmospheres, 124, 8134–8160, https://doi.org/https://doi.org/10.1029/2018JD029508, 2019.

Mondelain, D., Manigand, S., Kassi, S., and Campargue, A.: Temperature dependence of the water vapor self-continuum by cavity ring-down spectroscopy in the 1.6 μm transparency window, Journal of Geophysical Research: Atmospheres, 119, 5625–5639, https://doi.org/https://doi.org/10.1002/2013JD021319, 2014.

Morcrette, C. J.: Improvements to a prognostic cloud scheme through changes to its cloud erosion parametrization, Atmos. Sci. Let., 13, 95–102, https://doi.org/10.1002/asl.374, 2012.

Mulcahy, J. P., Jones, C., Sellar, A., Johnson, B., Boutle, I. A., Jones, A., Andrews, T., Rumbold, S. T., Mollard, J., Bellouin, N., Johnson, C. E., Williams, K. D., Grosvenor, D. P., and McCoy, D. T.: Improved Aerosol Processes and Effective Radiative Forcing in HadGEM3 and UKESM1, JAMES, 10, 2786–2805, https://doi.org/10.1029/2018MS001464, 2018.

Mulcahy, J. P., Johnson, C., Jones, C. G., Povey, A. C., Scott, C. E., Sellar, A., Turnock, S. T., Woodhouse, M. T., Abraham, N. L., Andrews, M. B., Bellouin, N., Browse, J., Carslaw, K. S., Dalvi, M., Folberth, G. A., Glover, M., Grosvenor, D. P., Hardacre, C., Hill, R., Johnson, B., Jones, A., Kipling, Z., Mann, G., Mollard, J., O'Connor, F. M., Palmiéri, J., Reddington, C., Rumbold, S. T., Richardson, M., Schutgens,

https://doi.org/10.5194/egusphere-2026-2425
Preprint. Discussion started: 26 May 2026

N. A. J., Stier, P., Stringer, M., Tang, Y., Walton, J., Woodward, S., and Yool, A.: Description and evaluation of aerosol in UKESM1 and HadGEM3-GC3.1 CMIP6 historical simulations, Geosci. Model Dev., 13, 6383–6423, https://doi.org/10.5194/gmd-13-6383-2020, 2020.

Mulcahy, J. P., Jones, C. G., Rumbold, S. T., Kuhlbrodt, T., Dittus, A. J., Blockley, E. W., Yool, A., Walton, J., Hardacre, C., Andrews, T., Bodas-Salcedo, A., Stringer, M., de Mora, L., Harris, P., Hill, R., Kelley, D., Robertson, E., and Tang, Y.: UKESM1.1: development and evaluation of an updated configuration of the UK Earth System Model, Geoscientific Model Development, 16, 1569–1600, https://doi.org/10.5194/gmd-16-1569-2023, 2023.

Nachtergaele, F., van Velthuizen, H., Verelst, L., Batjes, N., Dijkshoorn, K., van Engelen, V., Fischer, G., Jones, A., Montanarella, L., Petri, M., Prieler, S., Teixeira, E., Wiberg, D., and Shi, X.: Harmonized World Soil Database (version 1.0), FAO, FAO, Rome, Italy and IIASA, Laxenburg, Austria, 2008.

NASA/LARC/SD/ASDC: CERES Energy Balanced and Filled (EBAF) TOA and Surface Monthly means data in netCDF Edition 4.1, https://doi.org/10.5067/TERRA-AQUA/CERES/EBAF_L3B.004.1, 2019.

Nicholls, S.: The dynamics of stratocumulus: Aircraft observations and comparisons with a mixed layer model, Q. J. R. Meteorol. Soc., 110, 783–820, https://doi.org/10.1002/qj.49711046603, 1984.

Oki, T.: Validating the runoff from LSP-SVAT models using a global river routing network by one degree mesh, in: AMS 13^{th} Conference on Hydrology, Long Beach, California, 2-7^{th} February 1997, pp. 319–322, 1997.

Oki, T. and Sud, Y. C.: Design of Total Runoff Integrating Pathways (TRIP) — A global river channel network, Earth Interact., 2, 1–36, https://doi.org/10.1175/1087-3562(1998)002<0001:DOTRIP>2.3.CO;2, 1998.

Palmer, T. N., Buizza, R., Doblas-Reyes, F. J., Jung, T., Leutbecher, M., Shutts, G., Steinheimer, M., and Weisheimer, A.: Stochastic parametrization and model uncertainty, Tech. Rep. 598, ECMWF RD Technical Memorandum, ECMWF, Reading, UK, https://doi.org/10.21957/ps8gbwbdv, 2009.

Pincus, R., Barker, H. W., and Morcrette, J.-J.: A fast, flexible, approximate technique for computing radiative transfer in inhomogeneous cloud fields, Journal of Geophysical Research: Atmospheres, 108, https://doi.org/https://doi.org/10.1029/2002JD003322, 2003.

Pincus, R., Mlawer, E. J., Oreopoulos, L., Ackerman, A. S., Baek, S., Brath, M., Buehler, S. A., Cady-Pereira, K. E., Cole, J. N. S., Dufresne, J.-L., Kelley, M., Li, J., Manners, J., Paynter, D. J., Roehrig, R., Sekiguchi, M., and Schwarzkopf, D. M.: Radiative flux and forcing parameterization error in aerosol-free clear skies, Geophys. Res. Lett., 42, 5485–5492, https://doi.org/10.1002/2015GL064291, 2015.

Poulter, B., MacBean, N., Hartley, A., Khlystova, I., Arino, O., Betts, R., Bontemps, S., Boettcher, M., Brockmann, C., Defourny, P., Hagemann, S., Herold, M., Kirches, G., Lamarche, C., Lederer, D., Ottlé, C., Peters, M., and Peylin, P.: Plant functional type classification for Earth system models: results from the European Space Agency's Land Cover Climate Change Initiative, Geoscientific Model Development, 8, 2315–2328, https://doi.org/10.5194/gmd-8-2315-2015, 2014.

Prigent, C., Jimenez, C., and Catherinot, J.: Comparison of satellite microwave backscattering (ASCAT) and visible/near-infrared reflectances (PARASOL) for the estimation of aeolian aerodynamic roughness length in arid and semi-arid regions, Atmos. Meas. Tech.,, 5, 2703–2712, https://doi.org/10.5194/amt-5-2703-2012, 2012.

Ptashnik, I. V., McPheat, R. A., Shine, K. P., Smith, K. M., and Williams, R. G.: Water vapor self-continuum absorption in near-infrared windows derived from laboratory measurements, J. Geophys. Res.-Atmos., 116, D16 305, https://doi.org/10.1029/2011JD015603, 2011.

Ptashnik, I. V., McPheat, R. A., Shine, K. P., Smith, K. M., and Williams, R. G.: Water vapour foreign-continuum absorption in near-infrared windows from laboratory measurements, Philos. Trans. R. Soc. Lond. A, 370, 2557–2577, https://doi.org/10.1098/rsta.2011.0218, 2012.

https://doi.org/10.5194/egusphere-2026-2425
Preprint. Discussion started: 26 May 2026

Ptashnik, I. V., Klimeshina, T. E., Solodov, A. A., and Vigasin, A. A.: Spectral composition of the water vapour self-continuum absorption within 2.7 and 6.25 μm bands, Journal of Quantitative Spectroscopy and Radiative Transfer, 228, 97–105, https://doi.org/https://doi.org/10.1016/j.jqsrt.2019.02.024, 2019.

Ranjithkumar, A., Gordon, H., Williamson, C., Rollins, A., Pringle, K., Kupc, A., Abraham, N. L., Brock, C., and Carslaw, K.: Constraints on global aerosol number concentration, SO2 and condensation sink in UKESM1 using ATom measurements, Atmos. Chem. Phys., 21, 4979–5014, https://doi.org/10.5194/acp-21-4979-2021, 2021.

Rawlins, F., Ballard, S. P., Bovis, K. J., Clayton, A. M., Li, D., Inverarity, G. W., Lorenc, A. C., and Payne, T. J.: The Met Office global four-dimensional variational data assimilation system, Q. J. R. Meteorol. Soc., 133, 347–362, 2007.

Redelsperger, J.-L., Guichard, F., and Mondon, S.: A parametrization of mesoscale enhancement of surface fluxes for large-scale models, J. Climate, 13, 402–421, https://doi.org/10.1175/1520-0442(2000)013<0402:APOMEO>2.0.CO;2, 2000.

Renfrew, I. A., Elvidge, A. D., and Edwards, J. M.: Atmospheric sensitivity to marginal-ice-zone drag: global and local responses, Q. J. R. Meteorol. Soc., 145, 1165–1179, https://doi.org/10.1002/qj.3486, 2019.

Richard, L., Vasilchenko, S., Mondelain, D., Ventrillard, I., Romanini, D., and Campargue, A.: Water vapor self-continuum absorption measurements in the 4.0 and 2.1μm transparency windows, Journal of Quantitative Spectroscopy and Radiative Transfer, 201, 171–179, https://doi.org/https://doi.org/10.1016/j.jqsrt.2017.06.037, 2017.

Rooney, G. G. and Jones, I. D.: Coupling the 1-D lake model FLake to the community land-surface model JULES, Boreal Env. Res., 15, 501–512, 2010.

Rothman, L. S., Gordon, I. E., Babikov, Y., Barbe, A., Chris Benner, D., Bernath, P. F., Birk, M., Bizzocchi, L., Boudon, V., Brown, L. R., Campargue, A., Chance, K., Cohen, E. A., Coudert, L. H., Devi, V. M., Drouin, B. J., Fayt, A., Flaud, J.-M., Gamache, R. R., Harrison, J. J., Hartmann, J.-M., Hill, C., Hodges, J. T., Jacquemart, D., Jolly, A., Lamouroux, J., Le Roy, R. J., Li, G., Long, D. A., Lyulin, O. M., Mackie, C. J., Massie, S. T., Mikhailenko, S., Müller, H. S. P., Naumenko, O. V., Nikitin, A. V., Orphal, J., Perevalov, V., Perrin, A., Polovtseva, E. R., Richard, C., Smith, M. A. H., Starikova, E., Sung, K., Tashkun, S., Tennyson, J., Toon, G. C., Tyuterev, V. G., and Wagner, G.: The HITRAN2012 molecular spectroscopic database, J. Quant. Spectrosc. Radiat. Transfer, 130, 4–50, https://doi.org/10.1016/j.jqsrt.2013.07.002, 2013.

Samanta, A., Ganguly, S., Schull, M. A., Shabanov, N. V., Knyazikhin, Y., and Myneni, R. B.: Collection 5 MODIS LAI/FPAR Products, Presented at AGU Fall Meeting, San Francisco, USA, 15^{th}–19^{th} December, 2008, 2012.

Sanchez, C., Williams, K. D., and Collins, M.: Improved stochastic physics schemes for global weather and climate models, Q. J. R. Meteorol. Soc., 142, 147–159, https://doi.org/10.1002/qj.2640, 2016.

Sellar, A. A., Jones, C. G., Mulcahy, J. P., Tang, Y., Wiltshire, A., O'Connor, F. M., Stringer, M., Hill, R., Palmieri, J., Woodward, S., de Mora, L., Kuhlbrodt, T., Rumbold, S. T., Kelley, D. I., Ellis, R., Johnson, C. E., Walton, J., Abraham, N. L., Andrews, M. B., Andrews, T., Archibald, A. T., Berthou, S., Burke, E., Blockley, E., Carslaw, K., Dalvi, M., Edwards, J., Folberth, G. A., Gedney, N., Griffiths, P. T., Harper, A. B., Hendry, M. A., Hewitt, A. J., Johnson, B., Jones, A., Jones, C. D., Keeble, J., Liddicoat, S., Morgenstern, O., Parker, R. J., Predoi, V., Robertson, E., Siahaan, A., Smith, R. S., Swaminathan, R., Woodhouse, M. T., Zeng, G., and Zerroukat, M.: UKESM1: Description and Evaluation of the U.K. Earth System Model, Journal of Advances in Modeling Earth Systems, 11, 4513–4558, https://doi.org/10.1029/2019MS001739, 2019.

Sellar, A. A., Walton, J., Jones, C. G., Wood, R., Abraham, N. L., Andrejczuk, M., Andrews, M. B., Andrews, T., Archibald, A. T., Mora, L., Dyson, H., Elkington, M., Ellis, R., Florek, P., Good, P., Gohar, L., Haddad, S., Hardiman, S. C., Hogan, E., Iwi, A., Jones, C. D., Johnson, B., Kelley, D. I., Kettleborough, J., Knight, J. R., Köhler, M. O., Kuhlbrodt, T., Liddicoat, S., Linova-Pavlova, I., Mizielinski, M. S.,

https://doi.org/10.5194/egusphere-2026-2425
Preprint. Discussion started: 26 May 2026

Morgenstern, O., Mulcahy, J., Neininger, E., O'Connor, F. M., Petrie, R., Ridley, J., Rioual, J., Roberts, M., Robertson, E., Rumbold, S., Seddon, J., Shepherd, H., Shim, S., Stephens, A., Teixiera, J. C., Tang, Y., Williams, J., Wiltshire, A., and Griffiths, P. T.: Implementation of U.K. Earth System Models for CMIP6, Journal of Advances in Modeling Earth Systems, 12, https://doi.org/10.1029/2019MS001946, 2020.

Sellers, P. J.: Canopy reflectance, photosynthesis and transpiration, International Journal of Remote Sensing, 6, 1335–1372, https://doi.org/10.1080/01431168508948283, 1985.

Serdyuchenko, A., Gorshelev, V., Weber, M., Chehade, W., and Burrows, J. P.: High spectral resolution ozone absorption cross-sections - part 2: temperature dependence, Atmos. Meas. Tech., 7, 625–636, https://doi.org/10.5194/amt-7-625-2014, 2014.

Smith, R. N. B.: A scheme for predicting layer clouds and their water contents in a GCM, Q. J. R. Meteorol. Soc., 116, 435–460, https://doi.org/10.1002/qj.49711649210, 1990.

Smith, S.: Accounting for moist processes in a sub-grid orographic drag scheme., Q. J. R. Meteorol. Soc., 147, 2124–2146, https://doi.org/10.1002/qj.4013, 2021.

Smith, S., Field, P., Vosper, S., Shipway, B., and Hill, A.: A parametrization of subgrid orographic rain enhancement via the seeder-feeder effect, Q. J. R. Meteorol. Soc., 142, 132–142, https://doi.org/10.1002/qj.2637, 2016.

Smith, S. A., Field, P. R., Vosper, S. B., and Derbyshire, S. H.: Verification of a seeder-feeder orographic precipitation enhancement scheme accounting for low-level blocking, Q. J. R. Meteorol. Soc., 145, 2909–2932, https://doi.org/10.1002/qj.3584, 2019.

Smolander, S. and Stenberg, P.: Simple parameterizations of the radiation budget of uniform broadleaved and coniferous canopies, Remote Sens. Environ., 94, 355–3463, https://doi.org/10.1016/j.rse.2004.10.010, 2005.

Taylor, J. W., Wu, H., Szpek, K., Bower, K., Crawford, I., Flynn, M. J., Williams, P. I., Dorsey, J., Langridge, J. M., Cotterell, M. I., Fox, C., Davies, N. W., Haywood, J. M., and Coe, H.: Absorption closure in highly aged biomass burning smoke, Atmos. Chem. Phys., 20, 11 201–11 221, https://doi.org/10.5194/acp-20-11201-2020, 2020.

Tennant, W. J., Shutts, G. J., Arribas, A., and Thompson, S. A.: Using a stochastic kinetic energy backscatter scheme to improve MOGREPS probabilistic forecast skill, Mon. Weather Rev., 139, 1190–1206, https://doi.org/10.1175/2010MWR3430.1, 2011.

Thomason, L. W., Ernest, N., Millán, L., Rieger, L., Bourassa, A., Vernier, J.-P., Manney, G., Luo, B., Arfeuille, F., and Peter, T.: A global space-based stratospheric aerosol climatology: 1979–2016, Earth System Science Data, 10, 469–492, https://doi.org/10.5194/essd-10-469-2018, 2018.

Untch, A. and Simmons, A. J.: Increased stratospheric resolution in the ECMWF forecasting system, Tech. Rep. 82, ECMWF Newsletter, ECMWF, Reading, UK, 1999.

Uppala, S. M., Kallberg, P. W., Simmons, A. J., Andrae, U., da Costa Bechtold, V., Fiorino, M., Gibson, J. K., Haseler, J., Hernandez, A., Kelly, G. A., Li, X., Onogi, K., Saarinen, S., Sokka, N., Allan, R. P., Andersson, E., Arpe, K., Balmaseda, M. A., Beljaars, A. C. M., van de Berg, L., Bidlot, J., Bormann, N., Caires, S., Chevallier, F., Dethof, A., Dragosavac, M., Fisher, M., Fuentes, M., Hagemann, S., Holm, E., Hoskins, B. J., Isaksen, L., Janssen, P. A. E. M., Jenne, R., McNally, A. P., Mahfouf, J.-F., Morcrette, J.-J., Rayner, N. A., Saunders, R. W., Simon, P., Sterl, A., Trenberth, K., Untch, A., Vasiljevic, D., Viterbo, P., and Woollen, J.: The ERA-40 re-analysis, Q. J. R. Meteorol. Soc., 131, 2961–3012, https://doi.org/10.1256/qj.04.176, 2005.

van Genuchten, M. T.: A closed-form equation for predicting the hydraulic conductivity of unsaturated soils, Soil Sci. Soc. America J., 44, 892–898, https://doi.org/10.2136/sssaj1980.03615995004400050002x, 1980.

van Marle, M. J. E., Kloster, S., Magi, B. I., Marlon, J. R., Daniau, A.-L., Field, R. D., Arneth, A., Forrest, M., Hantson, S., Kehrwald, N. M., Knorr, W., Lasslop, G., Li, F., Mangeon, S., Yue, C., Kaiser, J. W., and van der Werf, G. R.: Historic global biomass burning emissions for

https://doi.org/10.5194/egusphere-2026-2425
Preprint. Discussion started: 26 May 2026

CMIP6 (BB4CMIP) based on merging satellite observations with proxies and fire models (1750–2015), Geoscientific Model Development, 10, 3329–3357, https://doi.org/10.5194/gmd-10-3329-2017, 2017.

Van Weverberg, K., Boutle, I. A., Morcrette, C. J., and Newsom, R. K.: Towards retrieving critical relative humidity from ground-based remote-sensing observations, Q. J. R. Meteorol. Soc., 142, 2867–2881, https://doi.org/10.1002/qj.2874, 2016.

Van Weverberg, K., Morcrette, C. J., and Boutle, I. A.: A Bimodal Diagnostic Cloud Fraction Parameterization. Part II: Evaluation and Resolution Sensitivity, Mon. Weather Rev., 149, 859–878, https://doi.org/10.1175/MWR-D-20-0230.1, 2021a.

Van Weverberg, K., Morcrette, C. J., Boutle, I. A., Furtado, K., and Field, P. R.: A Bimodal Diagnostic Cloud Fraction Parameterization. Part I: Motivating Analysis and Scheme Description, Mon. Weather Rev., 149, 841–847, https://doi.org/10.1175/MWR-D-20-0224.1, 2021b.

Ventrillard, I., Romanini, D., Mondelain, D., and Campargue, A.: Accurate measurements and temperature dependence of the water vapor self-continuum absorption in the 2.1 μm atmospheric window, The Journal of Chemical Physics, 143, 134 304, https://doi.org/10.1063/1.4931811, 2015.

Verhoef, A. and Egea, G.: Modeling plant transpiration under limited soil water: Comparison of different plant and soil hydraulic parameterizations and preliminary implications for their use in land surface models, Agric. For. Meteorol., 191, 22–32, https://doi.org/10.1016/j.agrformet.2014.02.009, 2014.

Vosper, S. B.: Mountain waves and wakes generated by South Georgia: implications for drag parametrization, Q. J. R. Meteorol. Soc., 141, 2813–2827, https://doi.org/10.1002/qj.2566, 2015.

Walters, D., Baran, A., Boutle, I., Brooks, M., Earnshaw, P., Edwards, J., Furtado, K., Hill, P., Lock, A., Manners, J., Morcrette, C. Mulcahy, J., Sanchez, C., Smith, C., Stratton, R., Tennant, W., Tomassini, L., Van Weverberg, K., Vosper, S., Willett, M., Browse, J., Bushell, A., Dalvi, M., Essery, R., Gedney, N., Hardiman, S., Johnson, B., Johnson, C., Jones, A., Mann, G., Milton, S., Rumbold, H., Sellar, A., Ujiie, M., Whitall, M., Williams, K., and Zerroukat, M.: The Met Office Unified Model Global Atmosphere 7.0/7.1 and JULES Global Land 7.0 configurations, Geosci. Model Dev., 12, 1909–1963, https://doi.org/doi.org/10.5194/gmd-12-1909-2019, 2019.

Walters, D. N., Best, M. J., Bushell, A. C., Copsey, D., Edwards, J. M., Falloon, P. D., Harris, C. M., Lock, A. P., Manners, J. C., Morcrette, C. J., Roberts, M. J., Stratton, R. A., Webster, S., Wilkinson, J. M., Willett, M. R., Boutle, I. A., Earnshaw, P. D., Hill, P. G., MacLachland, C., Martin, G. M., Moufouma-Okia, W., Palmer, M. D., Petch, J. C., Rooney, G. G., Scaife, A. A., and Williams, K. D.: The Met Office Unified Model Global Atmosphere 3.0/3.1 and JULES Global Land 3.0/3.1 configurations, Geosci. Model Dev., 4, 919–941, https://doi.org/10.5194/gmd-4-919-2011, 2011.

Walters, D. N., Williams, K. D., Boutle, I. A., Bushell, A. C., Edwards, J. M., Field, P. R., Lock, A. P., Morcrette, C. J., Stratton, R. A., Wilkinson, J. M., Willett, M. R., Bellouin, N., Bodas-Salcedo, A., Brooks, M. E., Copsey, D., Earnshaw, P. D., Harris, C. M., Levine, R. C., MacLachlan, C., Manners, J. C., Martin, G. M., Milton, S. F., Palmer, M. D., Roberts, M. J., Rodríguez, J. M., Tennant, W. J., and Vidale, P.: The Met Office Unified Model Global Atmosphere 4.0 and JULES Global Land 4.0 configurations, Geosci. Model Dev., 7, 361–386, https://doi.org/10.5194/gmd-7-361-2014, 2014.

Walters, D. N., Brooks, M., Boutle, I., Melvin, T., Stratton, R., Vosper, S., Wells, H., Williams, K., Wood, N., Allen, T., Bushell, A., Copsey, D., Earnshaw, P., Edwards, J., Gross, M., Hardiman, S., Harris, C., Heming, J., Klingman, N., Levine, R., Manners, J., Martin, G., Milton, S., Mittermaier, M., Morcrette, C., Riddick, T., Roberts, M., Sanchez, C., Selwood, P., Stirling, A., Smith, C., Suri, D., Tennant, W., Vidale, P. L., Wilkinson, J., Willett, M., Woolnough, S., and Xavier, P.: The Met Office Unified Model Global Atmosphere 6.0/6.1 and JULES Global Land 6.0/6.1 configurations, Geosci. Model Dev., 10, 1487–1520, https://doi.org/10.5194/gmd-10-1487-2017, 2017.

Warner, C. D. and McIntyre, M. E.: An ultrasimple spectral parametrization for nonorographic gravity waves, J. Atmos. Sci., 58, 1837–1857, https://doi.org/10.1175/1520-0469(2001)058<1837:AUSPFN>2.0.CO;2, 2001.

https://doi.org/10.5194/egusphere-2026-2425
Preprint. Discussion started: 26 May 2026

Weisheimer, A., Palmer, T. N., and Doblas-Reyes, F. J.: Assessment of representations of model uncertainty in monthly and seasonal forecast ensembles, Geophys. Res. Lett., 38, L16 703, https://doi.org/10.1029/2011GL048123, 2011.

Weisheimer, A., Cortia, S., Palmer, T., and Vitart, F.: Addressing model error through atmospheric stochastic physical parametrizations: impact on the coupled ECMWF seasonal forecasting system, Philos. Trans. R. Soc. Lond. A, 372, 20130 290, https://doi.org/10.1098/rsta.2013.0290, 2014.

Wentz, F. J. and Spencer, R. W.: SSM/I rain retrievals within a unified all-weather ocean algorithm, J. Atmos. Sci., 55, 1613–1627, https://doi.org/10.1175/1520-0469(1998)055<1613:SIRRWA>2.0.CO;2, note: SSM/I data are produced by Remote Sensing Systems and sponsored by the NASA Earth Science MEaSUREs DISCOVER Project. Data are available at `http://www.remss.com`, last access: 25th October 2017, 1998.

Wesely, M.: Parameterization of surface resistances to gaseous dry deposition in regional-scale numerical models, Atmos. Environ., 23, 1293–1304, 1989.

West, A. E., McLaren, A. E., Hewitt, H. T., and Best, M. J.: The location of the thermodynamic atmosphere-ice interface in fully coupled models - a case study using JULES and CICE, Geosci. Model Dev., 9, 1125–1141, https://doi.org/doi.org/10.5194/gmd-9-1125-2016, 2016.

West, R. E. L., Stier, P., Jones, A., Johnson, C. E., Mann, G. W., Bellouin, N., Partridge, D. G., and Kipling, Z.: The importance of vertical velocity variability for estimates of the in direct aerosol effects, Atmos. Chem. Phys., 14, 6369–6393, https://doi.org/10.5194/acp-14-6369-2014, 2014.

Willett, M., Brooks, M., Bushell, A., Earnshaw, P., Smith, S., Tomassini, L., Best, M., Boutle, I., Brooke, J., Edwards, . J. M., Elvidge, A. D., Furtado, K., Hardacre, C., Hartley, A. J., Hewitt, A. J., Johnson, B., Lock, A., Malcolm, A., Mulcahy, J., Müller, E., Renfrew, I. A., Rumbold, H., Rooney, G. G., Sellar, A., Ujiie, M., van Niekerk, A., Wiltshire, A., and Whitall, M.: The Met Office Unified Model Global Atmosphere 8.0 and JULES Global Land 9.0 configurations, Geosci. Model Dev., 19, 1473–1517, https://doi.org/10.5194/gmd-19-1473-2026, 2026.

Willett, M. R.: Supplementary material in support of manuscript "The Met Office Unified Model Global Atmosphere and Land 9.0 configuration": AMIP, NWP DA trial and NWP case study data., https://doi.org/10.5281/zenodo.19484323, 2026a.

Willett, M. R.: Supplementary material in support of manuscript "The Met Office Unified Model Global Atmosphere and Land 9.0 configuration": Python scripts, https://doi.org/10.5281/zenodo.19666610, 2026b.

Willett, M. R. and Whitall, M. A.: A Simple Prognostic based Convective Entrainment Rate for the Unified Model: Description and Tests, Forecasting Research Technical Report 617, Met Office, FitzRoy Road, Exeter, Devon EX1 3PB, UK, 2017.

Wilson, D. R. and Ballard, S. P.: A microphysically based precipitation scheme for the U.K. Meteorological Office Unified Model, Q. J. R. Meteorol. Soc., 125, 1607–1636, https://doi.org/10.1002/qj.49712555707, 1999.

Wilson, D. R., Bushell, A. C., Kerr-Munslow, A. M., Price, J. D., and Morcrette, C. J.: PC2: A prognostic cloud fraction and condensation scheme. I: Scheme description, Q. J. R. Meteorol. Soc., 134, 2093–2107, https://doi.org/10.1002/qj.333, 2008a.

Wilson, D. R., Bushell, A. C., Kerr-Munslow, A. M., Price, J. D., Morcrette, C. J., and Bodas-Salcedo, A.: PC2: A prognostic cloud fraction and condensation scheme. II: Climate model simulations, Q. J. R. Meteorol. Soc., 134, 2109–2125, https://doi.org/10.1002/qj.332, 2008b.

Wiltshire, A. J., Duran Rojas, M. C., Edwards, J. M., Gedney, N., Harper, A. B., Hartley, A. J., Hendry, M. A., Robertson, E., and Smout-Day, K.: JULES-GL7: the Global Land configuration of the Joint UK Land Environment Simulator version 7.0 and 7.2, Geosci. Model Dev., 13, 483–505, https://doi.org/10.5194/gmd-13-483-2020, 2020.

https://doi.org/10.5194/egusphere-2026-2425
Preprint. Discussion started: 26 May 2026

Wood, N., Brown, A. R., and Hewer, F. E.: Parametrizing the effects of orography on the boundary layer: An alternative to effective roughness lengths, Q. J. R. Meteorol. Soc., 127, 759–777, https://doi.org/10.1002/qj.49712757303, 2001.

Wood, N., Diamantakis, M., and Staniforth, A.: A monotonically-damping second-order-accurate unconditionally-stable numerical scheme for diffusion, Q. J. R. Meteorol. Soc., 133, 1559–1573, https://doi.org/10.1002/qj.116, 2007.

Wood, N., Staniforth, A., White, A., Allen, T., Diamantakis, M., Gross, M., Melvin, T., Smith, C., Vosper, S., Zerroukat, M., and Thuburn, J.: An inherently mass-conserving semi-implicit semi-Lagrangian discretization of the deep-atmosphere global non-hydrostatic equations, Q. J. R. Meteorol. Soc., 140, 1505–1520, https://doi.org/10.1002/qj.2235, 2014.

Woodward, S.: Mineral dust in HadGEM2, Tech. Rep. 87, Hadley Centre, Met Office, Exeter, UK, 2011.

Xavier, P., Willett, M., Graham, T., Earnshaw, P., Copsey, D., Narayan, N., Marzin, C., Sellar, A., Ackerley, D., Blockley, E., Bodas-Salcedo, A., Bushell, A., Choi, N., Chua, X. R., Guiavarc'h, C., Hassim, M., Heming, J., Hudson, D., Ineson, S., Jones, C., Keane, R., Kim, K., Kim, J., Kuhlbrodt, T., Lee, M., Li, C., Martin, G., Mccabe, A., Moise, A., Ridley, J., Roberts, L., Sahany, S., Schiemann, R. K. H., Storkey, D., Tennant, W., Tomassini, L., Tsushima, Y., Weedon, G. P., West, A., Wheeler, M., Zhou, X., and Zhu, H.: Assessment of the Met Office Global Coupled model version 5 (GC5) configurations, [in preparation], 2026.

Xie, P. and Arkin, P. A.: Global precipitation: A 17-year monthly analysis based on gauge observations, satellite estimates, and numerical model outputs, Bull. Amer. Meteorol. Soc., 78, 2539–2558, https://doi.org/10.1175/1520-0477(1997)078<2539:GPAYMA>2.0.CO;2, 1997.

Zerroukat, M. and Allen, T.: On the monotonic and conservative transport on overset/Yin–Yang grids, J. Comput. Phys., 302, 285–299, https://doi.org/10.1016/j.jcp.2015.09.006, 2015.

Zhang, Y., Li, M., Cheng, Y., Geng, G., Hong, C., Li, H., Li, X., Tong, D., Wu, N., Zhang, X., Zheng, B., Zheng, Y., Bo, Y., Su, H., and Zhang, Q.: Modeling the aging process of black carbon during atmospheric transport using a new approach: a case study in Beijing, Atmos. Chem. Phys., 19, 9663–9680, https://doi.org/10.5194/acp-19-9663-2019, 2019.

Zhong, W. and Haigh, J. D.: An efficient and accurate correlated-k parameterization of infrared radiative transfer for troposphere–stratosphere–mesosphere GCMs, Atmos. Sci. Lett., 1, 125–135, https://doi.org/10.1006/asle.2000.0022, 2000.